

POLITECNICO DI TORINO  
MSc IN BIOMEDICAL ENGINEERING

**DESIGN OF WEARABLE STRAIN SENSORS BASED ON STRETCHABLE  
ELECTRONICS FOR HUMAN MOTION MONITORING APPLICATIONS**



---

*Supervisors*

*Prof. Laura Gastaldi*

*Prof. Fabrizio Billi*

*Prof. Stefano Paolo Pastorelli*

*Author*

Mattia Cosimo Devangelio

Academic Year 2019 - 2020

*Design of wearable strain sensors based on stretchable electronics for human motion monitoring applications, Academic Year 2019 - 2020*

University of California, Los Angeles  
David Geffen School of Medicine, Department of Orthopaedic Surgery  
NanoLab (California NanoSystems Institute)  
Billi Research Lab

## ABSTRACT

---

Wearable devices have been attracting growing interest in detection of human body motion and human physiological parameters. In the healthcare field, motion data is used for diagnosis and rehabilitation as well as in sport science it is significant for physical therapy and training of athletes. Although the development of high-performance electronic devices for wearable applications represents a demanding challenge, investigated sensing devices with high stretchability have shown good suitability to be employed for several potential applications in human motion monitoring. For this aim, flexible and stretchable sensors, based on strain-response mechanism, were designed and analyzed by the conducted research study. The design process began with the steps of material selection and structure design through to the final fabrication and characterization process: simple fabrication steps were introduced to prepare sensing samples, which were assembled from conductive composite and finally characterized in terms of electromechanical response. Moreover, hardware and software methods, based on high resolution analog-digital conversion, were adopted in order to interface with the samples, making possible to perform real-time data acquisition. Applications to monitor human body motion were investigated by carrying out dynamic tests, proving the sensors were appropriate also for multiple motion detection. The acquired sensing signals were then analyzed and the related final results discussed. The developed samples showed high stretchability, high electrical conductivity, and excellent fit for wearable applications, leading to the possibility of further integration into more complex wearable sensing systems.



# CONTENTS

---

I	THEORETICAL FRAMEWORK AND LITERATURE REVIEW	1
1	CHAPTER ONE	3
1.1	Flexible and Stretchable Wearable Systems . . . . .	3
1.2	Activity Monitoring . . . . .	4
2	CHAPTER TWO	5
2.1	Stretchable Strain Sensors . . . . .	5
2.1.1	Performance Parameters . . . . .	5
2.2	Sensing Mechanism . . . . .	7
2.2.1	Piezoresistivity . . . . .	7
2.2.2	Capacitance . . . . .	9
2.3	Stretchable Sensors Design . . . . .	11
2.3.1	Material Design . . . . .	11
2.3.2	Structure Design . . . . .	15
II	CONCEPTUAL AND PRACTICAL DEVELOPMENT	19
3	CHAPTER THREE	21
3.1	Conductive Polymer Matrix Composites . . . . .	21
3.2	Conductive Percolation Network . . . . .	21
3.3	Composite Fabrication Method . . . . .	24
3.3.1	Fabrication Process . . . . .	26
3.4	Composite Electrical Characterization . . . . .	28
3.4.1	Two-point Technique . . . . .	30
3.5	Percolation Analysis . . . . .	38
3.6	SEM Analysis . . . . .	42
4	CHAPTER FOUR	59
4.1	Deformation Dependence . . . . .	59
4.2	Single Stripe-shaped Sensor Design . . . . .	60
4.2.1	Mold Design and Fabrication . . . . .	61
4.2.2	Silicon-based Polymer Preparation . . . . .	65
4.3	Stripe Sample Fabrication . . . . .	67
4.3.1	Led Test . . . . .	71
5	CHAPTER FIVE	73
5.1	Board Set-up . . . . .	73
5.2	Resistance Change Reading . . . . .	74
5.2.1	Analog-to-Digital Conversion . . . . .	75
5.3	Hardware Set-up . . . . .	77
5.3.1	Voltage Divider Method . . . . .	78
5.3.2	Software Set-up . . . . .	80
5.4	Multiacquisition . . . . .	80
5.5	High Resolution Analog-to-Digital Converter . . . . .	84
5.5.1	Hardware Description . . . . .	84
5.5.2	Pins Configuration . . . . .	86

5.6	Serial Interface . . . . .	87
5.6.1	Read/Write Operation . . . . .	89
5.7	Registers Description . . . . .	92
5.7.1	Data Registers . . . . .	94
III	HUMAN MOTION MONITORING APPLICATIONS	95
6	CHAPTER SIX	97
6.1	Signal Acquisition and Filter Stage . . . . .	97
6.2	Electromechanical Performance . . . . .	100
6.3	Human Motion Monitoring . . . . .	105
6.4	Developments in Stretchable Electronics . . . . .	118
IV	APPENDIX	119
A	SOFTWARE ROUTINES	121
A.1	Processing Script . . . . .	121
	BIBLIOGRAPHY	125

## LIST OF FIGURES

---

Figure 1	Application areas of wearable physical sensors.	3
Figure 2	Example of stretchable sensor . . . . .	4
Figure 3	Illustration of the difference between dispersion and distribution. . . . .	24
Figure 4	Composite created from Ag powder and PDMS polymer. . . . .	28
Figure 5	Electron flow inside a conductive material. . .	28
Figure 6	Two-point resistivity measurement. . . . .	30
Figure 7	Schematic of the division into intervals of the sample length. . . . .	31
Figure 8	Micromanipulator Manual Probe Station. . . .	32
Figure 9	The tips of the two probes . . . . .	33
Figure 10	Global scatter plot . . . . .	34
Figure 11	Linear fitting of resistance readings related to 75 wt% samples. . . . .	35
Figure 12	Linear fitting of resistance readings related to 80 wt% samples. . . . .	36
Figure 13	Ag weight-volume concentration relationship curve. . . . .	38
Figure 14	Concentration-conductivity curve. . . . .	39
Figure 15	Schematic of estimated percolation threshold.	39
Figure 16	Example of percolation curve. . . . .	40
Figure 17	Linear fitting of the curve in logarithmic scale.	41
Figure 18	Ion Beam Sputtering System. . . . .	42
Figure 19	ZEISS Scanning Electron Microscope. . . . .	43
Figure 20	Cross-sectional view of sample with Ag concentration of 75 wt%. . . . .	44
Figure 21	Cross-sectional view of sample with Ag concentration of 80 wt%. . . . .	45
Figure 22	Cross-sectional images for particle analysis. . .	46
Figure 23	Parameter distributions for the 75 wt% image.	47
Figure 24	Parameter distributions for the 80 wt% image.	48
Figure 25	Original and logical images. . . . .	50
Figure 26	Clusters identification of the 75 wt% processed image. . . . .	50
Figure 27	Original and logical images. . . . .	51
Figure 28	Clusters identification of the 80 wt% processed image. . . . .	51
Figure 29	Distribution of cluster area for $th = 1000$ . . . .	53
Figure 30	Scatter plot of clusters with area values $> 1000$ .	53
Figure 31	Cross-sectional SEM image of the sample. . . .	54

Figure 32	Back-scattered cross-sectional image . . . . .	55
Figure 33	Cross-sectional image highlights the different appearance of the two materials. . . . .	55
Figure 34	Detail of the Ag particles with low (a) and high (b) magnification. . . . .	56
Figure 35	SEM images of samples under states of increasing deformation. . . . .	57
Figure 36	Render 3D model of the stripe sensor's parts. .	61
Figure 37	3DXTech ABS 3D printing filament. . . . .	61
Figure 38	Geometric design of the 3D printed mold. . . .	62
Figure 39	3D editor view of the scaled up model. . . . .	63
Figure 40	Slicing previews. . . . .	64
Figure 41	Set-up for starting the vacuum process. . . . .	65
Figure 42	Valve reopening procedure. . . . .	66
Figure 43	Produced PDMS, before and after vacuum degassing. . . . .	66
Figure 44	Pouring process into the custom-made mold. .	67
Figure 45	Heating system. . . . .	67
Figure 46	Obtained lower support layer. . . . .	68
Figure 47	Conductive layer deposition procedure. . . . .	68
Figure 48	Conductive layer properly applied on the lower support layer. . . . .	69
Figure 49	Wires connection and complete structure. . . .	69
Figure 50	Pouring process to obtain the final sandwich structure. . . . .	70
Figure 51	Strain sensor in different states. . . . .	70
Figure 52	Series electrical circuit of LED and sensor. . . .	71
Figure 53	Emitting LED due to electrical continuity. . . .	71
Figure 54	Stretching applied to the sample. . . . .	72
Figure 55	HUZZAH32 – ESP32 Feather Board. . . . .	73
Figure 56	Arduino IDE Preferences. . . . .	74
Figure 57	Block diagram of a 12-bit SAR ADC. . . . .	75
Figure 58	Analog Pins. . . . .	77
Figure 59	Electrical circuit schematic. . . . .	78
Figure 60	Voltage divider configuration. . . . .	79
Figure 61	Breakout CD74HC4067. . . . .	81
Figure 62	Connection based on the multiplexing strategy.	83
Figure 63	16-TSSOP Breakout AD7746. . . . .	84
Figure 64	AD7746 Block diagram. . . . .	85
Figure 65	Block diagram of a 2nd-order $\Delta\Sigma$ modulator. .	86
Figure 66	AD7746 Pin configuration (16-Lead TSSOP). .	86
Figure 67	Generic example of I <sup>2</sup> C bus. . . . .	88
Figure 68	Start byte address for Read/Write operation. .	90
Figure 69	Write and Read Sequences. . . . .	91
Figure 70	Conversion data reading process. . . . .	92
Figure 71	Data transmission from microcontroller to PC.	97

Figure 72	Data storage through self-written Processing program. . . . .	97
Figure 73	Connection set-up for real-time signal acquisition. . . . .	98
Figure 74	Example of original signal filtered by Savitzky-Golay filter. . . . .	99
Figure 75	Strain of 20% applied on the fixed sample. . .	100
Figure 76	Examples of increasing strain tests. . . . .	101
Figure 77	Example of response time evaluation. . . . .	102
Figure 78	Fixed sample in pressing and pinching states.	103
Figure 79	Slow pressing test. . . . .	104
Figure 80	Fast pressing test. . . . .	104
Figure 81	Pinching test. . . . .	105
Figure 82	Cycles of motion of the ankle joint at different frequency values. . . . .	106
Figure 83	Strain sensor placed on the ankle joint. . . . .	107
Figure 84	Cycles of motion of the ankle joint by moving the foot upwards. . . . .	107
Figure 85	Strain sensor placed on the wrist joint. . . . .	108
Figure 86	Quick bending cycles of the wrist joint at different frequencies. . . . .	109
Figure 87	Bending cycles of the wrist joint with controlled unloading phase. . . . .	110
Figure 88	Strain sensor placed on the proximal interphalangeal joint. . . . .	110
Figure 89	Full bending-unbending cycles of the interphalangeal joint. . . . .	111
Figure 90	Quick bending-unbending cycles of the interphalangeal joint. . . . .	112
Figure 91	Finger bending. . . . .	112
Figure 92	Vibration test of the interphalangeal joint. . . .	113
Figure 93	Strain sensor placed on the knee joint. . . . .	113
Figure 94	Full up-down cycles of the knee joint. . . . .	114
Figure 95	Full up-down cycles of the knee joint with controlled release phase. . . . .	115
Figure 96	Representative strain-resistance change curve.	117
Figure 97	Examples of innovative soft electronics. . . . .	118

## LIST OF TABLES

---

Table 1	Experimental resistance values. . . . .	33
Table 2	Calculated experimental parameter. . . . .	37
Table 3	Statistical data of conductivity values. . . . .	37
Table 4	Particle results of the analyzed images by the Software. . . . .	46
Table 5	Detected clusters by setting an area threshold of 1000. . . . .	54
Table 6	Slicer software settings. . . . .	63
Table 7	I/O limit values. . . . .	76
Table 8	MUX pins. . . . .	81
Table 9	Pin function description. . . . .	87
Table 10	Registers summary. . . . .	93
Table 11	Filter arguments. . . . .	99

## ACRONYMS

---

ABS	Acrylonitrile Butadiene Styrene
ADC	Analog-to-digital Converter
AgNPs	Silver Nanoparticles
AgNWs	Silver Nanowires
AWG	American Wire Gauge
CNFs	Carbon Nanofibers
CNTs	Carbon Nanotubes
FDM	Fused Deposition Modeling
GF	Gauge Factor
IDE	Integrated Development Environment
LSB	Least Significant Bit
MSB	Most Significant Bit
MWCNTs	Multi-walled Carbon Nanotubes
PDMS	Poly(dimethylsiloxane)
PEDOT	Poly(3,4 ethylenedioxythiophene)
PSS	Poly(styrenesulfonate)
PU	Polyurethane
SACNTs	Super-aligned Carbon Nanotubes
SAR	Successive Approximation Register
SBR	Styrene-butadiene Rubber
TPU	Thermoplastic Polyurethane
UART	Universal Asynchronous Receiver-transmitter



Part I

---

THEORETICAL FRAMEWORK AND  
LITERATURE REVIEW



## CHAPTER ONE

---

### 1.1 FLEXIBLE AND STRETCHABLE WEARABLE SYSTEMS

Wearable electronics take on a considerable role in the development of new personalized healthcare systems. A substantial number of wearable systems are designed to be worn during regular daily activity in order to offer not only smart functions but also to provide information about health and wellbeing through continuous monitoring.

This type of devices can be worn on the body as implants or integrated with medical garments and fashion accessories. Monitoring of body motion as well as tracking key physiological parameters like respiration rate, heart rhythms, blood pressure, and body temperature, represent very significant means in disease diagnosis and preventative intervention. Getting a change of healthcare system from a conventional hospital-centered system to a personalized one represents the main purpose in the development of wearable systems.

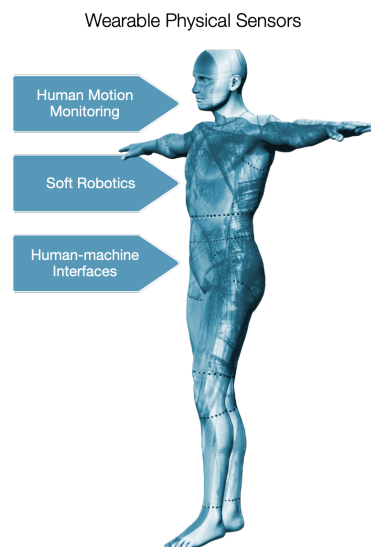


Figure 1: Application areas of wearable physical sensors.

The flexibility and stretchability ensure strong and conformal contact with curvilinear and irregular surface of human skin, so that the working state of the devices is not affected during daily activities. For this purpose, there has been a growing demand for wearable systems which can be properly attached to human skin or integrated with textiles in order to detect physiological parameters of human body.

To meet the above-mentioned requirements, it is important to develop electronics that can undergo large strain to accommodate the stretching of human skin or garments on which it is integrated. Wearable systems can be made flexible and stretchable depending on accurate material selection and structure design.

## 1.2 ACTIVITY MONITORING

There is a growing interest in development of devices with electronic materials and innovative sensing technology. In particular, strain sensors with high stretchability represent important means for a wide number of applications including human activity monitoring. Measurements of body motion are required in healthcare services and in professional and amateur sports for providing assessment of human motion wellness. In the healthcare field, motion data is used for diagnosis and rehabilitation as well as in sport science it is significant for athletes' physical therapy and training.

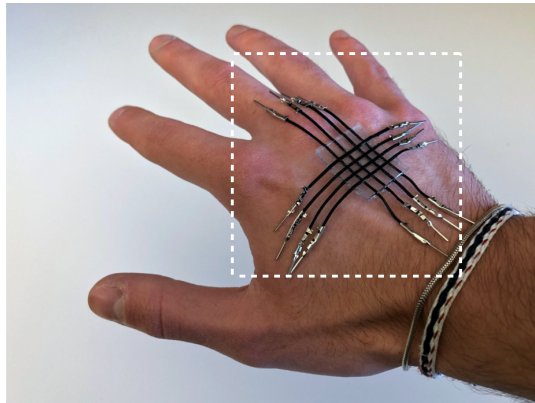


Figure 2: Example of stretchable sensor manufactured with 3D printed conductive TPU fibers embedded into a PDMS substrate.

In the recent research some wearable strain sensors have been developed to be used to monitor the bending and unbending state of joints as well as acquire biomechanical parameters in specific parts of the human body. An important feature of stretchable sensors is the ability to stretch with movements without structural damages, particularly when large-scale body movements occur. This fact means this kind of sensors should show high stretchability, up to  $\approx 50\%$ , to properly accommodate the tensile strain due to body motion.

Following this aim, the conducted research study is part of the advancement related to the development of highly stretchable strain sensors for wearable applications.

## 2.1 STRETCHABLE STRAIN SENSORS

Stretchable strain sensors are characterized by several different parameters. Stretchability is a fundamental mechanical parameter indicating the maximum strain at which sensors can continue working properly. When sensors get above this mechanical limit, they are not able to show desired reproducibility at the related strain value. Most intrinsically conductive materials such as metals, silicon, and conducting polymers do not show large stretchability. For instance, conventional metallic strain gauges generally exhibit poor stretchability ( $\approx 5\%$  strain). By combining these intrinsically conductive materials with flexible and stretchable materials or incorporating specific structure designs, high stretchability can be achieved. Stretchability can change depending on mechanical properties of substrates, material selection, structure design, and fabrication process.

Sensitivity represents the main parameter to characterize sensors. For strain sensors, the ratio of relative electrical resistance or capacitance signal change to the applied strain is defined as gauge factor (GF). Stretchable sensors should have high GF values, i. e. high sensitivity. When resistive and capacitive strain sensors are stretched, they mostly elongate in the loading direction and contract in the transverse direction. For this reason, geometrical effect is the main mechanism responsible for changes of their electrical properties.

### 2.1.1 *Performance Parameters*

- Stretchability

The high stretchability is the first feature which compares both resistive strain sensors and capacitive strain sensors.

- Sensitivity

Resistive sensors can reach high sensitivity, i. e. high GF values, as long as a lower stretchability leading to a reduced value of maximum strain level. They show a corresponding decrease of GF when the strain level is induced to increase. Capacitive sensors are characterized by low GF values which get closer unity in the best cases, but they can withstand high levels of applied strain.

- Linearity

Capacitive sensors exhibit excellent linearity which is the basic parameter related to the calibration process of sensors. On the other side, most resistive sensors exhibit a nonlinear behavior since an inhomogeneous change occurs within the sensing structure when strain is applied. Also, they exhibit larger overshooting behavior if compared with capacitive sensors.

- Hysteresis and Response time

When a state of dynamic strain is applied, capacitive sensors results more suitable due to their better values of hysteresis and response time. These two parameters can be straight related to the materials of sensors because of the viscoelastic nature of polymers.

- Noise and SNR

Capacitance signal of sensors can be affected by EM interference and fringe fields generated from anything conductive object, including biological tissue. For this reason, any expedient on the structure of sensor is needed to address that issue. Also, high baseline capacitance values give strength the sensor to parasitic capacitance and crosstalk improving signal-to-noise ratio.

- Durability and Drifting behavior

Both capacitive and resistive sensors have good stability in terms of dynamic durability and drifting behavior during the usage time.

Achieving high sensitivity and stretchability simultaneously is a difficult target for the development of stretchable sensors. Moreover, most of the sensors are designed to mainly detect uniaxial strain, which limits inevitably their applications. Strain sensors designed with isotropic conductive networks respond similarly to strain in different directions, not allowing to distinguish multiple strains. In many applications it would be necessary to detect complex multi-axial strain conditions like human skin does. A possible solution would be to design sensors in order to get assembled devices which are able to detect independently omnidirectional strain. Alternatively, intrinsically anisotropic conductive networks can be designed to achieve independent responses to applied strain in different directions.

For stretchable sensors, performance parameters such as linearity, hysteresis, and durability are significant considerations during the design process. Linearity indicates how closely the electrical signal changes of the sensors follow a linear relationship with deformation. High linearity simplifies the calibration process which is essential for a sensor device for providing reliable readings.

Generally, conventional metallic sensors exhibit excellent linearity since their gauge factors depend on Poisson's ratio only. Instead, for many composite-based sensors, linearity can be low since electrical signal changes are attributed to several mechanisms. In addition, some sensors can exhibit multiple-linear regions.

It is important for the wearable sensors, either worn directly on skin or as accessories, to remain stable under different conditions, because their working can be influenced by physical or chemical contact with the external environment. The development of an integration strategy for the sensors is needed to achieve high reliability and continuing monitoring capability.

## 2.2 SENSING MECHANISM

Two main groups of strain sensors can be distinguished on the basis of their sensing mechanism. The most investigated strain sensors base their work principle on electrical resistance and capacitance change. It means electrical signal change represents the sensing signal and is related to the applied strain.

Even though both types use electrical signal changes, the physical effect which explains the working principle is different. The two groups of sensors are characterized by different parameters, so that sometimes sensors of the first type can be preferable than the second ones, whereas in other situations sensors of the second type could work better, depending on the required applications.

### 2.2.1 Piezoresistivity

The fundamental principle of piezoresistive sensors comes from the following equation

$$R = \rho \frac{L}{A} \quad (1)$$

where

- $R$  sensor resistance ( $\Omega$ )
- $L$  sensor length of the sensor (m)
- $A$  sensor cross-section area ( $\text{m}^2$ )
- $\rho$  electrical resistivity of the conductive material ( $\Omega \text{m}$ )

The resistance value increases when the resistive sensor is subjected to elongation in length and shrinkage in cross-section area.

Taking natural logarithm on both sides yields

$$\ln(R) = \ln(\rho) + \ln(L) - \ln(A) \quad (2)$$

The differential of the aforementioned equation becomes

$$\frac{dR}{R} = \frac{d\rho}{\rho} + \frac{dL}{L} - \frac{dA}{A} \quad (3)$$

The first term on the right side of the equation is due to changes in specific resistivity of the material. Its physical effect is governed by the electrical conduction mechanism in the solid; thus, its magnitude is very different in metals and metal alloys compared to semiconducting materials.

Considering the diameter  $D$  of a conductor and taking the natural logarithm of equation  $A = \pi D^2/4$

$$\ln(A) = \ln(\pi/4) + 2 \ln(D) \quad (4)$$

The differential of both sides results

$$\frac{dA}{A} = 2 \frac{dD}{D} \quad (5)$$

Then, considering

$$dD/D = \varepsilon_t \quad \text{with } \varepsilon_t \text{ the transverse or lateral strain}$$

$$dL/L = \varepsilon \quad \text{with } \varepsilon \text{ the longitudinal strain}$$

$$\nu = -\varepsilon_t/\varepsilon \quad \text{with } \nu \text{ the Poisson's ratio}$$

Equation 3 can be rewritten as

$$\frac{dR}{R} = \frac{d\rho}{\rho} + (1 + 2\nu) \varepsilon \quad (6)$$

establishing the basic relationship between resistance and strain.

The measure of sensitivity of the material, i. e. its resistance change per unit of applied strain, is defined by the gauge factor ( $GF$ ). For a resistive sensor, the strain gauge factor arising from piezoresistive effect is given by:

$$GF = \frac{\Delta R/R_0}{\varepsilon} = (1 + 2\nu) + \frac{\Delta\rho/\rho_0}{\varepsilon} \quad (7)$$

where

$\Delta R$  resistance change

$R_0$  initial resistance

$\Delta\rho$  resistivity change

$\rho_0$  initial resistivity

The first term  $(1 + 2\nu)$  of Equation 7 describes the contribution by geometric effects since it directly relates to the Poisson effect, which is the tendency in an elastic material to contract laterally in response to axial stretching. The second term denotes the contribution due to the intrinsic piezoresistivity of the materials, representing the changes in specific resistivity of the material in response to the applied strain.

### 2.2.2 Capacitance

A capacitor is a passive electrical component that can store energy in the form of an electric field. Parallel-plate capacitors have an arrangement of two conducting plates acting as electrodes and a dielectric between them which acts as a nonconducting separator for the plates. Capacitance, in a typical parallel-plate arrangement, can be defined in terms of charge storage

$$C = \frac{Q}{V} \quad (8)$$

where

- $C$  capacitance in farads (F)
- $Q$  charge in coulomb (C)
- $V$  voltage difference between the two plates (V)

The plates have equal and opposite charges.  $V$  can be expressed in terms of the work done on a positive test charge  $Q$  when it moves from the positive to the negative plate

$$V = \frac{\text{work done}}{\text{charge}} = \frac{F d}{Q} = E d \quad (9)$$

where

- $F$  force (N)
- $d$  distance between two parallel plates (m)
- $E$  electric field ( $\text{V m}^{-1}$  or  $\text{N C}^{-1}$ )

The unit of capacitance, the farad, is a large unit; practical capacitors have capacitances in microfarads ( $\mu\text{F}$  or  $10^{-6}$  F), nanofarads (nF or  $10^{-9}$  F), and picofarads (pF or  $10^{-12}$  F). Capacitive sensors are variable capacitors, that is, their capacitance changes during the sensing process.

Capacitance is function of geometry, relative permittivity of the dielectric medium (dielectric constant), plate materials, and plate configuration. In the case of capacitors with a parallel-plate configuration, the capacitance is given by

$$C = \frac{\epsilon A}{d} = \epsilon_0 \epsilon_r \frac{A}{d} \quad (10)$$

where

- $A$  area of the plates ( $\text{m}^2$ )
- $d$  distance between the plates (m)
- $\epsilon$  permittivity of the medium between the plates
- $\epsilon_0$  vacuum permittivity ( $8.854\,188 \times 10^{-12}$   $\text{F m}^{-1}$ )
- $\epsilon_r$  relative permittivity of the medium between the plates

The capacitance value depends on the parallel area of the two electrodes ( $A = lw$ , where  $l$  and  $w$  are the length and the width of the electrodes), and the distance between them ( $d$ ) that corresponds to the thickness of the dielectric layer between the electrodes. Hence, the electrical signal change relates to the change of the geometry factor  $A/d$ : changes of geometrical dimensions due to stretching lead to changes in the capacitance value.

The inverse relationship between the spacing  $d$  and the capacitance  $C$  leads to a large change in capacitance value with a small spacing change. Spacing-variation-based capacitive sensors are generally more sensitive, but only suitable for a small displacement range (usually the spacing variation is less than the electrode size and in the range of micrometers). On the other hand, area-variation-based sensors are less sensitive, but suitable for a larger displacement range.

For a parallel-plate capacitive sensor, subjected to stretching deformation  $\varepsilon$  parallel to the electrodes, along the strain direction the length of the electrodes increases to  $(1 + \varepsilon)l$ , while the width of the electrodes and the separation between the two electrodes decrease to  $(1 - \varepsilon\nu_e)w$  and  $(1 - \varepsilon\nu_d)d$ , respectively, where  $\nu_e$  and  $\nu_d$  denote the Poisson's ratio of the electrodes and the Poisson's ratio of the dielectric layer. Capacitance after the tensile strain can be defined

$$C = \varepsilon_0 \varepsilon_r \frac{(1 + \varepsilon)l (1 - \varepsilon\nu_e)w}{(1 - \varepsilon\nu_d)d} \quad (11)$$

The strain gauge factor ( $GF$ ) arising from change in the capacitance is given by

$$GF = \frac{\Delta C/C_0}{\varepsilon} = \frac{1 - \varepsilon\nu_e}{1 - \varepsilon\nu_d} + \frac{\nu_d - \nu_e}{1 - \varepsilon\nu_d} \quad (12)$$

where

$\Delta C$     capacitance change  
 $C_0$     initial capacitance

If the electrodes and dielectric layer have the same Poisson's ratio  $\nu_e = \nu_d$ , strain sensitivity i. e.  $GF$  approximates the unity as follows

$$GF = \frac{\Delta C/C_0}{\varepsilon} \approx \frac{(1 + \varepsilon)C_0 - C_0}{\varepsilon C_0} = 1 \quad (13)$$

while in case of  $\nu_e < \nu_d$ , it will be always beyond unity.

## 2.3 STRETCHABLE SENSORS DESIGN

For stretchable sensors, high gauge factor values are desired in order to achieve high signal-to-noise ratio. Since gauge factors depending only on the geometric changes have low values, to increase the value of sensitivity, according to Equation 7 on page 8, the contribution of the second term should be improved. Also, the conductive networks should not be altered in order to preserve electrical conductivity, while the flexible and stretchable substrates accommodate the applied strain.

Strain sensors based on nanocomposites show higher sensitivity than common metal-based strain sensors since their electrical resistance is strongly affected by several mechanisms including intrinsic piezoresistivity of the nanomaterials, separation of the conductive nanomaterials, and tunneling effects. Generally common nanomaterials are characterized by negligible deformation, therefore the contribution due to their intrinsic piezoresistivity is relatively small. When strain due to the mechanical deformation occurs, a disconnection between nanomaterials takes place. This event produces a rise in resistance since it affects the normal flowing of electrons through adjacent nanoparticles. The size of the effect depends on the concentration level of the nanoparticles in the nanocomposites since if the nanoparticles are highly overlapped or in close contact (distance between nanoparticles is less than the tunneling cutoff distance) it is more difficult to influence the conductive networks. Hence, the strain sensitivity of nanocomposites generally increases when the content of conductive nanomaterials decreases.

Other mechanisms have been explored in order to enhance the sensitivity of strain sensors. Among these, the cracking mechanism is certainly worth mentioning. It is based on the intentional creation of a cracked pattern in the conductive thin film which is deposited on the stretchable substrate.

Kang et al. [5] mimicked the structure of spider's sensory system by depositing 20 nm thick Platinum on PU acrylate, creating controlled cracks with different density and direction. The formation of high density cracks under stretching results in significant increase of resistance as well as higher gauge factor values. Although this mechanism brings advantages in terms of sensitivity, the process for the creation of cracked patterns can be tricky and the sensing range relatively low.

### 2.3.1 *Material Design*

- *Elastomer-based sensors*

An effective method for sensors design is based on the direct incorporation of conductive materials inside an elastomeric matrix.

The conductive fillers offer electrical function while the insulating elastomeric substrates offer support to the applied load. When the fillers are uniformly dispersed in the elastomeric matrix and the concentration of fillers reaches their percolation threshold concentration, the conductive network can form. The difficulty relates to the development of a suitable technique to improve the dispersion of the conductive fillers inside the elastomeric matrix since conductive materials are usually not compatible with elastomers and tend to create agglomerates in the matrix.

For instance, strain sensors with high conductivity can be produced by solution mixing of PU and the conducting polymer PEDOT:PSS. At the end of the process a homogeneous dispersion of PEDOT:PSS in PU matrix is obtained, resulting in PU/PEDOT:PSS composite fibers of high electrical conductivity. Similarly, highly stretchable strain sensors and conductive fibers can be developed by wet spinning of homogenous solution of PU and CNTs or PU and AgNPs. PDMS is another type of highly stretchable polymer which is widely used to create sensors or conductors. Conductive nanomaterials including carbon black, CNFs, and graphene can be dispersed in PDMS prepolymer leading to final polymer composites with high electrical conductivity.

To achieve homogenous dispersion of the conductive nanomaterials in the matrix, physical or chemical surface functionalization can be required. High loading of dispersed conductive fillers is necessary to ensure high electrical conductivity, but it could negatively influence the stretchability. Furthermore, the sensitivity of composites should increase upon decreasing the conductive filler content and the highest value should occur at a filler concentration near the percolation threshold.

To overcome issues due to low compatibility between conductive materials and elastomeric matrix, the design of segregated electrically conductive network can be considered. This method allows to use lower concentration of conductive nanomaterials due to a lower percolation threshold providing in any case high electrical conductivity. Sensors based on this type of design show high piezoresistive sensitivity and electrical conductivity due to the presence of segregated conductive structures.

Lin et al. [6, 7] reported the design based on the formation of segregated nanostructured conductive graphene networks in SBR composites for creating highly stretchable strain sensors with high sensitivity. The observed percolation thresholds are much lower than composites fabricated by common direct mixing method.

Sang et al. [11, 12] fabricated highly stretchable strain sensors using TPU with low-fraction CNTs: interconnected conductive networks are created by mixing PU particles with CNTs, which subsequently segregate at the particle interfaces. Other types of segregated CNTs networks can be created using pulverized PDMS particles as the “self-segregated” phase [13]: CNTs are located in the continuous PDMS phase, resulting in an extremely low percolation threshold.

Stretchable sensors can be also prepared using preconstructed conductive networks such as porous carbon nanostructures, carbon nanomaterials/metal hybrid sponges, foams or sponges coated with conductive particles, and metal nanowire gels. A subsequent filling of elastomers inside the porous structures of the 3D conductive networks is useful to improve the final mechanical integrity and stability of the structures: for instance, the liquid PDMS prepolymer can be used to permeate the 3D graphene porous structures [15, 16] creating highly conductive and stretchable sensors with high sensitivity.

The transfer of conducting materials onto elastic polymer substrates is a common method used to fabricate mainly thin skin-like electronic materials. Conductive nanoparticles can be deposited or coated through solution coating including spin coating, dip coating, spray coating, drop casting, and tape casting, creating conductive thin films. Also, printing methods find wide application due to their quick processing time. PDMS is considered one of the most suitable polymer substrates due to its low stiffness and chemical stability. For instance, sensors based on super-aligned CNT (SACNT) thin films, with CNTs aligned along the orthogonal direction to the stretching direction and directly coated on PDMS substrates, show extremely high sensing strain range as well as excellent durability [18]. As in this case, where PDMS is hydrophobic and chemically inert, a method to improve the interfacial adhesion is usually required. For this purpose, it is necessary to utilize one of the two possible strategies: surface functionalization of the substrate and use of a binder for the conductive film. Although the improved adhesion between conductive films and polymer substrates, their different surface and mechanical properties can cause events of debonding or delamination under high cyclic loading-unloading conditions.

- *Conductive polymer-based sensors*

High conductivity and low insulating content are desired in the design of this type of sensors.

On the other hand, a high degree of disorder of polymer chains is advantageous to improve deformability by creating a large free volume for polymer chains movement. Among the processable conducting polymers, the conductive polymer PEDOT:PSS shows very high electrical conductivity [14]. Due to the semicrystalline nature of PEDOT and PSS, it is necessary to incorporate some additives to enhance the stretchability of the polymer film, even though it should be noted that incorporation of additives causes a decrease of conductivity. Ionic additives can be effective for this purpose since they connect PEDOT-rich domains, promoting higher crystallinity, and make softer PSS domains, leading to both enhanced electrical conductivity and high stretchability.

- *Hydrogel-based sensors*

Soft hydrogels can be also employed in the design of stretchable sensors due to their excellent properties of flexibility and stretchability. Conductive hydrogels are classified in two main types: hydrogels made by intrinsically conductive materials such as conducting polymers, carbon nanomaterials or metal nanowires and ionic hydrogels prepared by adding polyelectrolytes.

The challenge relates to achieve high electrical conductivity in addition to good mechanical properties. Indeed, it is necessary to find a method for including conductive nanomaterials in the matrices of polymeric hydrogels, since nanomaterials usually tend to create agglomerates and show a certain resistance to be dissolved. The hydrogels adopted for these applications should be tough, while common hydrogels are soft and brittle, moreover they are characterized by high amount of water, so that can dehydrate or freeze in cold environments leading to lose conductivity. To prevent freezing, organic solvent can be used to replace pure water of common hydrogels. To overcome the problem of dehydration, hydrogels can be wrapped by a thin elastomer layer acting as water barrier keeping hydrogels moist and flexible. Also, adding hygroscopic fillers helps with retention of water in hydrogels under dry conditions. These cautions are needed to obtain hydrogels with unvaried flexibility, conductivity, and strain sensitivity.

- *Textile-based sensors*

Textile materials are able to provide high flexibility and stretchability when undergo stretching, shearing, and twisting deformations. For the application of wearable sensors the textiles need to be conductive since the common textile materials are electrically insulating. Textiles are processed from fibers by weaving, knitting, or embroidery techniques.

There are many different developed techniques to fabricate conductive textiles including integration of metal filaments with yarns, coating fibers with a thin layer of conductive materials as well as printing of conductive materials onto the surface of textiles, and direct patterning of conducting polymers. In particular, the method based on coating fibers with conductive materials makes possible preservation of mechanical properties of the fibers and high electrical conductivity.

For instance, elastic PU fabrics coated with reduced graphene oxide, lead to flexible and stretchable conductive fabrics with high sensitivity and large strain range [2]. At the same time the coating does not seem to influence the mechanical properties of the fabrics. Common issues that usually occur, are the increase of the fabrics' stiffness due to inclusion of metal filament in the yarns as well as the high electric resistance change of printed conductive materials during deformation because of changes of the porous textile structures. The most difficult problem of the coated fabric-based sensors are due to the degradation of the coating layer which could crack or detach from the sensor's surface after high cyclic loading-unloading or large strain conditions. Therefore, it is necessary to improve the bonding between coatings and textile fibers. Plasma treatment can be an effective solution to improve the adhesion between coating and fabric surface. It creates reactive groups on the fabric surface which form interactions with coating materials.

### 2.3.2 Structure Design

- *In-plane stretchable configurations*

In-plane stretchable configurations are usually created using metal wires in order to form conductive thin films with specific layouts. The join of conductive films with elastomeric substrates rises the capability of the structure to undergo large strains, even though the stretchability is limited by the adhesion between wires and substrate, by the substrate stiffness, and by structural failure caused by local stress concentration of wires. Despite the stiffness values of metals, they are able to bear bending as long as cross sections are sufficiently small: as known, thinner wires can be stretched more than wider ones.

The two most developed 2D metal wire structures are serpentine structures and fractal-based structures. The stretchability of a periodic serpentine structure depends on the extension capability of its "2D spring" structure.

However on the crests and troughs, points of the serpentine structure where the highest local stress concentration occurs, formation of cracks leading to failure of the structure is very probable. For this reason, structure design with uniform stress distribution is desirable: 3D coil structure shows a more uniform stress distribution than 2D coil structure, resulting in higher stretchability. Fractal-based structures can be also designed to accommodate high strain along a chosen direction due to their self-similarity layouts. These usually exhibit a higher stretchability if compared to serpentine structures.

- *Out-of-plane wavy structures*

Another alternative method of structure design is to make thin films or ribbons into out-of-plane buckles. The conductive structures can be made by metals or conductive nanomaterials. When the structures are stretched, the conductive layout remains unchanged providing effective conductivity while the substrate accommodates large deformation. Ordered wavy structures can be created by bending thin metal films on an elastomeric substrate due to the thermal expansion mismatch between the two different materials. A reported example is a thin metal film deposited on a PDMS substrate while it undergoes a thermal expansion. The buckled structure forms in the metal film because of the compressive stress generated by the subsequent cooling.

An alternative method is to deposit the conductive thin film or single fibers onto a prestrained elastomeric substrate. The subsequent relaxation of the substrate results in buckled structures that can withstand large deformation without leading significant loss of conductivity. Both the layer thickness and the level of prestrain influence the amplitude and wavelength of the wavy structures. Xu et al. [17] created buckled structures able to withstand large strain by using the prestrain strategy: a film of wavy CNTs ribbons is transferred onto a prestrained PDMS substrate and buckled out-of-plane upon releasing the strain.

Buckled structures can be also created by multiaxial prestrain. Ho et al. [4] reported biaxially stretchable AgNWs conductors by prestretching the PDMS biaxially. In addition to the uniaxial and multiaxial prestretching, Mu et al. [10] reported a method based on the creation of periodic hierarchical graphene wrinkles which ensure high conductivity also under large strain conditions.

- *Open structures*

Using open-mesh structures with different shapes represents a valid solution to achieve high stretchability due to the particular geometry of the holes. When mesh structures are stretched, the open holes deform with the strips rotating toward the stretching direction to accommodate the deformation while stress rises at the connected vertex of the structures. 3D printing techniques allow fabrication of composites with different open mesh structures including rhomboid mesh, square mesh, and hexagonal mesh.

For instance, stretchable electrodes based on rhomboid CNTs mesh films were developed [1], where the rhomboid structure enabled to accommodate strain providing high stretchability. Among the different nanocomposites, the PDMS nanocomposites with rhomboid mesh showed excellent deformation capability [9].

Particular open structures consist of patterns of thin-line cuts on conductive thin films. By setting the pattern of cuts, the structure can be characterized with desired mechanical properties, achieving high stretchability. However, the stretchability can be negatively influenced by different factors including film thickness, small cut lengths, and large spacing between the cuts.

3D porous structure is another type of design which is able to accommodate large strain due to the local bending of pore walls of the structure. Li et al. [3] and Zhu et al. [8] reported fabrication methods to create pores in PDMS composites to improve stretchability and sensing performance. A subsequent coating of the 3D porous PDMS with conductive fillers allows to get high conductivity as well.



Part II

---

CONCEPTUAL AND PRACTICAL  
DEVELOPMENT



CHAPTER THREE

---

## 3.1 CONDUCTIVE POLYMER MATRIX COMPOSITES

Polymer composites are multi-phase materials in which reinforcing fillers are embedded into a polymer matrix. PDMS is a wide-used polymer, characterized by interesting properties of flexibility, optical transparency, and biocompatibility, offering low cost, simple fabrication, and simple process. Indeed, the liquid uncured PDMS can be molded easily. Furthermore, PDMS is a very suitable material to be used in the wearable applications, since its properties of high stretchability, flexibility, and softness. PDMS-based materials are intrinsically not conductive, but by mixing conductive particles with the base polymer, conductivity can be achieved.

A certain number of recent studies have been carried out in the development of reinforced composites by using micro- and nanoparticles embedded into the PDMS matrix. Different types of conductive fillers have been used to prepare conductive PDMS-based composites, for instance using organic fillers such as carbon black (C-PDMS) and multi-walled carbon nanotube (MWCNT-PDMS), or inorganic fillers such as metallic particles.

Metallic fillers have the advantage to lead to high conductivity values, but on the other hand these can be difficult to disperse into polymeric matrix because of the large difference in density between the particles and the base polymer.

The present work introduces a facile method to create conductive sensing structures by using PDMS-based composites, made conductive by mixing metallic particles. In particular, the fabrication process focuses on conductive composites based on the use of silver microparticles as reinforcing phase, dispersed into the PDMS polymer phase homogeneously.

## 3.2 CONDUCTIVE PERCOLATION NETWORK

Micro/nano conductive fillers can be embedded into insulated polymers to create current percolating pathways. The resistance variation of these pathways is mainly due to the changes in inter-filler resistance, whereas intra-filler resistance can be negligible. This suggests the connection between conductive fillers in composites produces piezoresistive effect.

Although the mechanical reinforcement of composites using a filler should be characterized by homogeneous dispersion and high adhesion between filler and matrix, the electrical conductivity of composites is based on the formation of conductive paths. Using conductive particles as reinforcement phase in an insulating polymer matrix can alter the electrical properties of the host matrix, inducing electrical conductivity at low volume concentration of the filler. The percolation theory can explain effectively the electrical conductivity of polymeric composites.

According to the percolation theory, a certain value of fillers volume, which makes an insulating composite conductive, can be estimated. That value corresponds to the critical volume fraction of filler, also known as the percolation threshold, and in correspondence of that the electrical conductivity of the composite suddenly increases by several orders of magnitude. As long as the concentration of fillers does not achieve a high enough value to form a first conductive network, the particles stay completely separated into the matrix and no continuous network is created. The formation of multiple conductive paths induces a sudden increase of conductivity until its maximum value and subsequent increases in concentration of fillers have a negligible effect on the conductivity of the composite.

The electrical conductivity of the composite can be expressed using the power-law relationship

$$\sigma = \sigma_0 (\phi_f - \phi_c)^t \quad (14)$$

where

- $\sigma$  composite conductivity ( $\text{S m}^{-1}$ )
- $\sigma_0$  filler conductivity ( $\text{S m}^{-1}$ )
- $\phi_f$  volume fraction of filler
- $\phi_c$  critical volume fraction, i. e. percolation threshold
- $t$  critical exponent

Equation 14 is valid only for concentrations of filler higher than the percolation threshold, i. e.  $\phi_f > \phi_c$ . The value of the exponent  $t$  is related to the formation of continuous clusters through the composite above the critical volume fraction and needs to be evaluated by experimental methods.

It is noted the above-mentioned relationship shows a non-linear behavior because one parameter is proportional to another one to some power

$$y = K x^b \quad (15)$$

where both the factor  $K$  and the exponent  $b$  are constant.

The relationship can be graphically represented by logarithmic scale for both the conductivity values  $\log(\sigma)$  and the volume fraction differences  $\log(\phi_f - \phi_c)$ . Taking the natural logarithmic on both sides of Equation 14 yields

$$\log(\sigma) = \log \left[ \sigma_0 (\phi_f - \phi_c)^t \right] \quad (16)$$

According to the logarithmic properties, it can be rewritten as

$$\log(\sigma) = \log(\sigma_0) + \log(\phi_f - \phi_c)^t \quad (17)$$

So that, the linear relationship is obtained

$$\log(\sigma) = \log(\sigma_0) + t \log(\phi_f - \phi_c) \quad (18)$$

corresponding to the linear equation  $y = mx + b$ , where

$$m = \frac{d \log(y)}{d \log(x)} = \frac{d \log(\sigma)}{d \log(\phi_f - \phi_c)} = t \quad (19)$$

$$b = \log(\sigma_0) \quad (20)$$

are the slope and the y-intercept, respectively.

When the best linear fit is obtained, it is possible to estimate the value of the percolation threshold and the critical exponential as well. It means Equation 14 on the preceding page provides a strong mean to estimate the dependence of the electrical conductivity of composites with the concentration of conductive particles.

The estimated value of percolation threshold has great experimental relevance: since the filler has usually a much higher cost than the polymeric material, producing conductive composites with reduced values of critical volume of filler can be extremely advantageous.

The 3D percolation threshold depends on the filler morphology as well as dispersion and distribution characteristics of the filler clusters. Generally, a higher aspect ratio for the fillers leads to lower percolation thresholds, as in the case of NWs and nanotubes. Instead, for spherical particles, the aspect ratio is equal to 1. In addition, the levels of dispersion and distribution of the fillers need to be considered during the fabrication of the composite. Different dispersion and distribution of fillers completely affect the conductivity of the polymeric composite. Since the formation of conductive paths is the final aim, fillers should homogeneously dispersed into the matrix, whereas the distribution of fillers should not be uniform because it would increase distance between the conductive particles. For this reason, preferential distributions of fillers are desirable in order to form conduction paths. Different possibilities in terms of dispersion and distribution of fillers are shown in Figure 3.

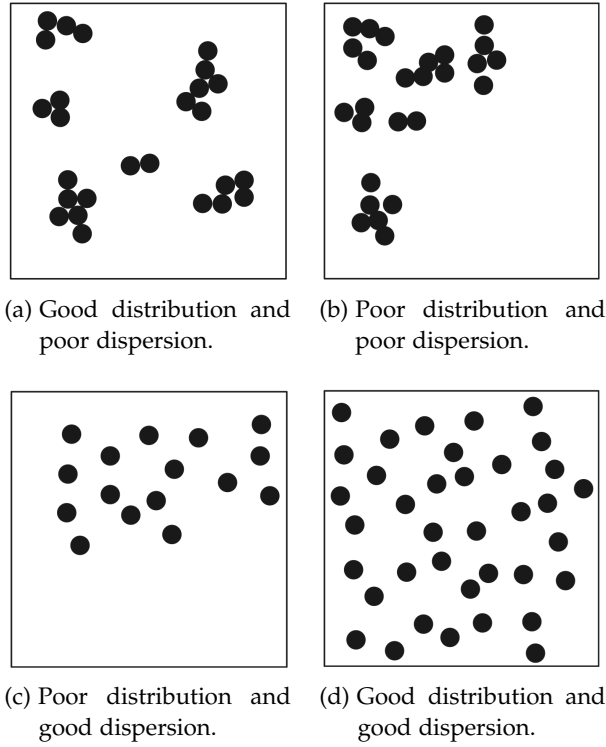


Figure 3: Illustration of the difference between dispersion and distribution.

Since Equation 14 on page 22 do not take into account of many factors such as particles dispersion, particles shape, particles orientation, and particles-matrix interaction, the values of the exponent  $t$  and the percolation threshold  $\phi_c$  are not constant, whereas depend on the particular composite and have to be determined through experimental methods by fitting experimental data.

### 3.3 COMPOSITE FABRICATION METHOD

The increase of the weight content of conductive filler reduces the electrical resistivity of the composite which results in an enhanced electrical conductivity because more interconnected clusters of silver particles are created into conduction paths.

For the filler, the volume fraction can be calculated according to

$$\phi_f = \frac{V_f}{V_f + V_m} = \frac{\frac{m_f}{\rho_f}}{\frac{m_f}{\rho_f} + \frac{m_m}{\rho_m}} \quad (21)$$

and the corresponding mass fraction<sup>1</sup> is calculated by

$$w_f = \frac{m_f}{m_f + m_m} \quad (22)$$

<sup>1</sup> also known as weight fraction wt, often defined in terms of weight concentration wt%, where wt = wt%/100.

It allows to obtain the two quantities related to the polymer matrix as follows

$$\phi_m = 1 - \phi_f \quad (23)$$

$$w_m = 1 - w_f \quad (24)$$

where

- $V_f$  volume of filler
- $V_m$  volume of polymer matrix
- $m_f$  mass of filler
- $m_m$  mass of polymer matrix
- $\rho_f$  density of filler
- $\rho_m$  density of polymer matrix

Herein, considering the Ag particles as fillers and the PDMS as polymer matrix, Equation 21 on the preceding page and Equation 22 on the facing page are rewritten as

$$\phi_{Ag} = \frac{V_{Ag}}{V_{Ag} + V_m} \quad (25)$$

$$w_{Ag} = \frac{m_{Ag}}{m_{Ag} + m_m} \quad (26)$$

Since, during the preparation of composites, it is easier to deal with the weight concentration wt%, the weight fractions need to be converted to volume fractions.

Once the weight concentration of filler wt<sub>Ag</sub>% is set, the volume fraction of the filler can be calculated by

$$\phi_{Ag} = \left[ \frac{\rho_{Ag}}{\rho_m} \left( \frac{1}{w_{Ag}} - 1 \right) + 1 \right]^{-1} \quad (27)$$

where the following density values are considered

- $\rho_{Ag} = 10.49 \text{ g cm}^{-3}$  density of silver
- $\rho_m = 1.0 \text{ g cm}^{-3}$  density of PDMS matrix

The volume fraction of the matrix is then calculated by Equation 23. Therefore, considering the total volume of the composite  $V_C$

$$V_C = V_{Ag} + V_m \quad (28)$$

the volume values can be calculated as follows

$$V_{Ag} = \phi_{Ag} V_C \quad (29a)$$

$$V_m = \phi_m V_C \quad (29b)$$

Then, the mass of the filler and the mass of the polymer matrix can be determined, respectively

$$m_{Ag} = \rho_{Ag} V_{Ag} \quad (30a)$$

$$m_m = \rho_m V_m \quad (30b)$$

Moreover, the mass of the PDMS base  $m_{PDMS}$  and the mass of the crosslinker agent  $m_{agent}$  are calculated from the mass of the matrix

$$m_m = m_{PDMS} + m_{agent} \quad (31)$$

according to the fixed weight ratio 10:1 between base and crosslinker

$$m_{PDMS} = (10/11) m_m \quad (32)$$

$$m_{agent} = (1/11) m_m \quad (33)$$

The density of the composite can be calculated based on the density and the volume fraction of the constituents as follows

$$\rho_C = \rho_{Ag} \phi_{Ag} + \rho_m \phi_m \quad (34)$$

Equation 34 can be also expressed as dependent only on the filler parameters. Considering Equation 23, 30a, and 30b, it can be rewritten

$$\begin{aligned} \rho_C &= \rho_{Ag} \phi_{Ag} + \rho_m \phi_m = \rho_{Ag} \phi_{Ag} + \rho_m \left( \frac{V_m}{V_m + V_{Ag}} \right) \\ &= \rho_{Ag} \phi_{Ag} + \frac{m_m}{\frac{m_m}{\rho_m} + \frac{m_{Ag}}{\rho_{Ag}}} = \rho_{Ag} \phi_{Ag} + \frac{m_m}{\frac{m_{Ag}}{\rho_{Ag}}} \left( \frac{\frac{m_{Ag}}{\rho_{Ag}}}{\frac{m_m}{\rho_m} + \frac{m_{Ag}}{\rho_{Ag}}} \right) \\ &= \rho_{Ag} \phi_{Ag} + \frac{m_m \rho_{Ag}}{m_{Ag}} \phi_{Ag} = \rho_{Ag} \phi_{Ag} \left( 1 + \frac{m_m}{m_{Ag}} \right) \\ &= \rho_{Ag} \phi_{Ag} \left( \frac{m_{Ag} + m_m}{m_{Ag}} \right) = \rho_{Ag} \phi_{Ag} \frac{1}{w_{Ag}} \end{aligned} \quad (35)$$

Finally, the resulting relationship is given by

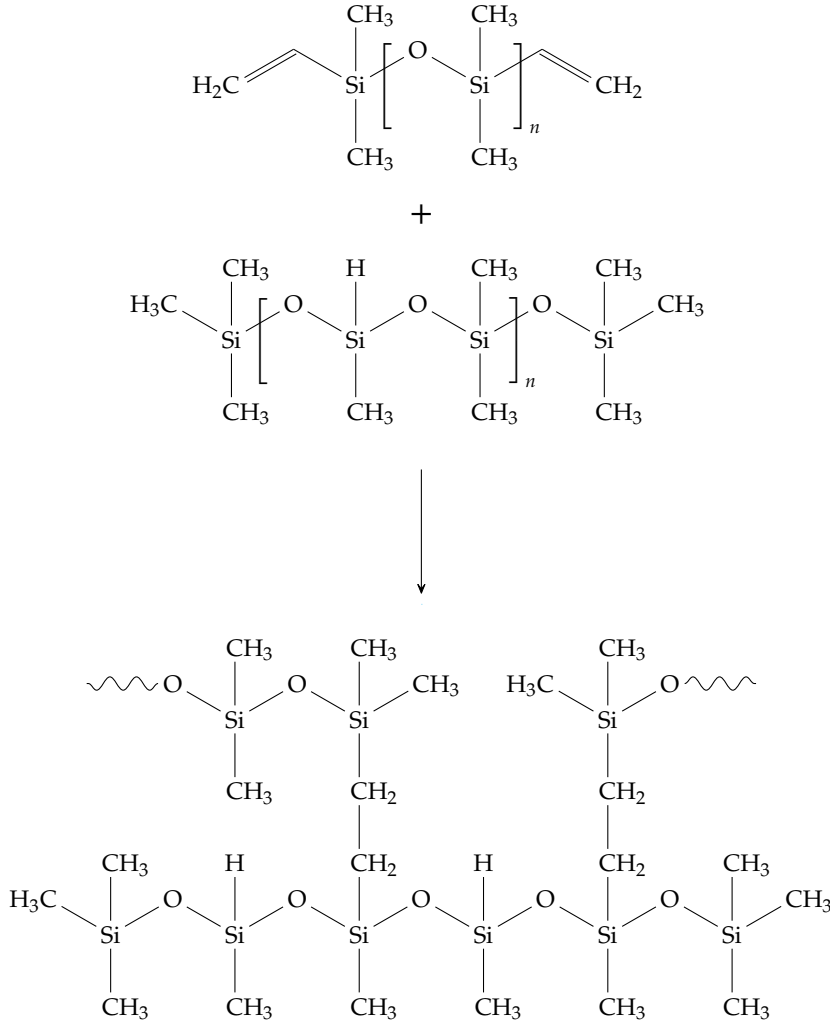
$$\rho_C = \frac{\rho_{Ag} \phi_{Ag}}{w_{Ag}} \quad (36)$$

### 3.3.1 Fabrication Process

The conductive composite is synthesized by mixing PDMS and silver particles in different concentrations to form Ag-PDMS. The used silver particles, with average diameter 2–3.5  $\mu\text{m}$ , are sold by Sigma-Aldrich, USA in form of Ag powder with purity of 99.9%.

Polydimethylsiloxane (Sylgard™ 184 Elastomer Kit, Dow Corning Co., USA), consisting of base elastomer (Part A) and curing agent (Part B). The base (Part A) consists of repeating  $-\text{OSi}(\text{CH}_3)_2-$  units and contain vinyl groups as final group.

The curing agent (Part B) contains silicon hydride  $-\text{O Si H CH}_3-$  units and has methyl groups as final group. During the thermal curing process, the curing agent acts as crosslinker of monomers, forming  $-\text{Si}-\text{CH}_2-\text{CH}_2-\text{Si}-$  linkages through the reactions between its silicon hydride groups and the vinyl groups of the monomers.



The Ag-PDMS composite is prepared by weighting the desired quantity of Ag powder and PDMS base elastomer on the basis of the chosen weight concentration of filler  $\text{wt}_{\text{Ag}}\%$ . The base polymer and the silver powder are manually stirred for few minutes in order to mix them properly.

After mixing the base polymer, the curing agent is added to the mixture in the weight ratio of 1:10, i. e. 1 part of curing agent in 10 parts of base elastomer and slightly mixed for few minutes. Then, the obtained mixture is degassed under vacuum for some minutes, typically up to 10 min, to remove any bubbles formed during manual mixing.



(a) Sigma-Aldrich silver powder.

(b) Conductive Ag-PDMS paste.

Figure 4: Composite created from Ag powder and PDMS polymer.

It is noted that the increase of the weight concentration of filler influences the density of the mixture, therefore the fabrication parameters in terms of mixing and degassing time can change, especially for much high values of  $wt_{Ag}\%$ .

After the vacuum degassing process, the composite is cured to form solid samples which are used for the subsequent electrical characterization of the composite. The two set up cure parameters are the cure temperature of  $80\text{ }^{\circ}\text{C}$  and the cure time of 30 min.

In order to carry out the percolation analysis of the composite, the fabrication process can be repeated for different values of filler concentration by changing the weight of silver powder added to the mixing step. For this purpose, the weight concentration of filler is changed in steps of 5%.

### 3.4 COMPOSITE ELECTRICAL CHARACTERIZATION

To characterize a composite material in terms of electrical conductivity is important to measure electrical resistivity, indeed the two quantities are related by an inverse relationship. The electrical resistivity of a material is an intrinsic physical property which describes how much the considered material resists the flow of electricity.

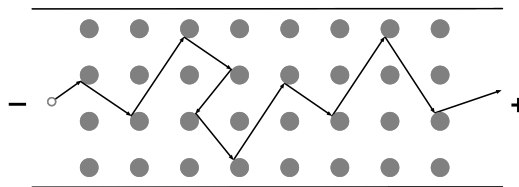


Figure 5: Electron flow inside a conductive material.

If electrons can flow easily through a material, the material has low resistivity, whereas if they have great difficulty flowing through that, the material shows high resistivity. Since conductivity describes how great electrons flow through the material, high conductivity is the same as low resistivity as well as low conductivity is the same as high resistivity. It means that from the analysis of the material in terms of resistivity, the conductivity analysis can be done by taking the inverse of resistivity.

Tests of electrical connection are performed by using the digital multimeter set up in continuity mode in order to check electrical continuity of the composite under test. When the continuity test returns negative response by the lack of emitted sound signal, the resistance reading can be subsequently performed to understand the order of magnitude of resistance related to the composite. Cases of no valid resistance reading from the multimeter imply a complete absence of conduction continuous paths inside the material since the particles are totally separate in the composite: as obvious consequence, the resistivity of composite cannot be estimated from resistance readings. Continuity tests run on samples assembled from composite with filler concentration of  $\leq 70$  wt% show complete lack of electrical connection in the material.

The first concentration value shows practical relevance in terms of electrical connection corresponds to 75 wt%. Although, composites with filler concentration of 80 wt% can be produced properly by just increasing the mixing time, the extremely enhanced density of composites with concentration  $> 80$  wt% limits the workability of the mixed material during the fabrication process.

The density of the composite depends on the density of the filler and its concentration as well. The density values of the composite, calculated by Equation 36 on page 26 for different weight concentration of filler, result

- wt = 0.70       $\phi_f = 0.182$        $\rho_C = 2.73 \text{ g cm}^{-3}$
- wt = 0.75       $\phi_f = 0.222$        $\rho_C = 3.11 \text{ g cm}^{-3}$
- wt = 0.80       $\phi_f = 0.276$        $\rho_C = 3.62 \text{ g cm}^{-3}$
- wt = 0.85       $\phi_f = 0.351$        $\rho_C = 4.33 \text{ g cm}^{-3}$

As shown by the calculated values, there is an important increase in density of the composite when the filler concentration is taken above 80 wt%. 80 wt%. For this reason, an ideal limit as workable concentration can be set at 85 wt%.

### 3.4.1 Two-point Technique

The electrical resistivity of materials is independent of the particular size or shape of the sample under test. Resistivity measurements, as known, are related to resistance measurements, which can be calculated from voltage measurements by using the two-point method.

It is called two-point since wires are connected to the material at two points of the sample and allows to calculate resistance between the two points using a voltage source draining current between them. For this purpose, two copper wires are connected to the two ends of the sample. The voltage source applies a voltage  $V$  across the sample, inducing a current  $I$  to flow through it.

The amount of current flowing through the sample is measured by an ammeter connected in series with the sample and voltage source. The internal resistance of the ammeter should be small enough to neglect the voltage drop across the instrument.

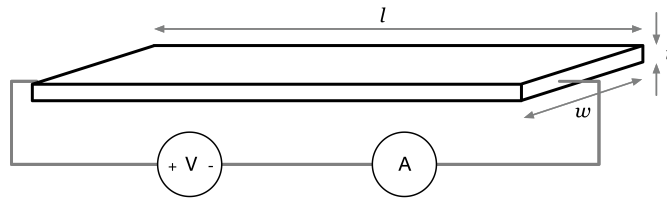


Figure 6: Two-point resistivity measurement.

The resistivity of the material can be obtained by measuring the resistance and physical dimensions of the sample. The measured resistance can be expressed as

$$R = \frac{V}{I} \quad (37)$$

Then, according to the physical dimensions of the sample, the resistivity can be determined as follows

$$\rho = R \frac{wt}{l} \quad (38)$$

where

- $\rho$  two-point resistivity ( $\Omega \text{ mm}$ )
- $R$  measured resistance ( $\Omega$ )
- $l$  sample length (mm)
- $w$  sample width (mm)
- $t$  sample thickness (mm)
- $wt$  sample cross-section area ( $\text{mm}^2$ )

It should be noted that there are issues related to the reliability of this technique due to the presence of external resistance, such as the resistance at the two points where the wires are attached on the sample (contact resistance) and the resistance of the measuring instruments as well. Therefore, the measured data as total resistance should be corrected from the external resistance values that are inevitably added up to the actual resistance value of the sample under test. These values cause an higher value of the measured resistivity which does not correspond to the actual sample resistance leading to wrong estimates of resistivity.

For the purpose of estimating resistivity from resistance measurements, Equation 38 is rewritten expressing resistance as follows

$$R = \frac{\rho}{wt} l \iff R = \frac{\rho}{wt} d \tag{39}$$

Which indicates the resistance of a conductor is directly proportional to the length of the conductor by the electrical resistivity of the material. Following the same principle, different resistance readings are performed by setting different distance between the two probes. This is equivalent to consider a different sample length for each resistance measurement. Therefore, Equation 39 is used to express resistance  $R$  as function of the distance between the probes  $d$ : the relationship between the calculated resistance values and the relative distances between the probes can provide an experimental estimate of resistivity of the fabricated composite.

Stripe-shaped samples used for electrical characterization are 50 mm long, 2 mm wide, and  $\approx 150 \mu\text{m}$  thick. The position of the probes is set by dividing the total length of the sample in intervals and moving the probes on the points related to the next smaller distance, as shown in Figure 7.

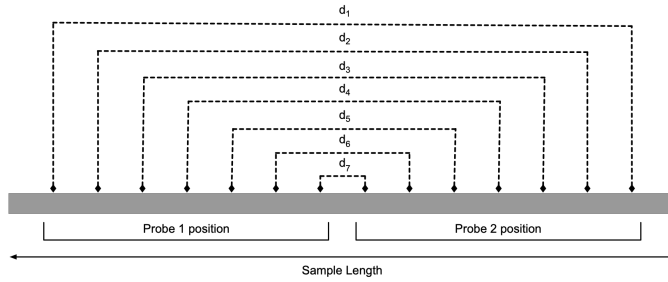


Figure 7: Schematic of the division into intervals of the sample length.

The sample length is divided into equal intervals of  $1/8''$  (3.175 mm), starting from the middle of the sample. The last positions are not considered as they are too close to the ends of the sample. The division leads to arrange the two probes in seven different positions.

The probes are supported by probe holders with signal wires with male coaxial connector for connection to measurement instruments.

For the purpose of performing resistance readings, the two inputs of a bench digital multimeter (BK Precision Model 5491B) are connected to the channel related to the used probes, as shown in Figure 8.

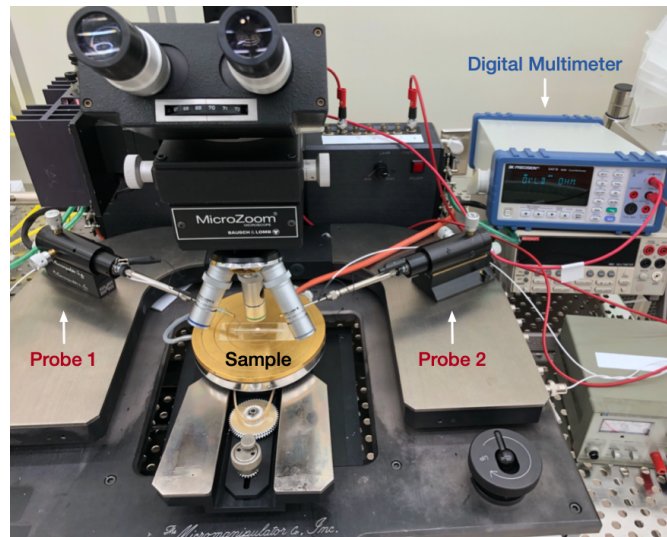


Figure 8: Micromanipulator Manual Probe Station.

The sample is placed on the plate and the vacuum is turned on in order to fix it on the plate. It avoids accidentally moving the sample during the reading process. Then, the tips are positioned properly by using the probe positioner manipulators, made stable on the probe station due to their vacuum bases. In particular, these have two manual regulators that allow to make precise up/down and right/left movements of the tips. To perform each reading, the tips are moved from the current position to the next by acting on the manipulators. After that, the tips are lowered by the height regulator until a gentle touch with the sample is achieved. An example of the tips touching the sample under test is shown in Figure 9.

Five samples are assembled from composite fabricated with filler concentration of 75 wt% and other five samples are assembled from composite with filler concentration of 80 wt%. Every sample is produced with the same geometric dimensions and then characterized in terms of resistance by using the two-point probe system in order to characterize the fabricated composites in terms of resistivity. Before starting the resistance readings, it is necessary to measure the base resistance to save the value and then subtract it from the acquired data, giving corrected resistance readings. This value takes into account the resistance of the probe system. The base resistance, measured by the direct contact of the two tips on the gold plate shows a value of  $3.84 \Omega$ . It is noted the measured resistance can be affected by the contact resistance which tends to increase the base resistance value.

This event is observed by applying pressure on the plate through the tips, leading the value to increase up to  $3.95 \Omega$ .

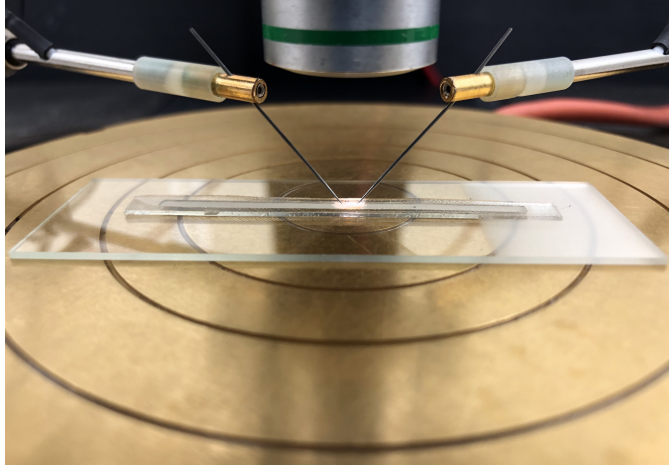


Figure 9: The tips of the two probes in gentle contact with the surface of the stripe sample under test fixed on a glass slide.

	$d_1$	$d_2$	$d_3$	$d_4$	$d_5$	$d_6$	$d_7$
	(mm)	(mm)	(mm)	(mm)	(mm)	(mm)	(mm)
	41.275	34.925	28.575	22.225	15.875	9.525	3.175
75 wt%							
$R_1 (\Omega)$	3.72	2.83	2.30	2.12	1.52	1.25	0.87
$R_2 (\Omega)$	3.81	2.36	1.90	1.55	1.36	1.23	0.49
$R_3 (\Omega)$	3.30	2.60	2.18	2.03	1.67	0.99	0.54
$R_4 (\Omega)$	3.61	3.08	2.70	2.04	1.59	1.11	0.57
$R_5 (\Omega)$	3.65	2.18	1.87	1.67	1.45	0.94	0.78
80 wt%							
$R_1 (\Omega)$	1.60	1.41	1.20	1.14	0.85	0.69	0.40
$R_2 (\Omega)$	1.46	1.27	1.06	0.98	0.81	0.54	0.39
$R_3 (\Omega)$	1.66	1.54	1.21	1.01	0.77	0.69	0.44
$R_4 (\Omega)$	1.61	1.39	1.11	0.84	0.65	0.46	0.31
$R_5 (\Omega)$	1.53	1.38	1.23	1.14	0.72	0.64	0.52

Table 1: Experimental resistance values.

The performed data collection based on resistance readings, reported in Table 1, is then processed by linear regression model. Hence, according to the linear equation in the form  $y = mx + b$ , where

$$y = R \quad x = d \quad (40a)$$

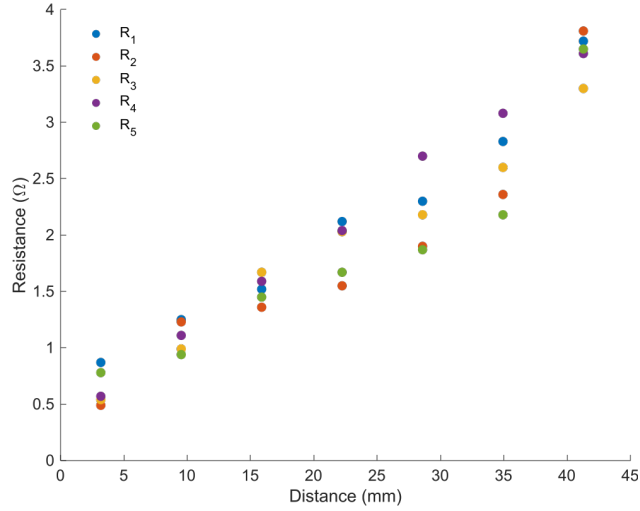
$$m = \rho / (wt) \quad b = 0 \quad (40b)$$

The resistivity of the composite can be then estimated from the experimental slope value  $m$ , considering a sample cross-section area  $\approx 0.3 \text{ mm}^2$  ( $w = 2 \text{ mm}$ ,  $t = 0.15 \text{ mm}$ )

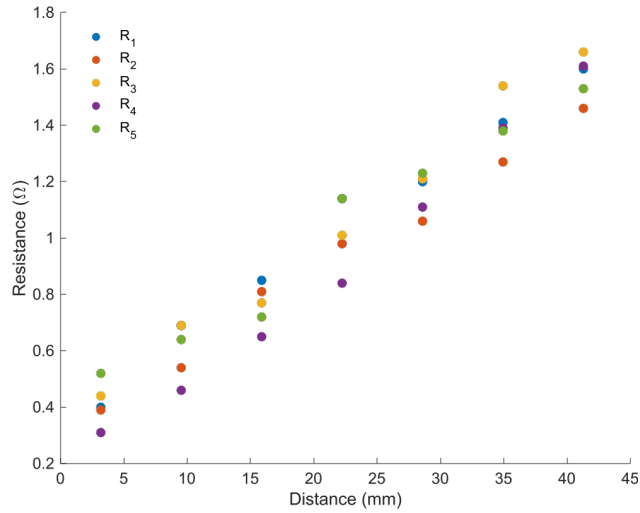
$$\rho = m w t \quad (41)$$

As a final step, electrical conductivity is easily obtained by taking the inverse of the estimated resistivity

$$\sigma = \rho^{-1} \quad (42)$$

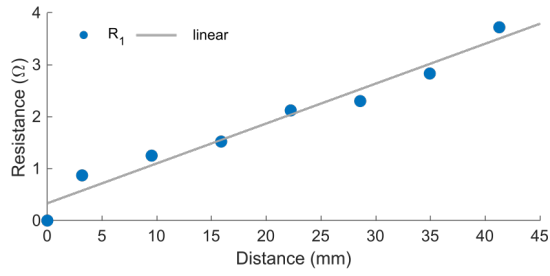


(a)

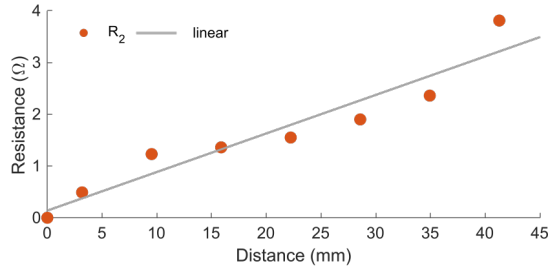


(b)

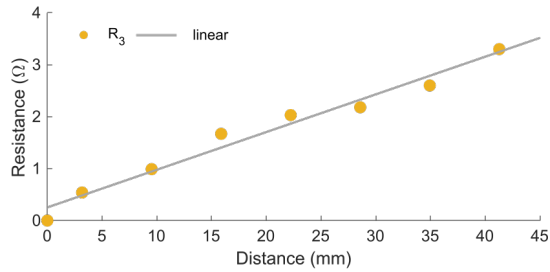
Figure 10: Global scatter plot of the resistance measurements related to the 75 wt% samples (a) and the 80 wt% samples (b).



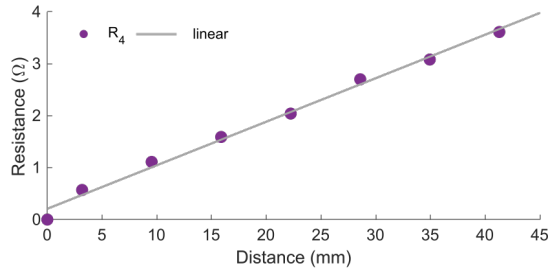
(a) sample 1.



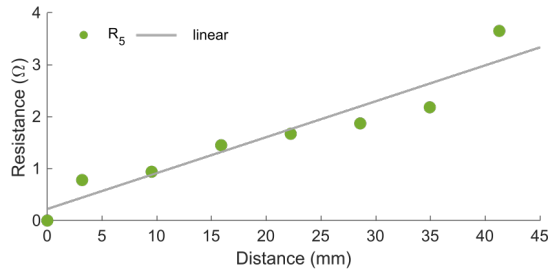
(b) sample 2.



(c) sample 3.

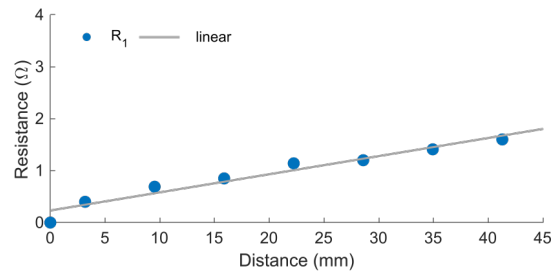


(d) sample 4.

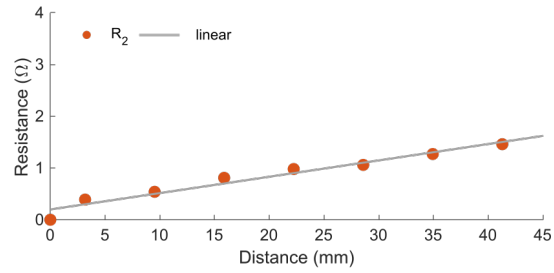


(e) sample 5.

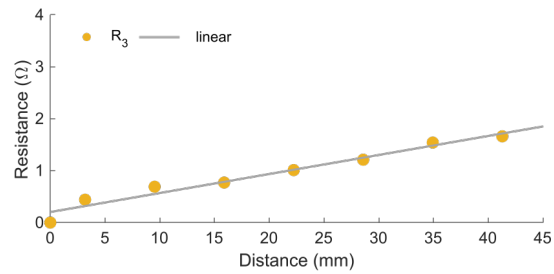
Figure 11: Linear fitting of resistance readings related to 75 wt% samples.



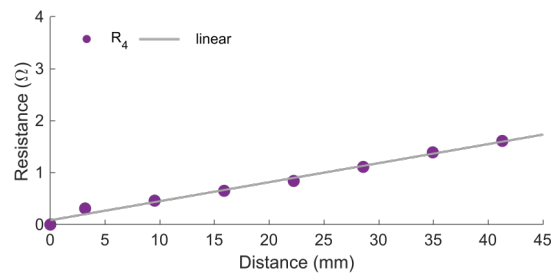
(a) sample 1.



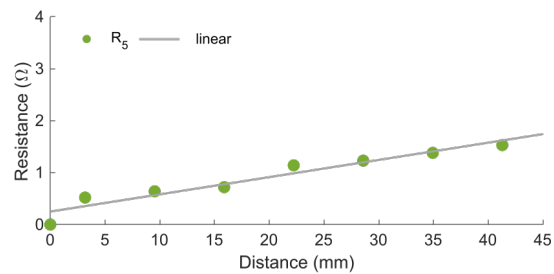
(b) sample 2.



(c) sample 3.



(d) sample 4.



(e) sample 5.

Figure 12: Linear fitting of resistance readings related to 80 wt% samples.

Table 2 summarizes the experimental parameters calculated from the characterized samples.

sample	$R^2$	$m$ ( $\Omega \text{ mm}^{-1}$ )	$b$ ( $\Omega$ )	$\rho$ ( $\text{m}\Omega \text{ cm}$ )	$\sigma$ ( $\text{S cm}^{-1}$ )
75 wt%					
s <sub>1</sub>	0.9612	0.0768	0.3328	2.30	434
s <sub>2</sub>	0.9083	0.0745	0.1388	2.23	447
s <sub>3</sub>	0.9732	0.0725	0.2532	2.18	460
s <sub>4</sub>	0.9925	0.0838	0.2080	2.51	398
s <sub>5</sub>	0.8990	0.0691	0.2232	2.07	482
80 wt%					
s <sub>1</sub>	0.9490	0.0349	0.2327	1.05	955
s <sub>2</sub>	0.9557	0.0316	0.1993	0.95	1055
s <sub>3</sub>	0.9618	0.0366	0.2029	1.10	910
s <sub>4</sub>	0.9883	0.0366	0.0838	1.10	910
s <sub>5</sub>	0.9289	0.0332	0.2502	0.99	1005

Table 2: Calculated experimental parameter.

Once the data fit is executed, the resistivity values are calculated by slope of the linear functions so that the estimate of conductivity is accomplished. Finally, the experimental results related to the considered concentration values are analyzed in terms of the first two statistical moments, i. e. mean value and standard deviation, to quantify the variation level of the estimated conductivity. The statistical values are reported in Table 3.

	75 wt% ( $\text{S cm}^{-1}$ )	80 wt% ( $\text{S cm}^{-1}$ )
max	482.2	1055
min	397.8	909.9
$\mu$	444.2	967.2
$\sqrt{\sigma^2}$	31.4	62.9
$\mu + \sigma$	475.6	1030.1
$\mu - \sigma$	412.8	904.3
range	84.4	145.1

Table 3: Statistical data of conductivity values.

## 3.5 PERCOLATION ANALYSIS

From the performed electrical characterization of the composite, the study of percolation is conducted in order to estimate the value of critical volume fraction according to the adopted model.

Since Equation 14 on page 22 explaining percolation theory contains filler concentration expressed in volume, it is necessary to convert the weight concentration in volume concentration. The conversion can be done by using Equation 27 on page 25. Figure 13 reports the calculated curve expressing the relationship between the two types of concentration.

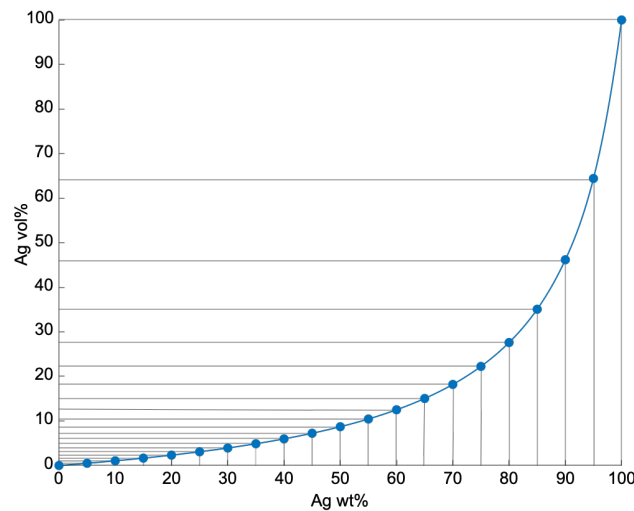


Figure 13: Ag weight-volume concentration relationship curve.

With reference to the experimental data, high conductivity values are found for weight concentration of 75 wt%, with a mean value higher than  $4 \times 10^2 \text{ S cm}^{-1}$ . This indicates the percolation threshold should lie for concentration values lower than this concentration value. Since no electrical connection is observed in the cases tested with 70 wt%, it can be concluded the sharp increase in conductivity of composite occurs for a concentration value between 70 wt% and 75 wt%.

By changing the concentration value from 75 wt% to 80 wt%, the calculated conductivity increases moderately keeping the same order of magnitude ( $10^2$ ) until the maximum value of  $\approx 967 \pm 63 \text{ S cm}^{-1}$  is reached. This should mean the value increases with increasing filler concentration, but the significant change in the electrical property of the material occurs before the 75–80 wt% range.

Conductivity values calculated for concentration values higher than 80 wt% are expected to be higher than the maximum experimental value found at 80 wt% ( $\approx 1030 \text{ S cm}^{-1}$ ), while maintaining the same order of magnitude ( $10^3$ ). According to statistical data reported in Table 3, a percolation curve, relative to the concentration range analyzed for the experimental acquisition, is plotted.

Hence, the plot in Figure 14 shows the conductivity values as a function of the filler concentration, reported by the double x-axis of the weight and volume concentration.

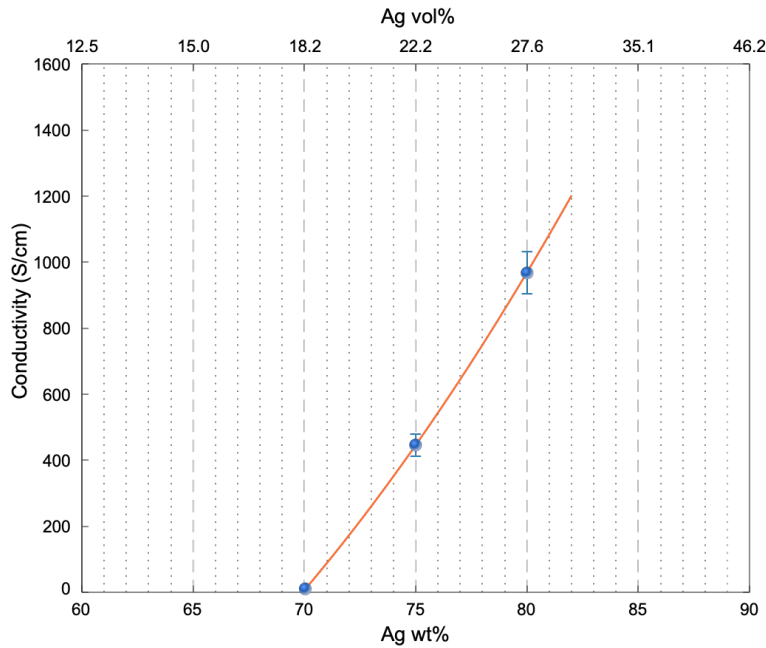


Figure 14: Concentration-conductivity curve.

The goal is to establish the critical concentration at which a conduction path is formed in the composite material turning the insulator material to a conductor. Estimating a percolation threshold in terms of weight concentration between 70 wt% and 75 wt% corresponds to consider a volume concentration higher than  $\approx 18\%$  and lower than  $\approx 22\%$ .

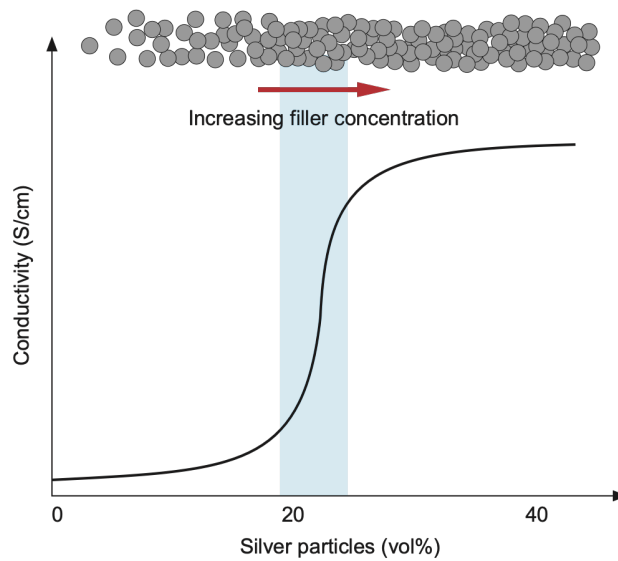


Figure 15: Schematic of estimated percolation threshold.

As evident from the curve shown in Figure 14, the conductivity for volume concentration  $> 27\%$  increases by 2 orders of magnitude from the values related to the established percolation volume. This behavior could be indicative of the achieved percolation transition.

It is important to get an idea of the percolation threshold of composites, as it can be extremely useful for choosing the amount of filler in the fabrication process of conductive composites. In particular, in strategies for developing conductive structures, such as in the case of sensing devices, the price of the conductive material is generally much higher than the non-conductive material that acts as support part. This matches with the analyzed case, indeed the silver powder is obviously more expensive than the polymer matrix itself.

The following description gives an example of a possible estimate. The first step to fit the experimental results is to assume an appropriate value for  $\phi_c$ . Based on the curve in Figure 14,  $\phi_c \approx 18 \text{ vol}\%$  is assumed for this example. Then the volume differences  $\phi_i - \phi_c$  are calculated, considering the only volume concentrations above the critical volume

- wt = 0.73       $\phi_1 - \phi_c = 0.205 - 0.182 = 0.023$
- wt = 0.75       $\phi_2 - \phi_c = 0.222 - 0.182 = 0.04$
- wt = 0.80       $\phi_3 - \phi_c = 0.276 - 0.182 = 0.094$

The data are then used to plot the graph of conductivity  $\sigma$  versus  $\phi_i - \phi_c$ , as shown in Figure 16.

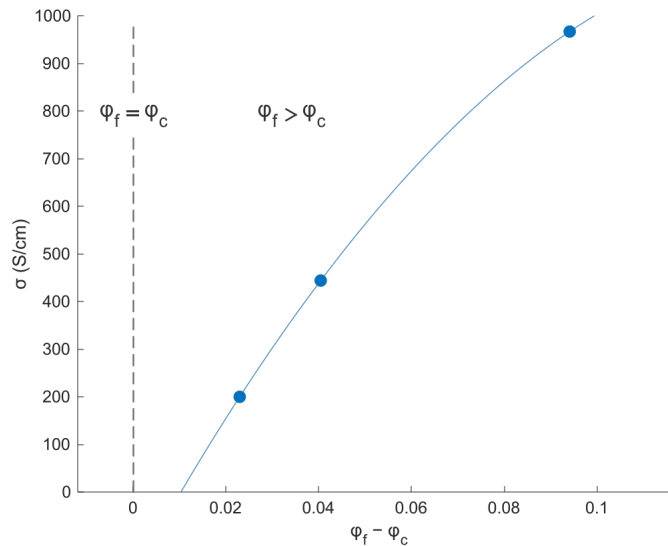


Figure 16: Example of percolation curve.

According to the graph, the fixed percolation threshold is indicated by the dotted line which separates the region of validity of the adopted equation ( $\phi_f > \phi_c$ ). Also, to obtain a linear fashion of data, the logarithmic scale is used on both axes, as shown in Figure 17.

This allows to calculate the critical exponent  $t$  from the linear fit, as described in Section 3.2 by Equation 19 on page 23.

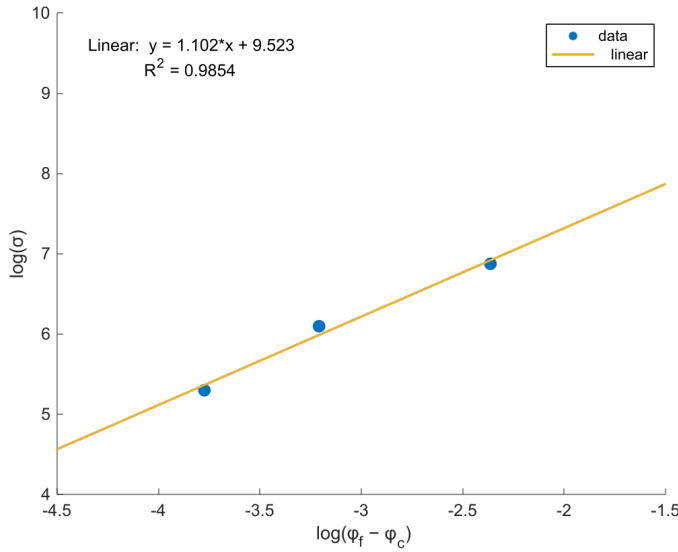


Figure 17: Linear fitting of the curve in logarithmic scale.

The best fit obtained results in value 1.1 of the critical exponent. The accuracy of fitting is indicated by the value of  $R^2 = 0.985$ .

The experimental power-law equation then becomes

$$\sigma = \sigma_0 (\phi_f - 0.182)^{1.1} \quad (43)$$

where

$\sigma$ ( $\text{S cm}^{-1}$ )	composite conductivity
$\sigma_0 = 6.29 \times 10^5 \text{ S cm}^{-1}$	silver conductivity
$\phi_c = 0.182$	critical volume fraction
$\phi_f$	volume fraction of filler
$t = 1.1$	critical exponent

The value of the critical exponent  $t$  strictly depends on the type of filler. The found value falls within the range reported by different authors, ranging from values below 1 such as 0.7–0.9 up to values around 3. It should be noted that the calculated value depends on the model used to explain the percolation theory as well as on the analyzed filler concentration range.

## 3.6 SEM ANALYSIS

Cross-sectional scanning electron microscopy (SEM) images of the fabricated samples are used to analyze the morphology and chemical elements in the composite. Moreover, these can reveal how the dispersed phase of conductive particles appear into the continuous polymeric phase when the fabrication process of the composite is completed.

SEM bases the operating principle on the detection of high energy electrons emitted from the analyzed samples' surface after being exposed to a highly focused beam of electrons from an electron gun. The preliminary requirement to follow for the samples preparation is based on the use of a thin film deposition system. The ion beam sputtering system, as that shown in Figure 18, is used to precisely deposit thin conductive coatings onto samples' surface prior to examination in the electron microscope.



Figure 18: Ion Beam Sputtering System.

Thin conductive films are deposited onto samples to prevent charging effects and to enhance contrast in images as well. Once the samples are introduced into the high vacuum chamber of the system, after the vacuum and the ion beam current set-up, the system provides the charge to the samples while spinning the rotating substrate holder where those are placed. After the sputtering process, the prepared samples are properly fixed onto the specimen holder and can be loaded in the SEM to be analyzed. The used electron microscope is shown in Figure 19.

The detector is set up with a typical ETH (electron high tension) of 5 kV and images are captured by a scan speed of 10, reduced up to 5 in cases of highly zoomed images to obtain a better acquisition. In addition to images acquired by using the detector for general purpose imaging, labeled as SE2, images are also captured by using the back scatter signal of the back-scatter electron detector, labeled as QBSD, that is very suitable for high contrast imaging.

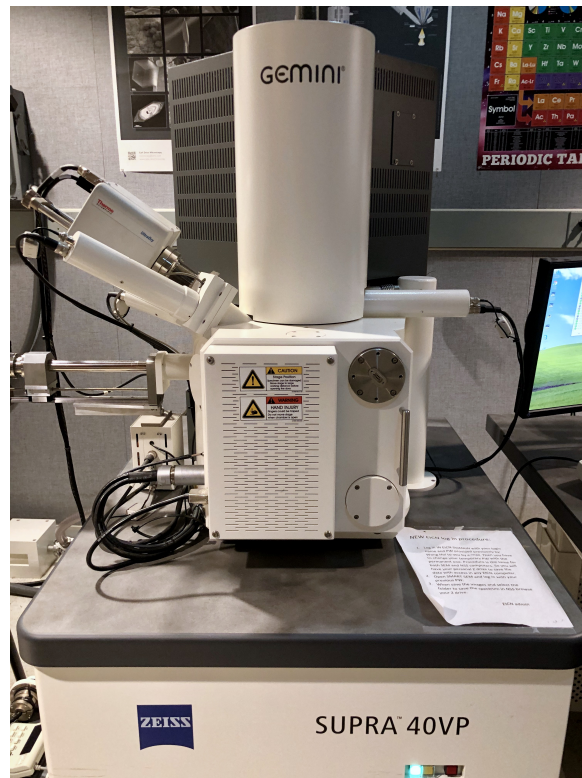
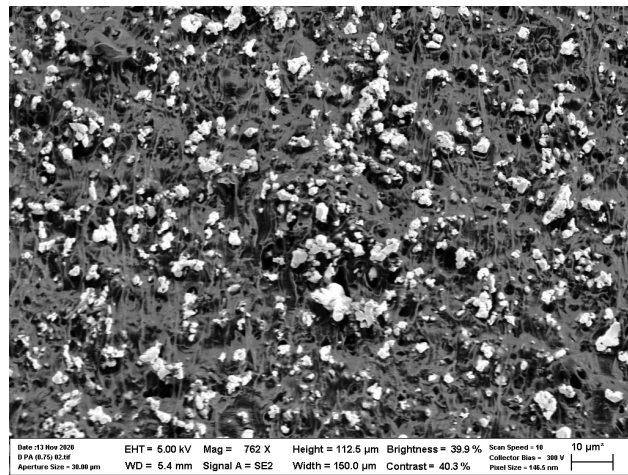


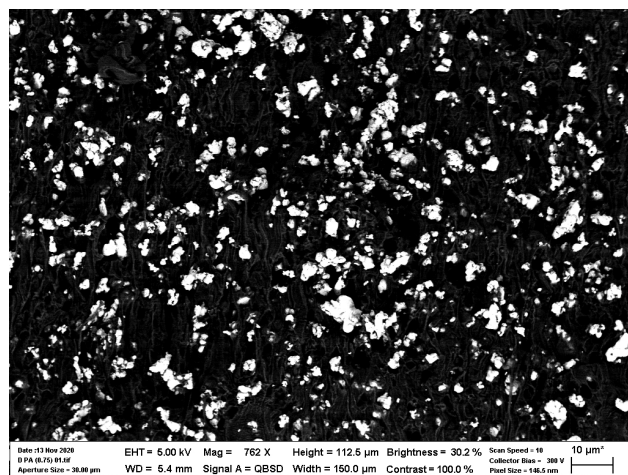
Figure 19: ZEISS Scanning Electron Microscope.

These images are formed by reflected electrons which are emitted by elastic scattering of the incident electrons. A back-scattered image reveals the compositional difference of the sample, according to the difference in the average atomic number. Since elements with high atomic number, such as Ag in this application, reflect electrons more strongly than elements with low atomic number, these appear brighter in the image. It means this kind of images are very suitable to highlight contrast due to the different chemical compositions.

The acquired SEM images, are related to cross sections of the Ag-PDMS samples with a silver content of 75 wt% and 80 wt%. Increasing the Ag content above 70 wt% results in complete coverage of the entire cross-sectional area, implying that the Ag particles are fully connected in the PDMS matrix. It is noted that the obtained dispersion level of the silver particles is significantly influenced by the mixing step during the fabrication process. The images show that all silver particles are uniformly distributed in the form of 3D network, meaning to suggest that the percolation network is completely created between the conductive particles, according to the continuity test performed during the electrical characterization of composites.



(a) SE2 image.

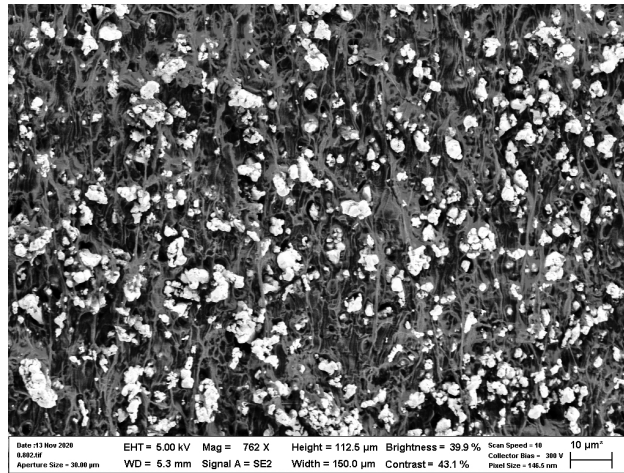


(b) QBSD image.

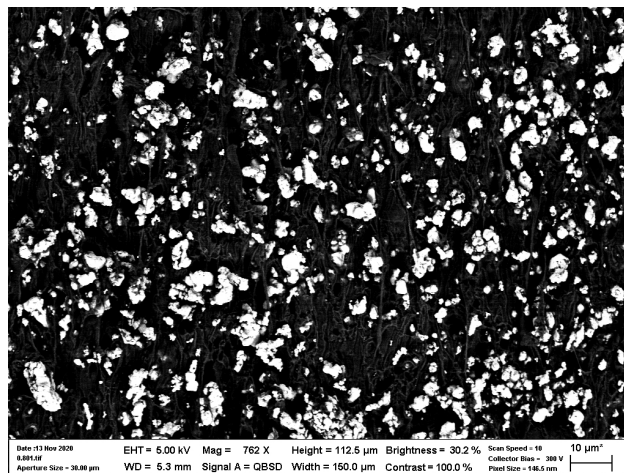
Figure 20: Cross-sectional view of sample with Ag concentration of 75 wt%.

The images in Figure 20 show the cross-sectional view of the sample produced with a filler concentration of 75 wt%. It is interesting to report both image versions, indeed the first image (a) can give idea of the background made of polymer, whereas the second one (b) focuses on the particles embedded between the polymer fibers.

In details, the first type of image highlights the morphology of both the composite phases, showing with high definition the polymer matrix in dark gray color and the bright silver particles dispersed inside that. In particular, the color of the particles results lighter than the background due to the different chemical composition between the metal particles and the polymer. The back-scattered image shows extremely bright silver particles in standing out on the dark background due to the enhanced contrast given by the electron reflections, allowing to easily observe the distribution of the particles within the polymer matrix.



(a) SE2 image.



(b) QBSD image.

Figure 21: Cross-sectional view of sample with Ag concentration of 80 wt%.

The same acquisition is then repeated for the sample produced with a filler concentration of 80 wt%, as shown in Figure 21. According to the increasing of filler concentration, the images of samples with different filler concentration show an improved quantity of silver clusters. This relevant feature is further analyzed by the image processing of the acquired images based on particle analysis. For a reasonable comparison of the two sectional images, the acquisitions are made with the same values of 150  $\mu\text{m}$  and 10  $\mu\text{m}$ , as reference to the width of the image and the scale, respectively.

The particle analysis can be executed by uploading the captured images on the dedicated ZEISS Software. Figure 22 on the next page shows two examples of cross-sectional images used for the purpose of particle analysis.

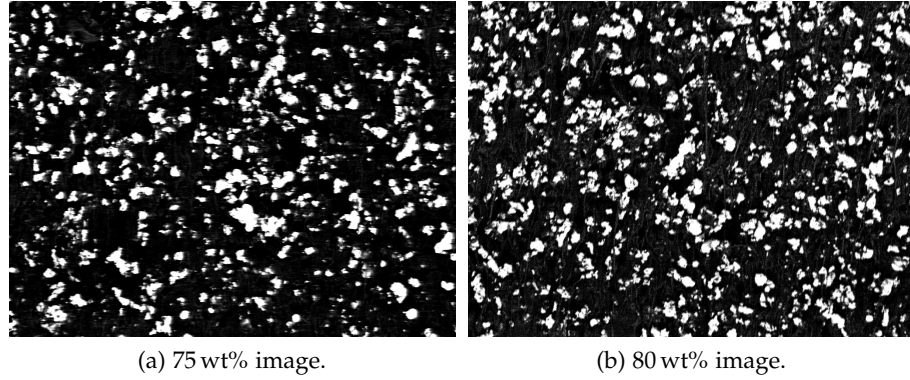


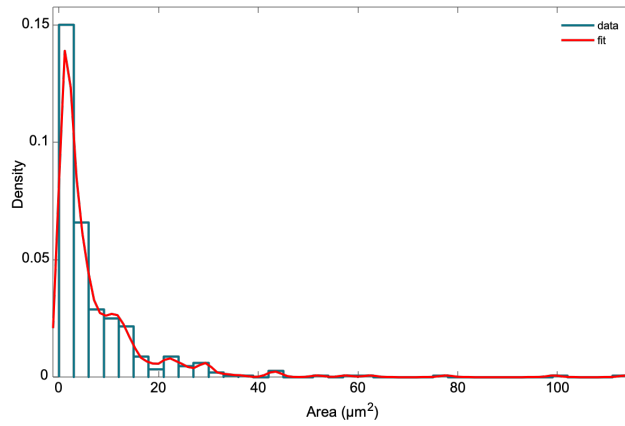
Figure 22: Cross-sectional images for particle analysis.

The Software can detect a total number of particles producing results for each uploaded image. The output data includes values of different parameters related to each particle. In particular, the following particle parameters are provided as output of the performed particle analysis:

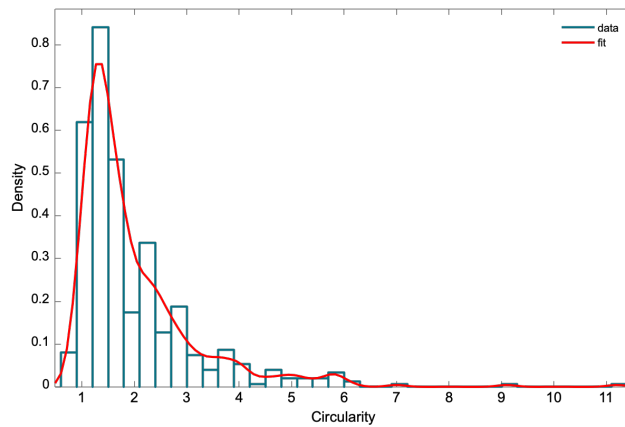
- Particle #
- Area
- Perimeter
- Circularity
- Coordinate x of centroid, Coordinate y of centroid
- Min coordinate x, Max coordinate x
- Min coordinate y, Max coordinate y
- Length, Width
- Aspect Ratio

Image Reference	75 wt%	80 wt%
Total Particles	495	593
Frac Area (nm <sup>2</sup> )	0.193 789	0.235 961
Total Area (nm <sup>2</sup> )	$1.92 \times 10^{10}$	$1.92 \times 10^{10}$
Image X Res (pixels)	1024	1024
Image Y Res (pixels)	768	768
Pixel Size (nm)	156.25	156.25

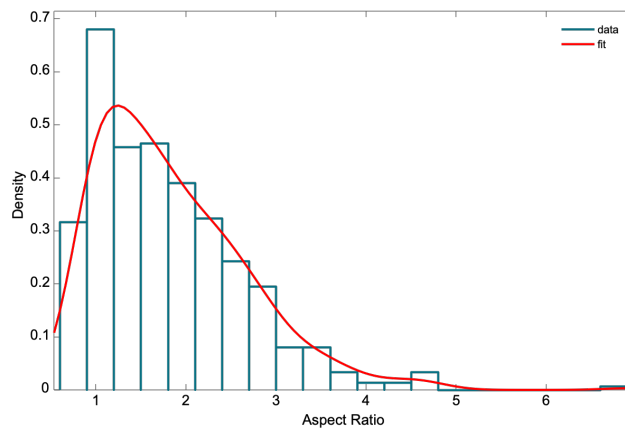
Table 4: Particle results of the analyzed images by the Software.



(a)



(b)

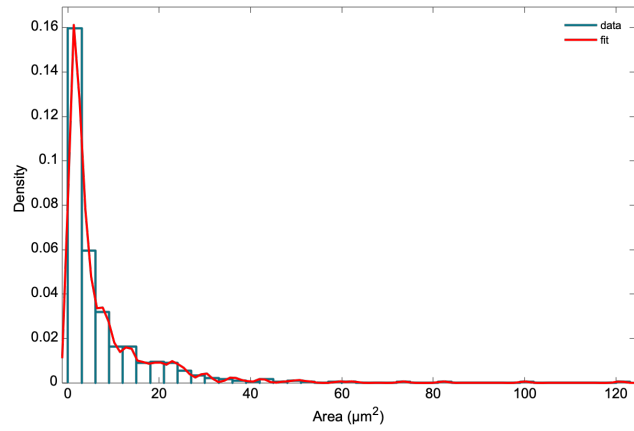


(c)

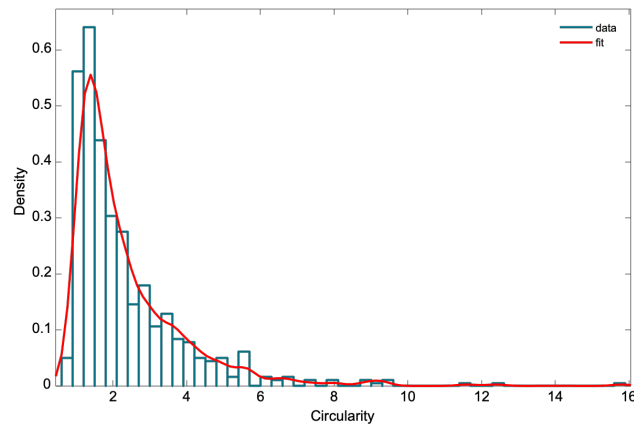
Figure 23: Distribution of Area (a), Circularity (b), and Aspect Ratio (c), for the 75 wt% processed image.

Although the particle analysis by the Software allows to estimate the particle contents, it is important to distinguish single particles from aggregated particles leading to form big clusters by aggregation of more single particles.

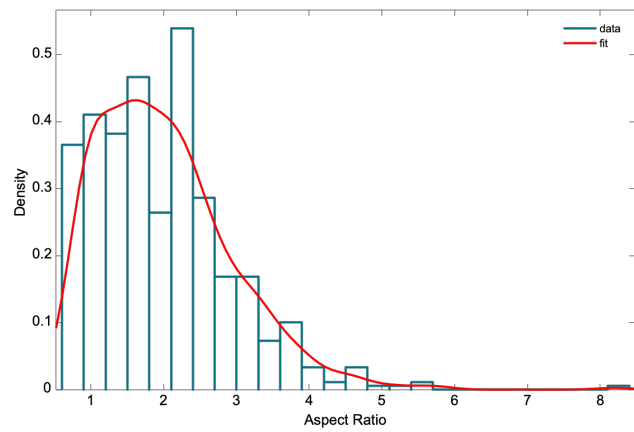
For this reason, some parameters related to both images are observed by distribution plots in order to understand their range of values, as shown in Figure 23 and Figure 24.



(a)



(b)



(c)

Figure 24: Distribution of Area (a), Circularity (b), and Aspect Ratio (c), for the 80 wt% processed image.

The distributions of area suggest the most particles have an area under a certain value, whereas higher values correspond to multiple particles grouped together. Moreover, the circularity index and the aspect ratio are parameters indicative of the cluster shape factor. The aspect ratio is a function of the largest and the smallest diameters that are orthogonal to each other: according to the ratio between the maximum axis and the minimum axis, the parameter tends to unity for particles with axes of approximately the same dimensions, while becomes larger when the maximum axis gets bigger and bigger than the minimum one.

The circularity depends on the square perimeter and the area, varying from 1 for a circle to higher values for cases with lacking circularity. For this reason, extremely large values of circularity indicate the presence of clusters in the network. Considering only this parameter may not be significant enough to detect clusters, due to the probability to find clusters with approximately round shape, which minimize the related circularity index.

In order to locate the formed clusters, the areas with large values must be considered. Based on the diameter range of 2–3.5  $\mu\text{m}$  and assuming particles are perfectly spherical, i. e. aspect ratio and circularity equal to 1, the area values are in the range  $\approx 3\text{--}10 \mu\text{m}^2$ . Even though these strong suppositions, the distributions of area show the highest density of particles for area values  $< 10 \mu\text{m}^2$ . Therefore, higher values are related to clusters with different size, which can be characterized by increasing values of aspect ratio and circularity as well.

In addition to the analysis performed by the Software providing output data automatically, some step of image processing are executed using the Image Processing Toolbox on MATLAB<sup>®</sup>. The aim is to run image segmentation in order to quantify the detected particles in images. Moreover, estimating the number of clusters by analyzing the area of the segmented regions can be very relevant.

The original images are gray-scale images, so these can be transformed in binary images by thresholding. For this purpose, `imbinarize` function creates a binary image from gray-scale image by replacing all values above a globally determined threshold with 1 and setting all other values to 0. This function works calculating the global image threshold by automatic method.

---

```
1 BW = imbinarize(I);
```

---

The white regions of the binary images can be easily highlighted by tracing their boundaries by the `bwboundaries` function, that allows to trace region boundaries in binary images, as shown in Figure 25 and Figure 27.

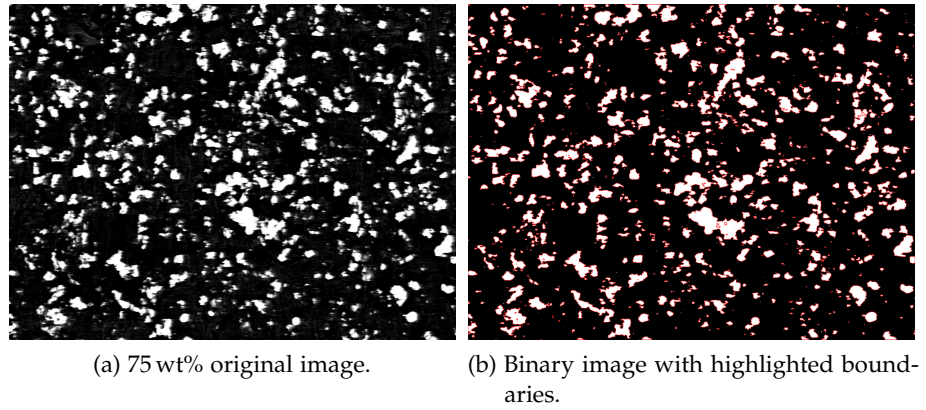


Figure 25: The logical image (b), related to the original one (a), is created to be processed for the clusters detection.

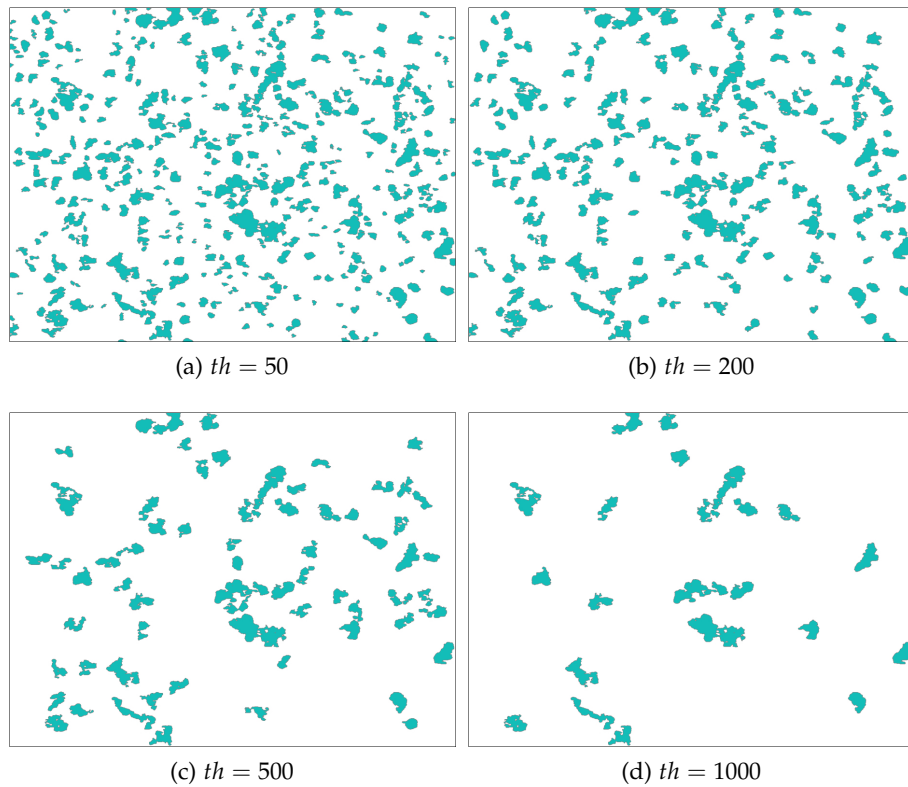


Figure 26: Clusters identification of the 75 wt% processed image by setting increasing area thresholds.

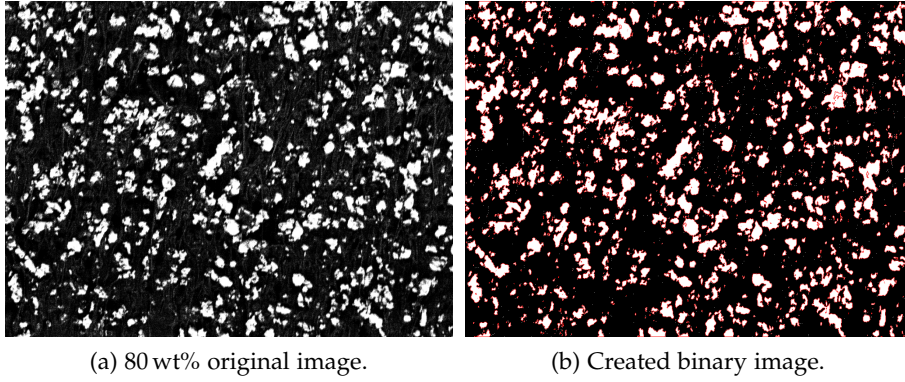


Figure 27: The logical image (b), related to the original one (a), is created to be processed for the clusters detection.

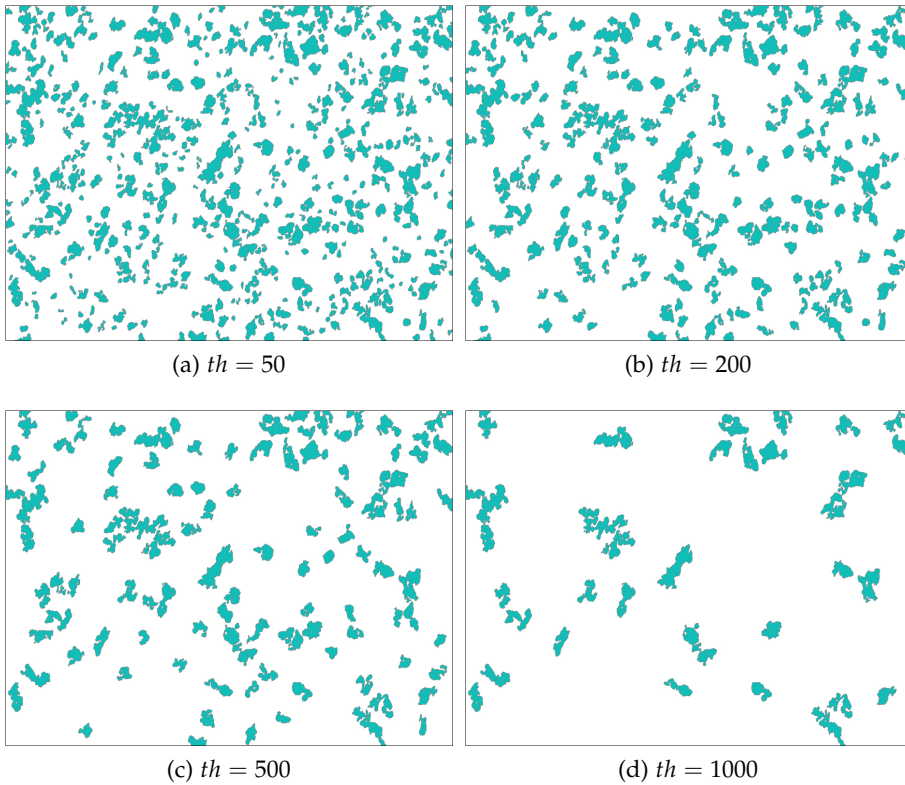


Figure 28: Clusters identification of the 80 wt% processed image by setting increasing area thresholds.

The function `bwconncomp` returns the connected components found in the binary image `BW`. It can compute connected components for binary images using a two-dimensional pixel connectivity of 8: pixels are connected if their edges or corners touch, two neighboring pixels belong to the same object if they are both on and are connected along the horizontal, vertical, or diagonal direction.

---

```
CC = bwconncomp(BW);
```

---

The relevant output data returned by the function are

`NumObjects`    Number of connected components (objects) in `BW`  
`PixelIdxList`   Cell array containing the pixel indices of each object

The `regionprops` function allows to measure a set of properties for each 8-connected component found by `bwconncomp`. Therefore, the area is calculated for connected components in the images using this function, which returns the values in a structure array.

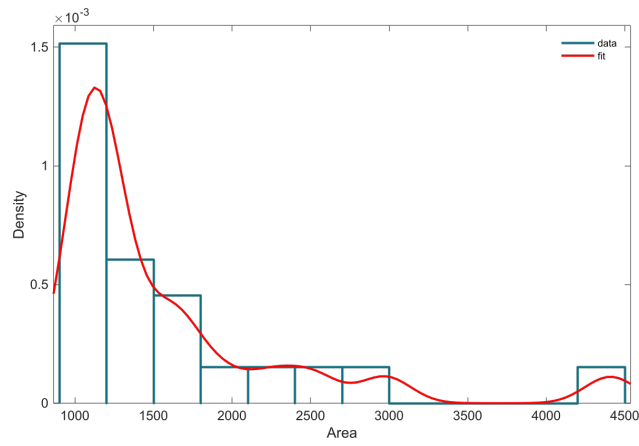
---

```
s = regionprops(CC, 'area'); %struct array
s = struct2cell(s);
area = cell2mat(s); %area values saved in a double array
```

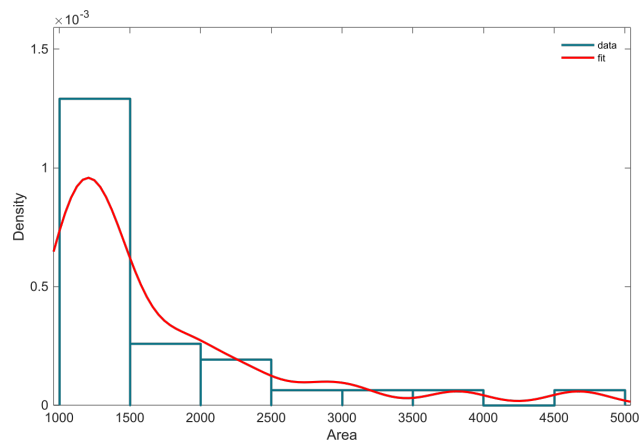
---

Observing the distribution of the calculated area values, it is possible to set some values as threshold in order to isolate only objects with higher area. This goal is achieved by setting 1 to the pixel indices of the binary image corresponding to the calculated indices of connected components with area above the set-up threshold, and setting all other values to 0. This allows to identify particles with big sizes, which means to detect the clusters formed in the percolated network. For this purpose, increasing threshold values are tested and the related results are displayed in Figure 26 and Figure 28.

The clusters with the biggest sizes, formed by aggregation of a large number single particles, can be identified by setting a threshold in terms of area values after inspection of the area distribution. Examples of area distributions for the found connected objects with area values higher than 1000 are reported by schematics in Figure 29, whereas a global representation of values for both images is provided by plot in Figure 30.



(a)



(b)

Figure 29: Distribution of cluster area for  $th = 1000$ , related to the 75 wt% image (a) and the 80 wt% image (b).

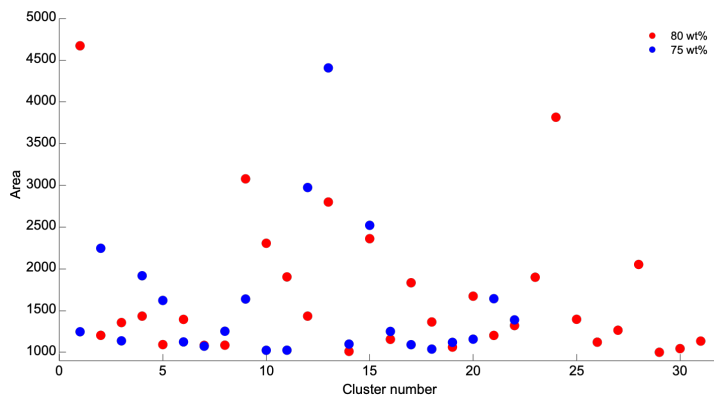


Figure 30: Scatter plot of clusters with area values  $> 1000$ .

From the conducted analysis on the size of clusters, the formation of a 3D conductive network within the insulating material can be entirely confirmed.

The increase in the filler concentration, as demonstrated by passing from 75 wt% to 80 wt%, induces to have a larger number of separated particles which indicates a high probability to find continuous paths between the bigger aggregations, letting electrons flow through.

	75 wt%	80 wt%
Detected Clusters	22	31
Min Area	1025	1001
Max Area	4408	4673

Table 5: Detected clusters by setting an area threshold of 1000.

Cross-sectional images of the sandwich structured sample allow to distinguish the area interface between the two different materials, i. e. the conductive composite and the PDMS. The sample used for the acquisitions consists of a bottom layer made of pure PDMS and a conductive layer of Ag-PMDS composite, as shown in Figure 31.

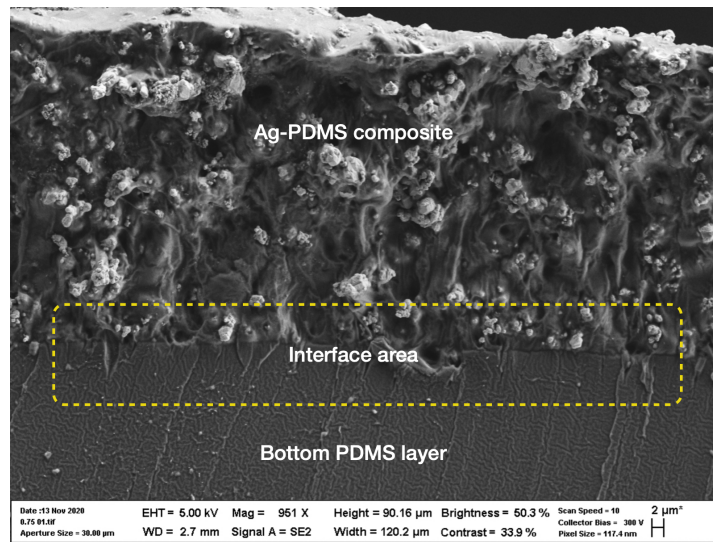


Figure 31: Cross-sectional SEM image of the sample shows clearly the interface between the materials.

The two layers are produced in separate fabrication steps and then assembled together. In particular, after the bottom layer becomes solid by curing process, the conductive paste is poured onto that. Then, during the polymerization time of the composite, it creates bonds also on the interface area with the bottom PDMS layer. It means the two final layers exhibit great match due to the same material they are made of.

Indeed, since the composite is based on the same polymer as the support layer, it leads to a compact multilayer structure reducing the risk of delamination under increasing stress conditions.

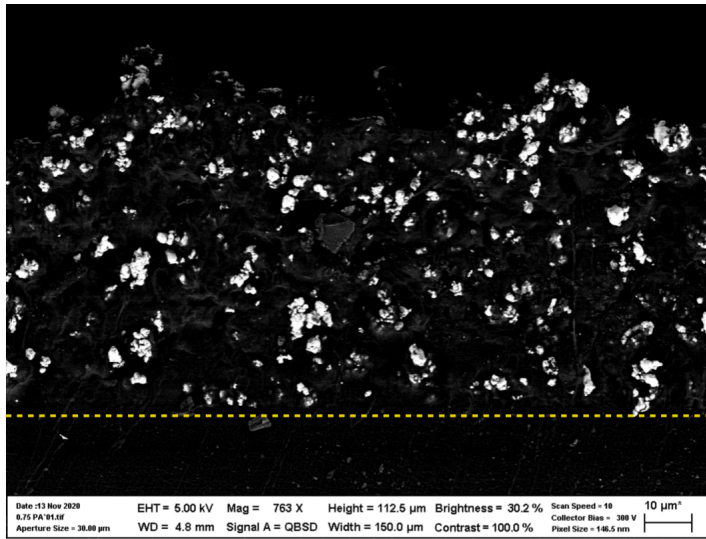


Figure 32: Back-scattered cross-sectional image with marked dividing line.

The particles are present only in the top layer, as shown by the back-scattered image in Figure 32. Moreover, the lower brightness image reported in Figure 33 shows the separation between the layers and allows to notice the final appearance of the polymerized pure PDMS as well. The different texture of the two layers is due to presence of two phases in the formed composite.

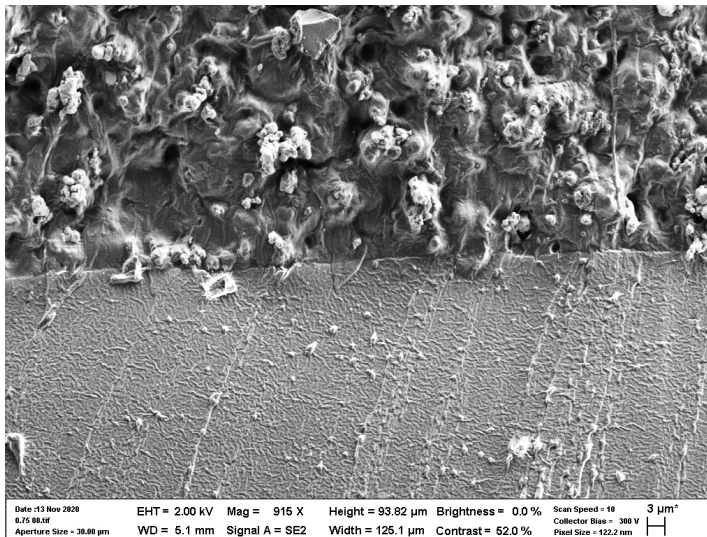
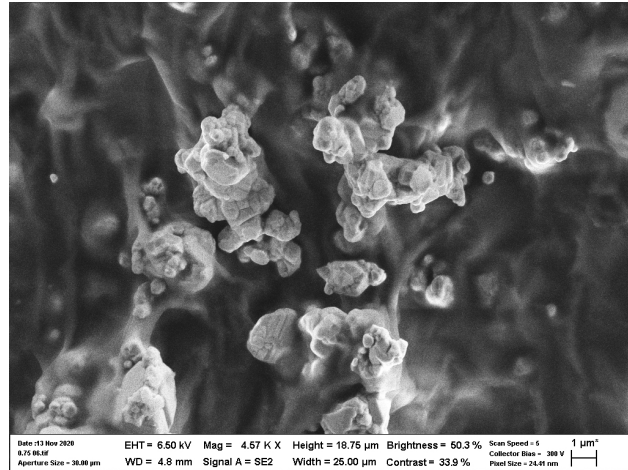
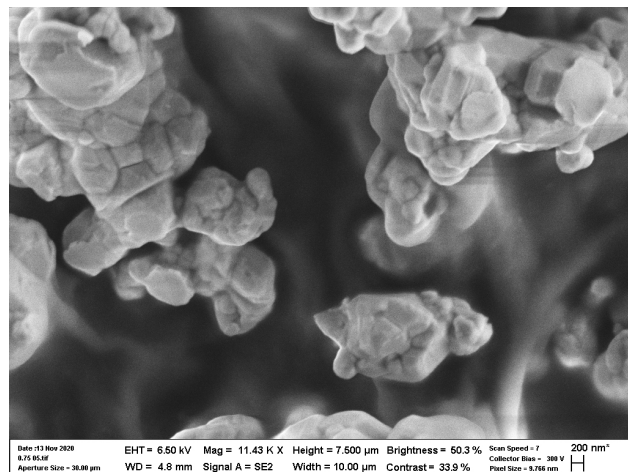


Figure 33: Cross-sectional image highlights the different appearance of the two materials.

The polymer chains link among the microparticles which result completely embedded in the final solid material. For this reason, the mixing step of fabrication influences the final aspect of the produced composite, as it is strictly related to the level of integration of particles within the polymer matrix. The appearance of the dispersed silver particles can be observed more closely in Figure 33 by different levels of magnification.



(a) SEM image (width=25  $\mu\text{m}$ , scale=1  $\mu\text{m}$ ).

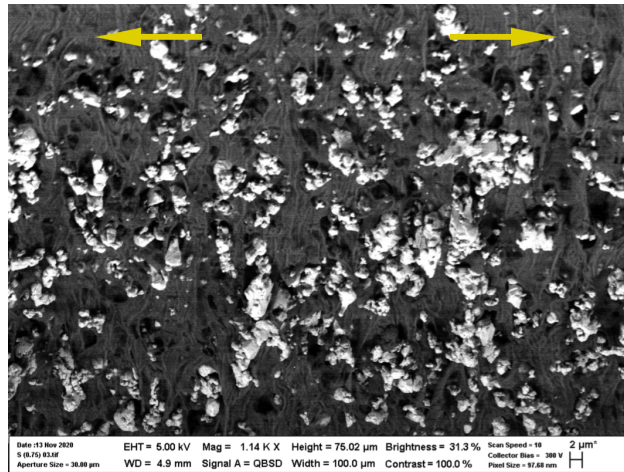


(b) SEM image (width=10  $\mu\text{m}$ , scale=200 nm).

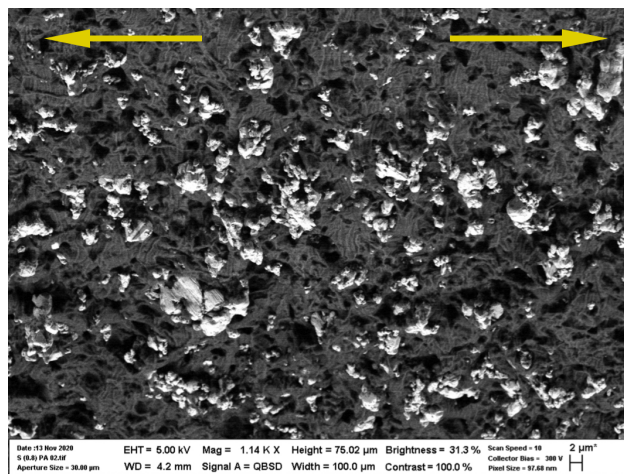
Figure 34: Detail of the Ag particles with low (a) and high (b) magnification.

A further acquisition is performed keeping sample stretched in two different levels of strength. The comparison of the two images reported in Figure 35 shows the deformation of the material while withstanding the applied elongation. Formation of holes between due to the movements of the particles can be observed by the presence of black regions in the polymer matrix. The stress condition leads to distance the particles from the no-stress positions inducing a complete deformation of the conductive network.

Since the maximum strain occurs along the longitudinal axis, most of the particles tend to move along the longitudinal direction. For this reason, longitudinal sections of samples are used to perform this last image acquisitions.



(a) First strain state.



(b) Second strain state.

Figure 35: SEM images of samples under states of increasing deformation.

When samples are stretched, the distance between adjacent silver particles increased gradually along the tensile direction. It makes the particles no longer tightly connected so that the conductive pathways reduce consequently. This event explains why the resistance of the composite increases after stretching.



## CHAPTER FOUR

## 4.1 DEFORMATION DEPENDENCE

Piezoresistive strain sensors base their working principle on the relative resistance change following the applied strain. Therefore, it may be important to understand how the resistance change is related to strain. For this purpose, the derivation of the theoretical electrical resistance change for stretchable strain sensors is described.

According to equation

$$R = \rho \frac{l}{w t} \quad (44)$$

where

- $R$  sensor resistance ( $\Omega$ )
- $l$  sensor length (mm)
- $w$  sensor width (mm)
- $t$  sensor thickness (mm)
- $w t$  sensor cross-section area ( $\text{mm}^2$ )
- $\rho$  electrical resistivity of the conductive material ( $\Omega \text{ mm}$ )

Assuming that the geometric deformation causes most of the change due to the applied strain, the change in resistivity can be neglected. Hence, resistance before and after the stretching state result

$$\begin{aligned} R_0 &= \rho \frac{l_0}{w_0 t_0} \\ R &= \rho \frac{l}{w t} \end{aligned} \quad (45)$$

where the physical quantities marked with the subscript “0” refer to initial condition of absence of applied strain. Assuming sensors made of incompressible materials, volume does not change after stretching

$$V = V_0 \implies l w t = l_0 w_0 t_0 \quad (46)$$

By rewriting the expression of resistance after stretching

$$R = \rho \frac{l^2}{l_0 w_0 t_0} \quad (47)$$

indicating that the electrical resistance changes in relation to the square of sensor length.

Then, the resistance can be related to the initial resistance value by expressing the relative resistance change

$$\frac{\Delta R}{R_0} = \frac{R}{R_0} - 1 = \left( \frac{\rho l^2}{l_0 w_0 t_0} \right) \left( \frac{w_0 t_0}{\rho l_0} \right) - 1 = \left( \frac{l}{l_0} \right)^2 - 1 \quad (48)$$

By substituting the expression of the longitudinal strain for positive elongation ( $l > l_0$ )

$$\varepsilon = \frac{\Delta l}{l_0} = \frac{l - l_0}{l_0} = \frac{l}{l_0} - 1 \quad (49)$$

the relative resistance change can be expressed as a function of the strain  $\varepsilon$

$$\frac{\Delta R}{R_0} = (1 + \varepsilon)^2 - 1 = \varepsilon^2 + 2\varepsilon = (\varepsilon + 2)\varepsilon \quad (50)$$

Finally, the theoretical  $GF$  can be also determined as follows

$$GF = \frac{\Delta R/R_0}{\varepsilon} = \varepsilon + 2 \quad (51)$$

To develop sensing structures capable to detect strain states by changing resistance value, it is necessary to design structures that allow to facilitate elongation. Stretchable materials, such as polymer-based materials, also undergo notable changes in other geometric dimensions, i. e. width and thickness.

Stretchable sensors based on the piezoresistive sensing mechanism can exhibit a different response from the theoretical relationship between the relative resistance change and the applied strain due to the material resistivity change caused by events internal to the conductive material.

#### 4.2 SINGLE STRIPE-SHAPED SENSOR DESIGN

The produced conductive composite is utilized to fabricate stripe-shaped samples characterized by strain sensing capability based on piezoresistive behavior. The structure design of the single stripe sensor is based on a simple sandwich structure where layers with different material and electrical properties alternate each other.

The layers are characterized by rectangular cross-sectional area, with a set thickness dimension less than 500  $\mu\text{m}$ , in order to create thin structures which can advance the parameter of stretchability. Also, the length parameter is set to improve the device's suitability for multiple wearable applications. More specifically, the conductive sensing part is placed between two non-conductive support layers, as shown in Figure 36. This part is made of Ag-PDMS composite, whereas the support parts are made of pure PDMS. Since the fabricated conductive PDMS is inherently the same material as pure PDMS, it is able to form strong bonds with the non-conductive layers perfectly.

The final stripe sensor is formed by

- lower support layer made of pure PDMS
- sensing layer made of conductive Ag-PDMS
- upper support layer made of pure PDMS

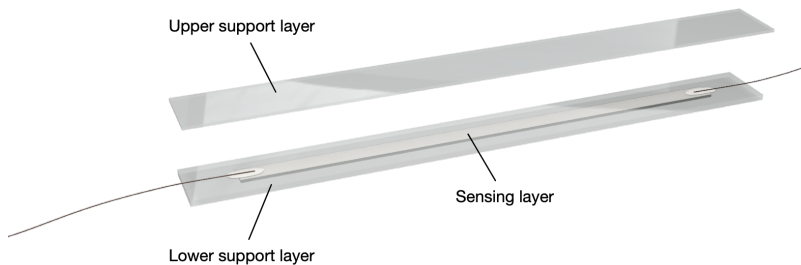


Figure 36: Render 3D model of the stripe sensor's parts.

#### 4.2.1 Mold Design and Fabrication

The lower support part of the stripe sensor is fabricated by using a mold casting method, pouring the liquid polymer into custom-made 3D printed molds.

These are created with fast and low cost FDM (Fused Deposition Modeling) 3D printing process by using a Prusa multi-material 3D printer extruding a continuous filament of thermoplastic material. The chosen material for the printing filament is the thermoplastic polymer ABS (Acrylonitrile Butadiene Styrene) due to its suitability for 3D printing process on FDM machines.



Figure 37: 3DXTech ABS 3D printing filament.

At first, the desired structure of the mold is designed by using the CAD software Autodesk<sup>®</sup> Inventor.

The internal geometric dimensions of the designed 3D printed mold replicate the lower support layer dimensions

length:  $l = 60 \text{ mm}$

width:  $w = 6 \text{ mm}$

thickness:  $t = 0.6 \text{ mm}$

In addition, a stripe is designed in the middle of the internal part of the mold according to the desired geometric parameters of the sensing layer

length:  $l_s = 50 \text{ mm}$

width:  $w_s = 2 \text{ mm}$

thickness:  $t_s = 0.3 \text{ mm}$

This feature allows to create a hollow shape in the PDMS part, which can be filled with the conductive composite during the next fabrication step. This leads conductive part to be completely embedded into the non-conductive lower support layer.

The external geometric dimensions, labeled by the “ $e$ ” subscript in Figure 38, are not significant for the sensor structure design. These can be set freely since are relevant only to the printing time.

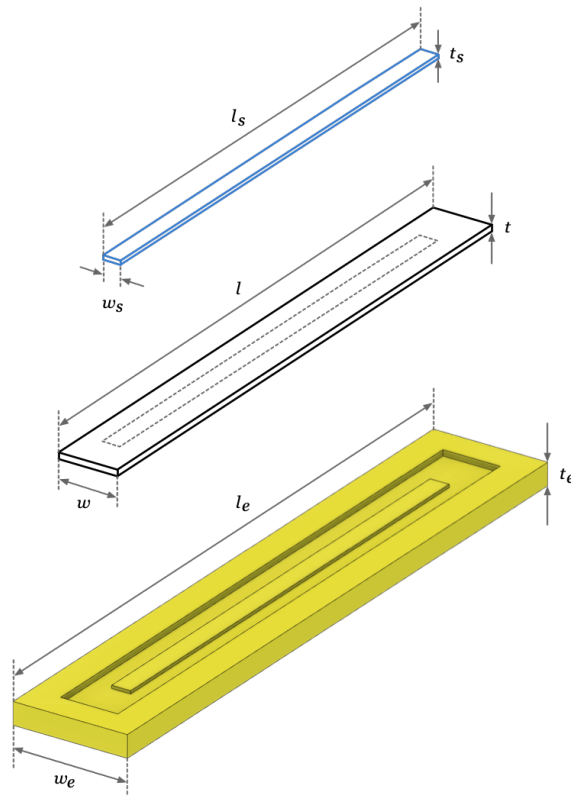


Figure 38: Geometric design of the 3D printed mold.

The file of the final designed 3D model is exported as .STL file and then imported into the 3D printer slicer software. For this purpose, the Slic3r-based software PrusaSlicer is used in order to process the CAD model preparing it to the effective printing.

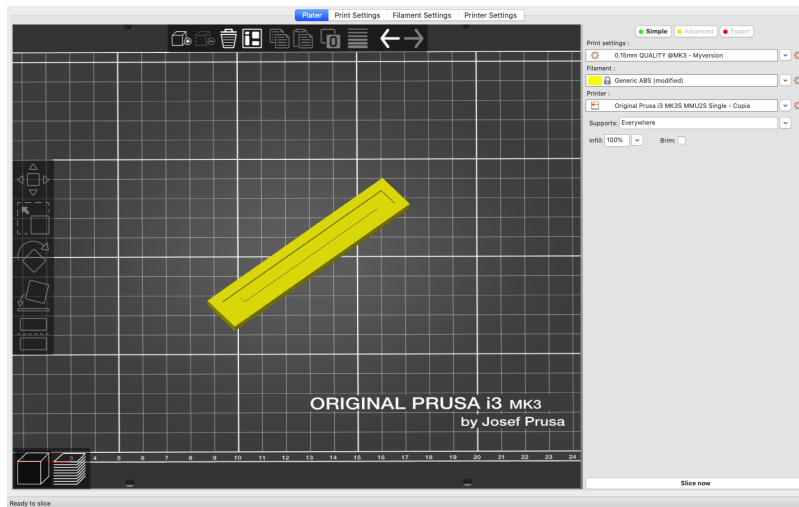


Figure 39: 3D editor view of the scaled up model.

---

#### Print settings

---

print profile	0.15 mm quality @MK3
fill density	100%
fill pattern	rectilinear
layer height	0.15 mm
speed for print moves	20 mm s <sup>-1</sup>

---

#### Filament settings

---

type	generic ABS
diameter	1.75 mm
density	1.04 g cm <sup>-3</sup>
extrusion multiplier	1
extruder temperature	255 °C
bed temperature	100 °C

---

#### Printer settings

---

model	Prusa i3 MK3S MMU2S
preset	MMU2S single
extruder nozzle diameter	0.4 mm

---

Table 6: Slicer software settings.

Figure 39 shows the 3D editor view of the imported CAD model that is ready to be sliced. During this step both the print, the filament, and the printer settings can be set up by software in the proper way. Specific settings are shown in Table 6.

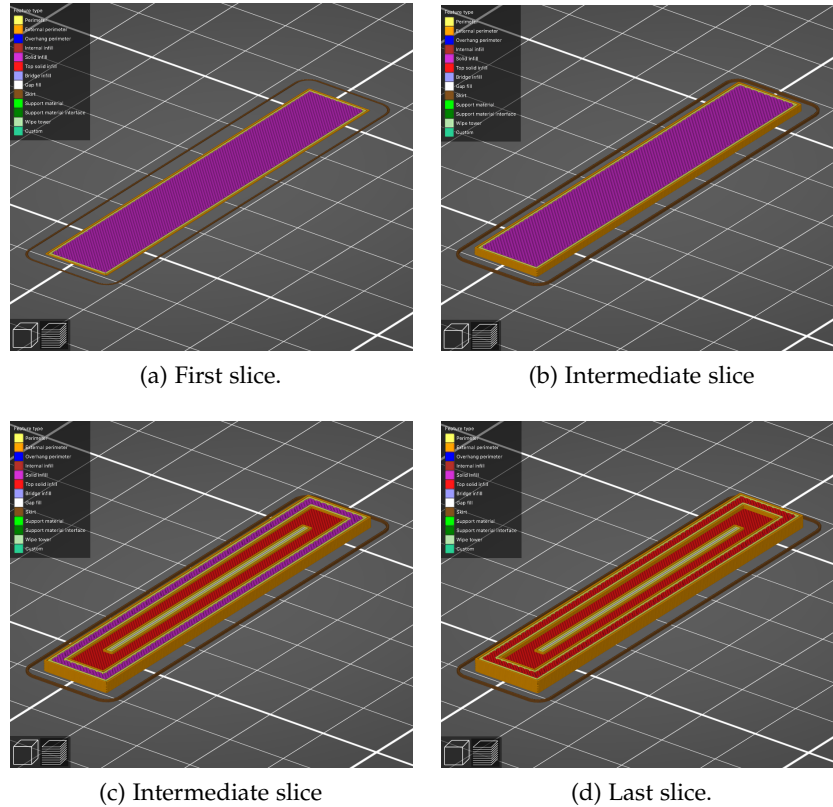


Figure 40: Slicing previews.

Once the settings set-up is completed, the model is sliced by the software. The result of the completed slicing process can be observed in the previews shown from Figure 40a to Figure 40d. By the slicing process, the corresponding G-code (Geometric Code) file is generated and can be exported. This kind of file is based on a programming language containing all the instructions for the printer head about how to accomplish movements in three dimensions as well as all the set up specific parameters which the printing machine needs to read throughout the printing process.

The surface of the printed mold shows a feature of evenness that depends strictly on the resolution limit of the printer's nozzle during the extrusion process. It entails a certain roughness grade of all the surface, so that the poured liquid polymer takes exactly the same surface imperfections during the curing time. In order to limit this effect, the surface of the mold can be exposed to acetone vapors for few minutes until the surface seems smoother and lighter.

This procedure to process molds is possible when ABS is used as filament material, since it is highly reactive to acetone, so that vapor smoothing process can work well to eliminate any visible layer lines.

#### 4.2.2 Silicon-based Polymer Preparation

Polydimethylsiloxane (Sylgard™ 184 Elastomer Kit), consisting of base elastomer (Part A) and curing agent (Part B), is used as soft material to fabricate both the support layers. To prepare the silicon-based polymer properly, the curing agent must be added to the mixture in the weight ratio of 1:10, i. e. 1 part of curing agent in 10 parts of elastomer base.

The base polymer and the curing agent are manually stirred in order to mix them. Generally, plastic containers are fine for mixing the two components. Containers with large surfaces can be better because can expose a larger surface of the contained fluid to air, which accelerates the degassing process. For this purpose, polystyrene antistatic weighing dishes are used. Once the dish is placed on the precision electronic scale, properly adjusted by pushing the “Zero” button, the polymer base is slowly poured into. Then, the curing agent is added according to the 1:10 mix ratio of curing agent and PDMS monomers. After that, the mixture is stirred by a disposable spatula for few minutes. There are many air bubbles in the mixture due to the mixing process, so it needs to be degassed in order to remove all of them. For this aim, the mixture is exposed to a vacuum for degassing. A desiccator is connected to a vacuum line to apply vacuum to the liquid mixture. After the mixture is placed into the desiccator, the vacuum valve on the desiccator is set to open and the vacuum line is activated.



(a) Desiccator connected to the vacuum line. (b) Open valve, vacuum line is turned on.

Figure 41: Set-up for starting the vacuum process.

When the mixture is into the desiccator, the vacuum induces the bubbles within the mixture to expand and rise up to the top surface in contact with air where they pop.

A wider surface in contact with air allows to improve this effect, decreasing the needed degassing time. The amount of time to degas the mixture depends on the amount of PDMS, that means more material to be mixed more air bubbles inside.

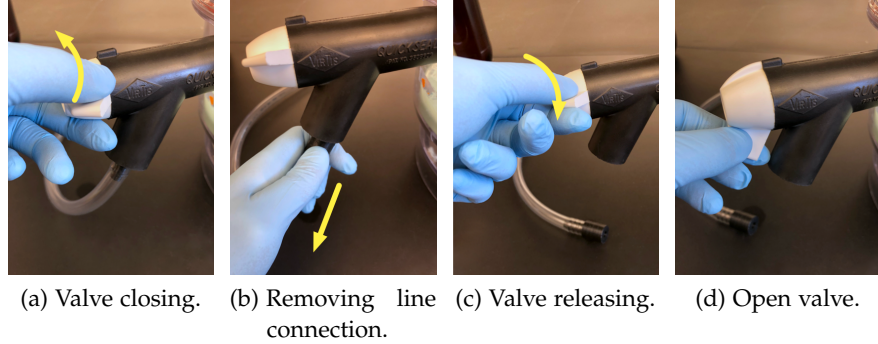


Figure 42: Valve reopening procedure.

When the mixture is ready to be taken out of the vacuum, the line is turned off and the valve is set to closed. Then, the valve is reopened slowly, as shown in Figure 42, to avoid sudden rush of air, so that the mixture can be removed from the desiccator.



Figure 43: Produced PDMS, before and after vacuum degassing.

Once the degassing process is completed, the surface of the liquid appears much smoother due to the total absence of bubbles inside it, as distinguishable from the comparison shown in Figure 43. Although there are no visible bubbles within the liquid polymer, any small bubbles that remain are removed during the curing process by contact with air.

## 4.3 STRIPE SAMPLE FABRICATION

When the liquid silicon-based elastomer is ready to be used, it is poured into the printed master mold. After the pouring process, some new air bubbles can appear inside the liquid polymer, so any further minutes of degassing are necessary.

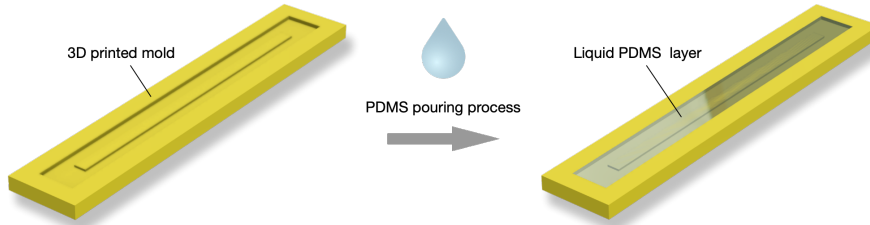


Figure 44: Pouring process into the custom-made mold.

After that, the liquid polymer hardens by the curing process with proper cure temperature and cure time. The used heating system is the Formlabs Form Cure, designed for curing parts placed on a rotating turntable which provides uniform exposure. The part is cured on the heating system at a temperature of 80 °C for 30 min, and left to cool at ambient temperature.

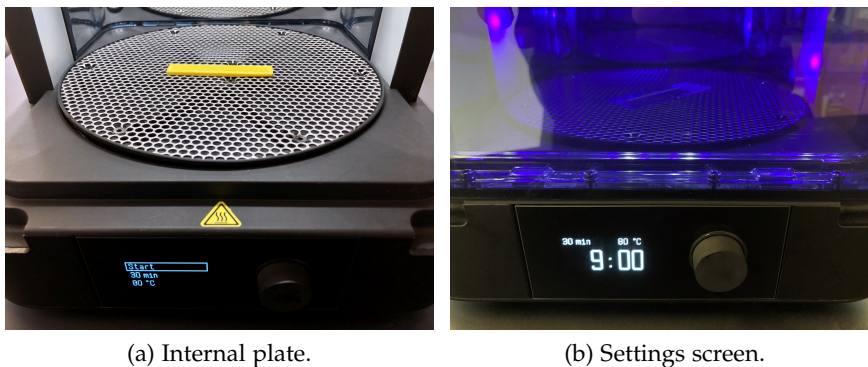
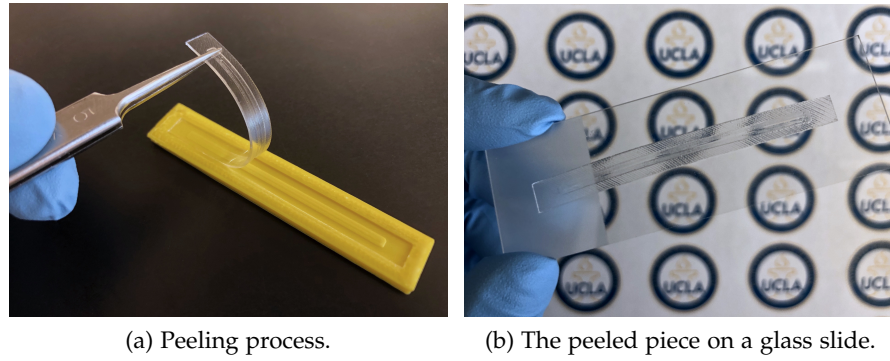


Figure 45: Heating system.

At the end of the curing process, the obtained solid PDMS part is gently peeled from the mold using tweezers, as shown in Figure 46a, since the material is very soft and the layer is thin. This part acts as lower support layer in the sensor structure and is used as polymeric mold for pouring the conductive layer during the next step of fabrication.



(a) Peeling process.

(b) The peeled piece on a glass slide.

Figure 46: Obtained lower support layer.

For the realization of the conductive sensing layer, the conductive Ag-PDMS composite is produced by following the fabrication method described in Section 3.3 of Chapter 3. The composite shows the texture like a viscous paste, due to the high filler concentration  $wt_{Ag}\%$ , therefore the pouring process is not immediate as in the case of pure liquid polymer.

The composite is deposited onto the surface of the lower support layer which acts as soft mold: to ease the process, a blade is used to apply the composite on the surface homogeneously like stencil printing process. The procedure is shown through a simple sketch of the side view of the structure in Figure 47.

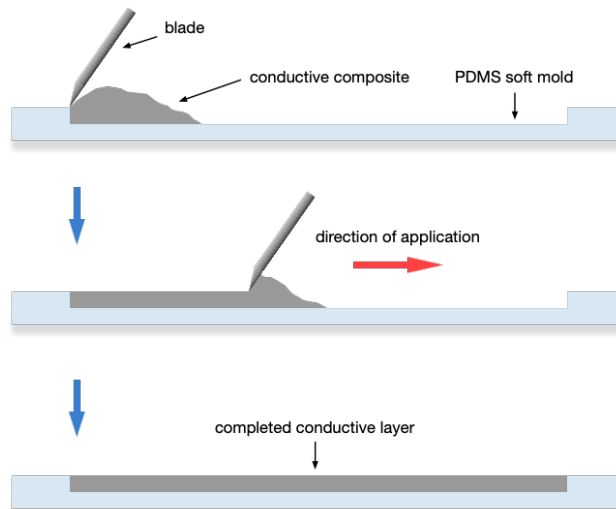


Figure 47: Conductive layer deposition procedure.

The same step of curing performed for the lower support layer, based on a cure temperature and a cure time of  $80\text{ }^{\circ}\text{C}$  and 30 min, respectively, is then replicated in order to obtain the solid conductive layer properly embedded into the support layer, as shown in Figure 48.



Figure 48: Conductive layer properly applied on the lower support layer.

At this point of the sensor fabrication, it is necessary to provide electrical connection to the sensor structure in order to connect sensor with external hardware for performing data acquisition.

For this aim, 34 AWG copper wire is bonded to the two conductive layer's far ends with conductive epoxy. In particular, MG Chemicals 9400, a silver-filled one-part epoxy adhesive with a low cure temperature, is applied onto the conductive layer and then cured at a temperature of 80 °C for 30 min.

The result of the wires connection is shown in Figure 49a.



(a) Wires connection.



(b) Complete stripe-shaped structure.

Figure 49: Wires connection by contact points on the conductive layer (a), and complete structure after pouring the upper support layer (b).

As last fabrication step, a final layer of pure PDMS is poured over the structure as upper support layer to fully cover the conductive layer and the wires connection.

This completes the sensor sandwich structure, as shown in Figure 50. The upper support layer is characterized by the same geometric dimensions of the lower support layer, corresponding to the internal dimensions of the printed mold, but with a thickness of 0.3 mm, in order to characterize the layers of the sensor structure with the same thickness value. An example of the complete stripe-shaped structure of the final sample is shown in Figure 49b.

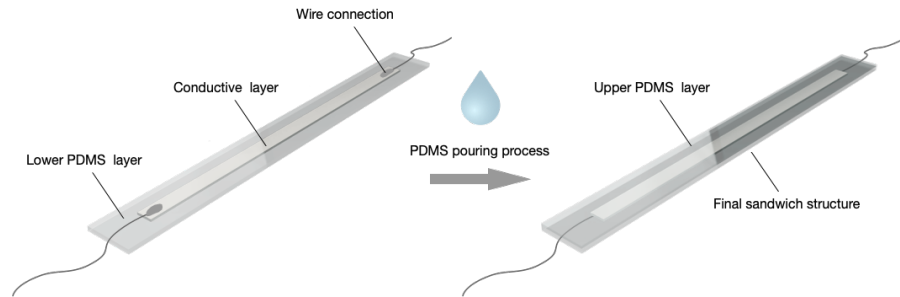


Figure 50: Pouring process to obtain the final sandwich structure.

The stretchability feature of the fabricated samples is demonstrated by applying a simple stretching, as shown in Figures 51a and 51b. In addition, the samples show a high level of flexibility, as shown in Figures 51c and 51d related to applied states of bending and twisting, respectively.

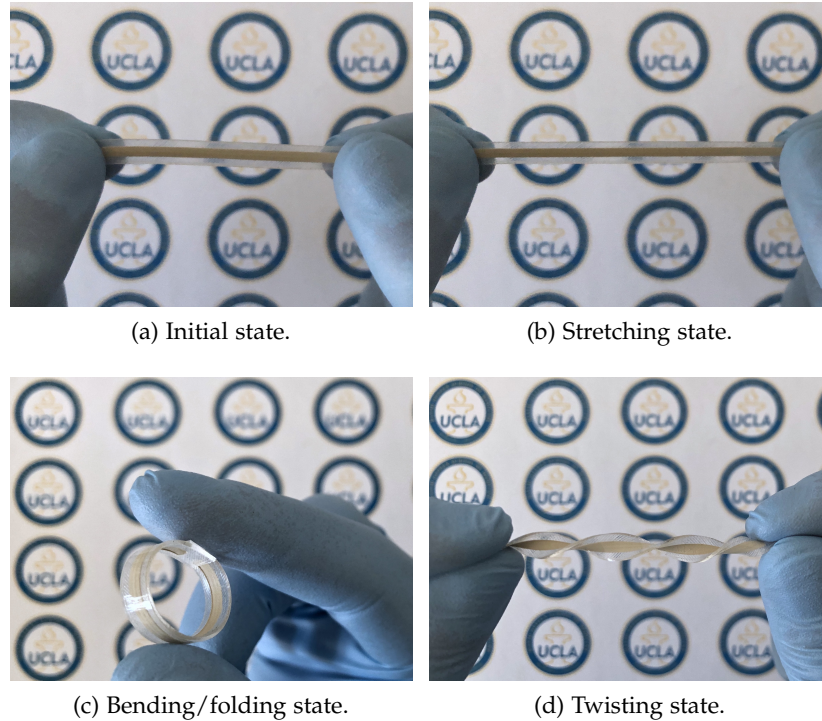


Figure 51: Strain sensor in different states.

4.3.1 *Led Test*

To demonstrate the sensor's capability to conduct electricity, the simple circuit shown in Figure 52 is implemented. A LED (light-emitting diode) is powered by a constant voltage source and the stretchable sensor, which acts as a variable resistor, is connected in series with it.

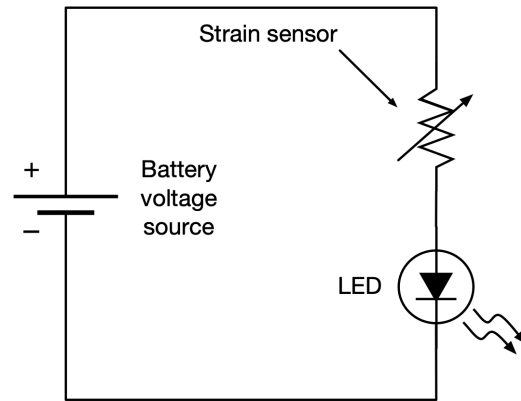


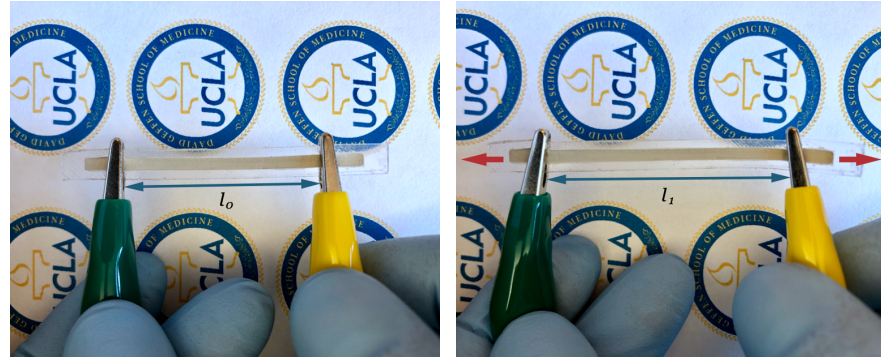
Figure 52: Series electrical circuit of LED and sensor.

The tested sample is clipped by two double ended alligator clips in order to perform stretching maintaining electrical connection with the LED simultaneously. When the sample is clipped, the LED emits intense light since the initial resistance value of the sample is in the order of few Ohms, as shown in Figure 53.



Figure 53: Emitting LED due to electrical continuity.

A strain state in the form of elongation is applied on the sample while it is connected to the circuit by the clips. The sample undergoes the applied stretching which leads to an increase in its length, as shown in Figure 54.



(a) Initial unstretched condition.

(b) Stretched condition.

Figure 54: Stretching applied to the sample.

As observed, by applying stretching to the sensor, the sudden increase of sensor resistance leads the intensity of light emission to decrease. When the sensor is released, resuming the initial unstretched condition, it restores the initial resistance value so that the LED emits maximum light since the current flowing through it becomes greater.

## CHAPTER FIVE

## 5.1 BOARD SET-UP

To acquire the real-time electromechanical response of the developed samples, it is necessary to connect the developed samples to a specially programmed microcontroller. Therefore, the connection allows to perform continuous sensing acquisition of the analog signals from samples. For this purpose, the signals related to the electrical resistance change due to the piezoresistive effect are measured by using the Adafruit ESP32-based Feather Huzzah32 Board, based on a 240 MHz dual core Tensilica LX6 32-bit microcontroller. The model of the programmed board is shown in Figure 55.

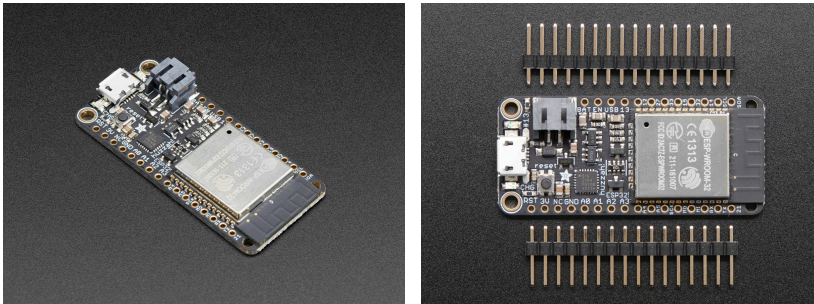


Figure 55: HUZAZH32 – ESP32 Feather Board.

The board comes fully assembled with a USB interface that lets user quickly use it with the Arduino IDE. In order to properly program an ESP32-based development board on the IDE, a few of preliminary steps are required.

The first step is installing the driver responsible for bridging the USB connection from a PC to the ESP32 via UART. Then, the following steps are based on the board manager of the Arduino IDE using the feature for including additional boards. In particular, it is necessary to search the ESP32 class of boards on the web since it is not included by default in the board manager.

On the IDE Preferences window, the following link needs to be added as text into the Additional Boards Manager URLs field:

[https://dl.espressif.com/dl/package\\_esp32\\_index.json](https://dl.espressif.com/dl/package_esp32_index.json)

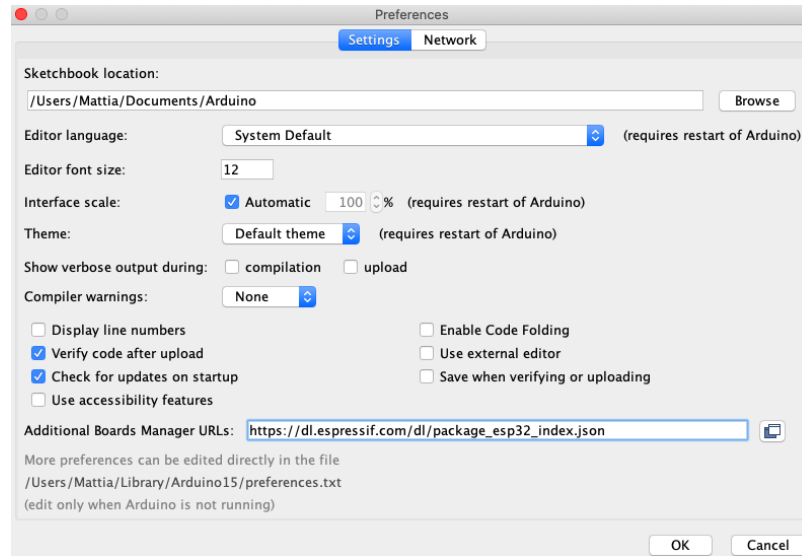


Figure 56: Arduino IDE Preferences.

In this way the board manager on the IDE allows to find and then install additional ESP32 boards. In the board manager, searching for the word “ESP32” and selecting the result called “esp32 by Espressif Systems”, a whole list of boards can be installed. Finally, on the Tools panel, under the voice Board, “Adafruit ESP32 Feather” is selected. Hence, the ESP32 board can be programmed allowing to use a large number of pins, named GPIO, as general purpose input/output pins, as well as control I2C and SPI devices. Also, the ESP32 runs on 3.3 V power and logic, so it must be considered when any general purpose IO pin will be used.

## 5.2 RESISTANCE CHANGE READING

The main aim is properly reading the current resistance value of the sensor while it is attached on human body and exposed to external strain due to performed movements. For this purpose, the resistance change based on the sensing mechanism of piezoresistive sensors needs to be acquired. This change can be seen as the relative change of electrical resistance, divided by the initial resistance value of the sensor corresponding to the initial rest condition without any movement performed.

The two sensor’s far ends are connected by copper wires and the ends of the two wires are soldered with Dupont style connector male pins. Therefore, the sensor can be connected to the ESP32 board in order to start the signal acquisition.

Since the sensor can be interpreted as a resistor that continuously changes its resistance value while strain is applied, the implemented method is easily based on analog-digital conversion of the acquired signal from the sensor.

### 5.2.1 Analog-to-Digital Conversion

The A/D conversion is performed by using one of the two Analog-to-digital Converters (ADCs) integrated on the board. In particular, the ESP32 integrates two multichannel 12-bit SAR (Successive Approximation Register) ADCs.

In a successive-approximations converter a series of known analog voltages are created and compared to the analog input voltage. The output from the comparator is continuously monitored and compared with the analog signal input. In the first trial, a voltage interval of one-half the input span is compared with the input voltage. This comparison determines whether the input voltage is in the upper or lower half of the input range. If the input voltage is in the upper half of the range, the most significant bit (MSB) is set to 1, otherwise it is set to 0. This process is repeated considering an interval half the width of the interval used in the last trial in order to determine all the bits until the least significant bit (LSB) is determined. For a N-bit converter, N steps of comparison are required.

Figure 57 shows an example of basic architecture for a 12-bit successive approximation A/D converter.

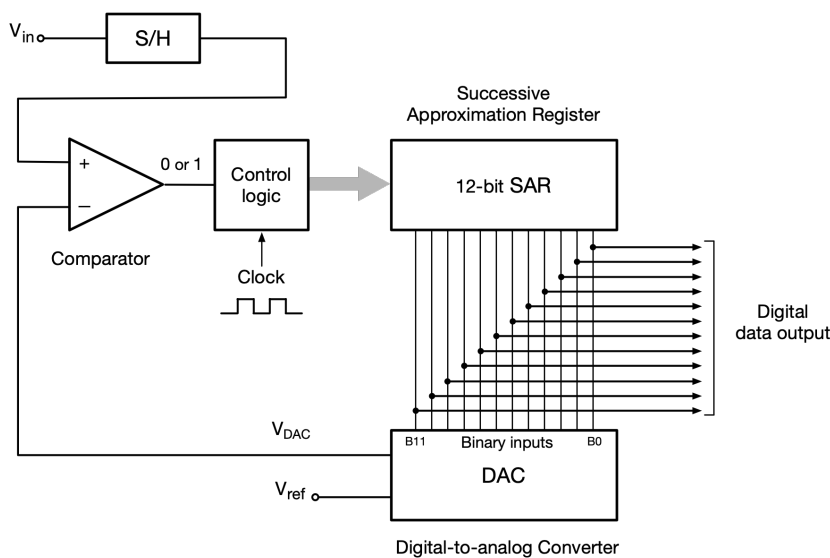


Figure 57: Block diagram of a 12-bit SAR ADC.

The reference voltage increment, created in each clock tick, is

$$\Delta V = \frac{\text{input span}}{2^N} \quad (52)$$

The integrated ADCs have a 12-bit resolution, so that analog signals can be divided in a number of discrete levels, known as quantization levels, equals to

$$N_{\text{levels}} = 2^N \quad (53)$$

where  $N = 12$  is the bit resolution of the ADC. Hence, the output values can represent the range from 0 to  $2^{12} - 1$  as unsigned integers. In addition, the resolution can be defined in terms of volts, corresponding to the smallest change in analog signal that will result in a change in the digital output. The voltage resolution of the ADC can be expressed as

$$V_{\text{res}} = \frac{V_{\text{FSR}}}{2^N} \quad (54)$$

where  $V_{\text{FSR}}$  is the voltage full scale range, i. e. the overall voltage measurement range

$$V_{\text{FSR}} = V_{\text{ru}} - V_{\text{rl}} \quad (55)$$

where  $V_{\text{ru}}$  and  $V_{\text{rl}}$  represent the upper and lower values of the input range.

The resolution also represents the quantization error inherent in the conversion of the signal to digital form. Indeed, since the output of the ADC changes in discrete steps, a resolution error, known as quantization error, can be defined

$$\text{resolution error} = \pm \frac{1}{2} V_{\text{res}} = \pm 0.5 \frac{V_{\text{ru}} - V_{\text{rl}}}{2^N} \quad (56)$$

In the practical case of the adopted implementation, the output code used to represent the digital output of ADC is simple binary output. This means that ADC maps input voltages between  $V_{\text{rl}}$  and  $V_{\text{ru}}$  into integer values between 0 and  $2^{12} - 1$ .

Table 7 summaries the input and output values which are considered for the A/D conversion process.

analog input	description	digital output	description
0 V	zero voltage	0	lower limit
3.3 V	operating voltage	4095	upper limit

Table 7: I/O limit values.

According to the input range of 0–3.3 V, the voltage resolution results

$$V_{\text{res}} = \frac{(3.3 - 0)V}{2^{12}} \approx 0.000806 \text{ V} = 806 \mu\text{V} \quad (57)$$

and the quantization error is equal to

$$\text{resolution error} \approx \pm 0.5 \times 806 \mu\text{V} = \pm 403 \mu\text{V} \quad (58)$$

which implies a resolution uncertainty, calculated on the voltage input range, of about  $\pm 0.012\%$ .

Ratiometric measurements are measurements where the signal being measured is related to the ADC reference. The ESP32 ADC assumes the system voltage (3.3 V) is the reference voltage so that all the voltage measurements are performed according to the following ratio

$$\frac{\text{ADC resolution}}{\text{system voltage}} = \frac{\text{ADC reading}}{\text{analog voltage measured}} \quad (59)$$

Rearranging to get the analog voltage measurement, it becomes

$$\text{analog voltage measured} = \text{ADC reading} \times \frac{3.3 \text{ V}}{4095} \quad (60)$$

### 5.3 HARDWARE SET-UP

The changing signal from the sensor is of analog type, therefore an analog pin on the board must be used in order to properly send the analog signal to the analog input on the ADCs of the board. Indeed, it should be noted that not every pin on a microcontroller has the ability to read analog voltages and perform A/D conversions.

The ESP32 board offers a certain number of pins to be used as analog pins. The analog inputs available for using the ESP32 ADCs are shown in Figure 58.

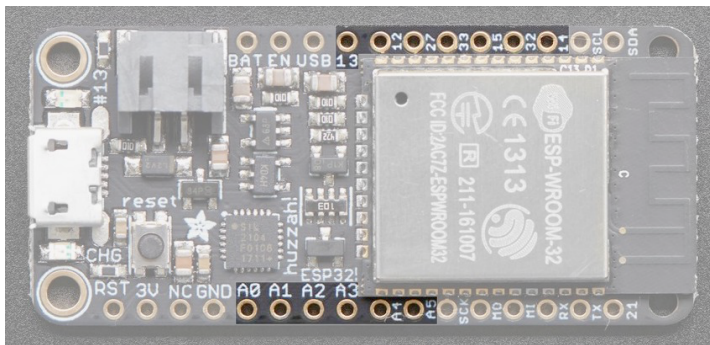


Figure 58: Analog Pins.

The ESP32 microcontroller operates at a system voltage of 3.3 V and the 3V pin is the output from the 3.3 V regulator. One terminal of the sensor is connected with the 3V pin, whereas the other one is connected with the selected analog pin, as shown in the circuit schematic in Figure 59.

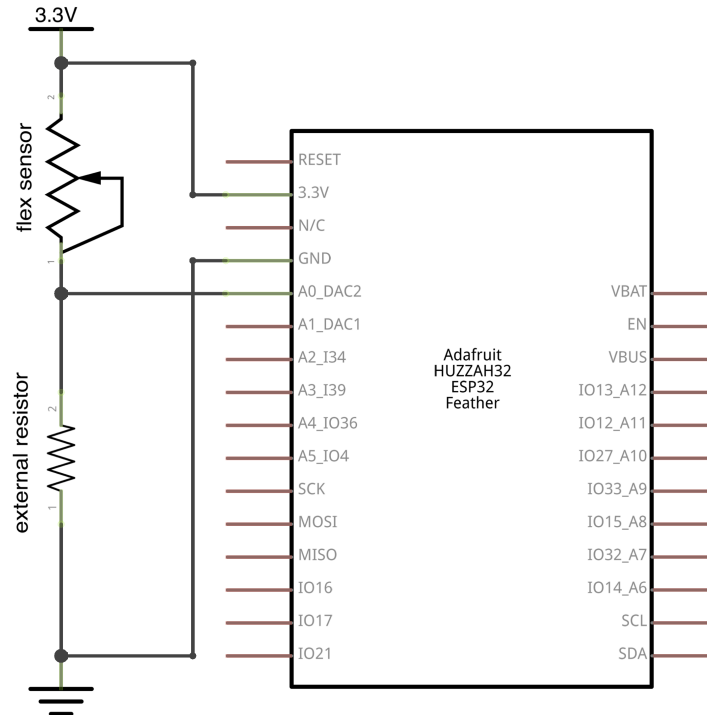


Figure 59: Electrical circuit schematic.

In order to take advantage of the voltage divider principle, an external resistor is added to the circuit. For that purpose, the external resistor, with fixed resistance value, is connected between the same analog pin the sensor is connected with and the common ground pin (GND).

The external resistance value should be chosen according to the order of magnitude of the sensing resistance range; in other words it depends on the voltage range to send as input on the analog input of the ADC. For this reason, the external resistor can change on the basis of the required application.

### 5.3.1 Voltage Divider Method

Adding the external resistor in series with the resistive sensor, the output voltage becomes a fraction of the input one. It means the voltage measured by the ADC will be a fraction of the system voltage.

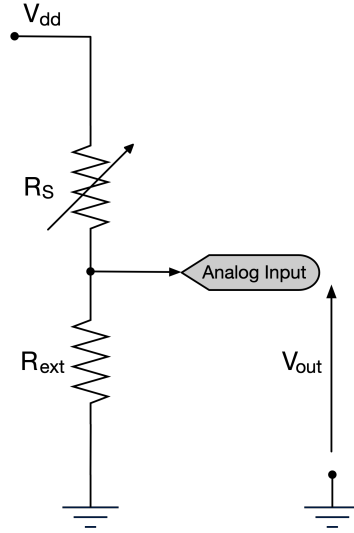


Figure 60: Voltage divider configuration.

Referring to Figure 60, the voltage drop across the external resistor, according to the voltage divider principle, is given by

$$V_{\text{out}} = V_{\text{dd}} \frac{R_{\text{ext}}}{R_{\text{ext}} + R_{\text{S}}} \quad (61)$$

where

$V_{\text{out}}$  voltage drop across the external resistor (V)

$V_{\text{dd}}$  system voltage (V)

$R_{\text{ext}}$  resistance of the external resistor ( $\Omega$ )

$R_{\text{S}}$  resistance of the flex sensor ( $\Omega$ )

Therefore, the sensing resistance value  $R_{\text{S}}$  can be calculated from Equation 61 as follows

$$R_{\text{S}} = \left( \frac{V_{\text{dd}}}{V_{\text{out}}} - 1 \right) R_{\text{ext}} \quad (62)$$

Following an equivalent way, sensing resistance value  $R_{\text{S}}$  can be calculated by measuring the voltage drop across the sensor  $V_{\text{S}}$

$$V_{\text{S}} = V_{\text{dd}} - V_{\text{out}} \quad (63)$$

Therefore, expressing  $V_{\text{S}}$  by using the voltage divider principle

$$V_{\text{S}} = V_{\text{dd}} \frac{R_{\text{S}}}{R_{\text{ext}} + R_{\text{S}}} \quad (64)$$

The sensing resistance value  $R_{\text{S}}$  can be finally calculated

$$R_{\text{S}} = \frac{V_{\text{S}}}{V_{\text{dd}} - V_{\text{S}}} R_{\text{ext}} = \frac{V_{\text{S}}}{V_{\text{out}}} R_{\text{ext}} \quad (65)$$

The ESP32 ADC can be sensitive to noise leading to large discrepancies in ADC readings. To minimize noise, a  $0.1 \mu\text{F}$  capacitor is connected to the ADC input in use.

### 5.3.2 Software Set-up

The C++ code is written on the IDE in order to read input voltage values by using one of the ESP32 analog channels. The analog pin related to the selected analog input of the ADC is set as input. This is required when the selected channel can work in both input and output mode.

The following commands are used as first setup

---

```

//set-up parameters
2 float maxadc = 4095.0;
  float Vdd = 3.3;
  float Re = 2000.0;
  float Vo;
  float Rs;
7
const int analogPin = A0; //selected analog pin
pinMode(analogPin, INPUT);

```

---

The main loop contains the commands to read the analog signal on the analog pin for each iteration yielding a continuous voltage reading. The digital output of the ADC is stored into an integer variable and then converted to Volts according to Equation 60 on page 77.

Finally, sensing resistance value is calculated according to the voltage divider method by applying Equation 62 on the previous page.

---

```

1 int readV = analogRead(analogPin); //ADC reading
  Vo = (float)readV*(Vdd/maxvadc); //measured voltage
  Rs = (Vdd/Vo-1.0)*Re; //measured sensing resistance

```

---

## 5.4 MULTIACQUISITION

The reported hardware-software configuration allows to obtain multiple reading from different sensors in the same time. Two multiplexers are used to perform multiacquisition from a fixed number of different sensors.

The CD74HC4067 is a high-speed CMOS Logic 16-Channel Analog Multiplexer/Demultiplexer that features 16 channels of selectable inputs/outputs. The routing of common signal to independent I/O is set by digitally controlling 4 select lines, which can be set either high or low into one of 16 binary combinations. The chip allows to connect up to 16 analog sources to 4 pins on a microcontroller.

This is a great way to connect the sensor to a few pins since it allows sensors to operate on only 4 pins of the microcontroller. Table 8 summarizes each pin and the related function.

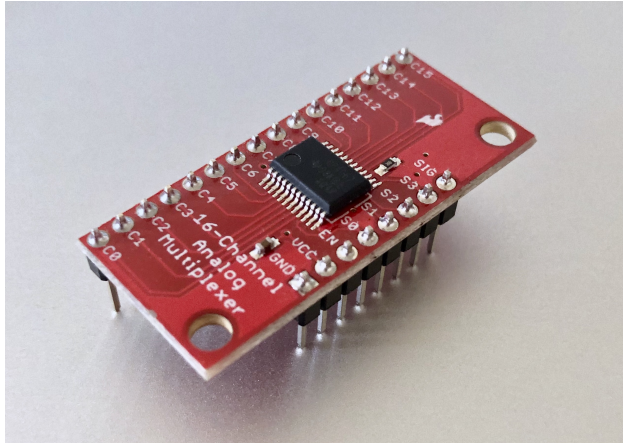


Figure 61: Breakout CD74HC4067.

Pin Label	Function	I/O	Description
C0, . . . , C15	Independent I/O	Input/Output	Selectable I/O to be routed to common pin.
S0, S1, S2, S3	Select controls	Input	Select inputs, S3 is the MSB and S0 is the LSB.
SIG	Common I/O	Input/Output	Common output or input.
EN	Enable	Input	Active low enable.
VCC	Positive supply	Supply	Positive supply voltage.
GND	Ground	Supply	Ground supply voltage.

Table 8: MUX pins.

Since the control lines are based on 4 digital pins of the board, it is necessary set the proper digital value for each of these bits in order to form the exact binary address of the channel to be selected.

The 4-bit digital word is stored into an integer array where the first value corresponds to the first bit, the second value to the second bit and so on. In this way, when the MUX switches to a channel, the corresponding digital code is created and set on the control lines. This operation is continuously repeated to select all the channels one after the other.

The control pins are set as output, and before the selection the Low level, corresponding to the Logic 0 is set as well.

---

```

#define N 16 //channels number
2 int ch_mux; //Mux channel
  int controlPins[4] = {12, 13, 14, 15};
  int inPin = A0;
  int readv = 0;
  float maxvadc = 4095.0;
7 float Vdd=3.3;
  float Re = 150.0;
  float Vo;
  float Rs;
  float R_ch[N]={};
12
  //function for the mux channels selection
  void setcontrolPins(int channel, int digitalPins[4])
  {
    for (int i=0; i<4; i++)
17 {
      if (channel & (1<<i))
        digitalWrite(digitalPins[i], HIGH);
      else
        digitalWrite(digitalPins[i], LOW);
22 }
  }

```

---

The function `setcontrolPins`, implemented for selecting channels, uses the bitwise AND operator (`&`) to compare each bit of the first operand (`channel`) to the corresponding bit of the second operand (`1<<i`). If both bits are 1, the corresponding result bit is set to 1 (High level), otherwise, the corresponding result bit is set to 0 (Low level).

---

```

void setup()
2 {
  Serial.begin(115200);
  pinMode(inPin, OUTPUT);
  for (int i=0; i<4; i++)
  {
7   pinMode(controlPins[i], OUTPUT);
     digitalWrite( controlPins[i], LOW);
  }
}

```

---

Once the channel is selected by the function, the voltage reading is executed by the `analogRead` command and the calculation to obtain the related resistance reading by using the voltage divider method is made.

Figure 62 shows the schematic of the implemented connection between the used hardware components and the fabricated samples for performing multiacquisition based on the multiplexing strategy.

---

```

void loop()
{
for (int ch_mux=0; ch_mux<N; ch_mux++)
{
5  setcontrolPins(ch_mux, controlPins);
  pinMode(inPin, INPUT);
  int readV = analogRead(inPin);
  Vo = (float)readV*(Vdd/maxvadc);
  Rs = (Vdd/Vo-1.0)*Re;
10 R_ch[ch_mux] = Rs;
  pinMode(inPin, OUTPUT);
  delay(1);
}
}

```

---

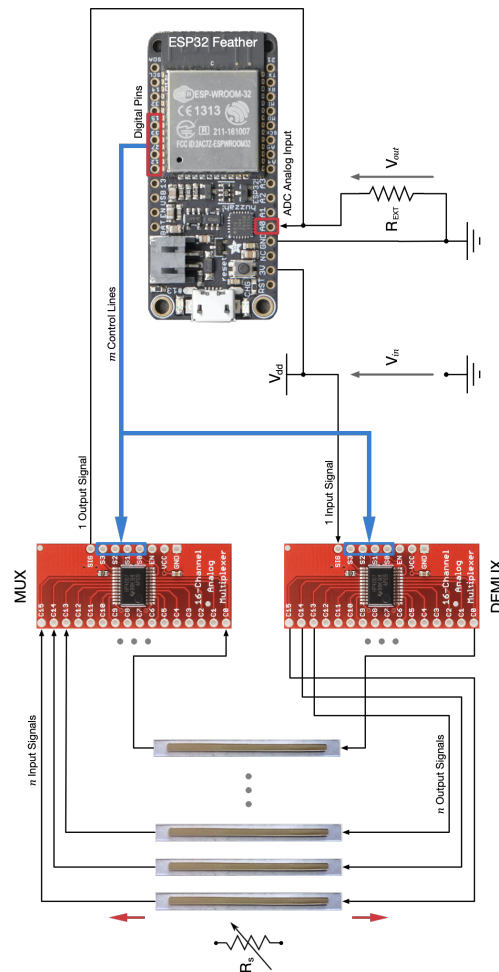


Figure 62: Connection based on the multiplexing strategy.

## 5.5 HIGH RESOLUTION ANALOG-TO-DIGITAL CONVERTER

The AD774x (© Analog Devices, Inc.) family includes single chip high resolution  $\Delta\Sigma$  Capacitance-to-Digital Converters (CDCs) that provide system level solutions for capacitance and voltage conversions with high resolution, high linearity, and high accuracy.

The AD7745 has one capacitance input channel, while the AD7746 has two input channels, but all other features are identical for both. Since these converters are designed for floating capacitance sensing, both capacitive plates have to be isolated from ground. On the contrary, the AD7747 version is available to measure capacitance with one plate connected to ground. The parts have also a standard voltage input, which allows to easily interface with an external sensor.

The architecture of the CDC opens up high performance applications also in medical instrumentation. The suitability for those applications is due to the combination of high precision, low power, low temperature drift, low noise, low cost, and reduced size.

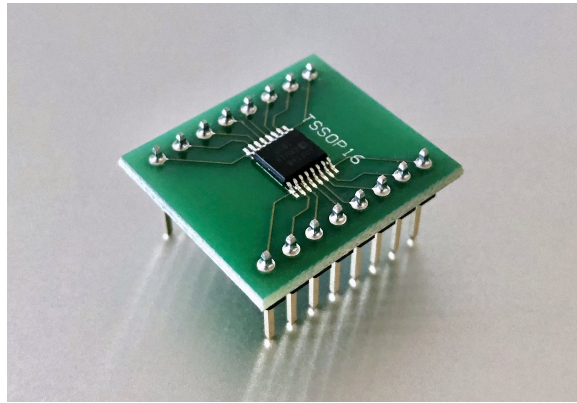


Figure 63: 16-TSSOP Breakout AD7746.

The parts are housed in small 16-lead TSSOP (Thin Shrink Small Outline Package) packages, so wiring up a breakout board could be necessary for rapid and easy prototyping. Figure 63 shows the used chip soldered to a TSSOP to DIP socket adapter produced by Aries Electronics.

### 5.5.1 Hardware Description

The high resolution converter consists of a 2nd order  $\Delta\Sigma$  modulator and a 3rd order digital filter. It can work as Capacitance-to-Digital Converter (CDC) for capacitive input as well as Analog-to-Digital Converter (ADC) for voltage input. For this reason, the chip includes channels for both capacitive and voltage analog input.

In addition to the converter, the chip integrates:

- multiplexer;
- excitation source;
- CAPDACs<sup>1</sup> for the capacitive inputs;
- temperature sensor;
- voltage reference for the voltage and temperature inputs;
- complete clock generator;
- control and calibration logic;
- I<sup>2</sup>C-compatible serial interface.

Since the AD7746 is used for all the purposes of the work, the related block diagram of its hardware components is shown in Figure 64.

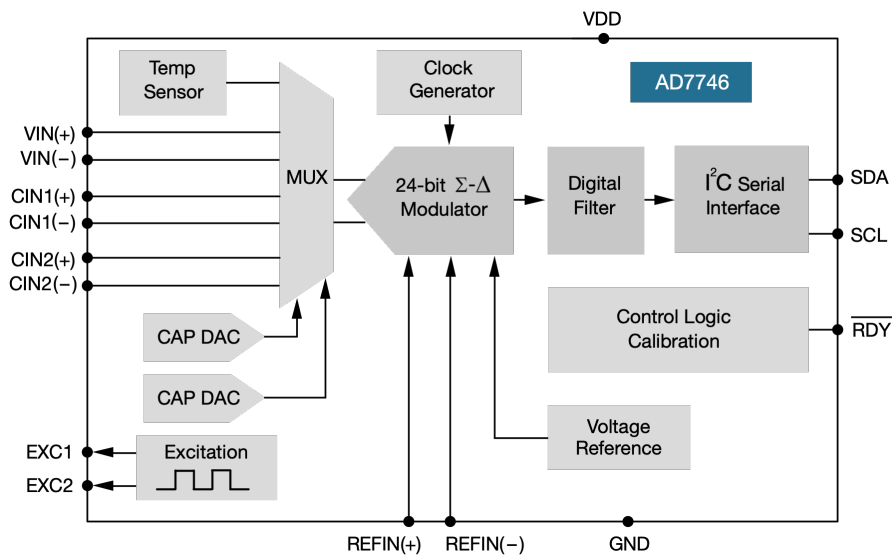


Figure 64: AD7746 Block diagram.

The conversion process is based on the  $\Delta\Sigma$  modulation, which is one of the possible methods for A/D converters to encode analog signals into digital signals. The main blocks of the 2nd order  $\Delta\Sigma$  modulator's architecture are represented in Figure 65.

<sup>1</sup> Programmable on-chip digital-to-capacitance converters.

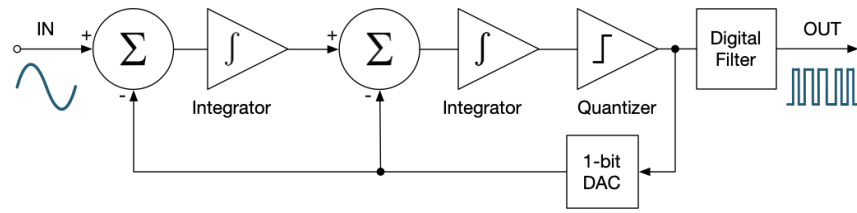


Figure 65: Block diagram of a second-order  $\Delta\Sigma$  modulator.

The modulator acquires and converts many samples of the analog input signal to produce a high-speed 1-bit digital stream. The conversion flow can include one or more integrators, which make a shaping of the quantization noise to higher frequencies. Since the number of integrators determines the order of the  $\Delta\Sigma$  modulator, 2nd order indicates the presence of two integrators. The output value of the quantizer is clocked back into the 1-bit DAC and the resulting analog signal is then subtracted from the analog input signal, leading to a consistent reduction of the error introduced by the modulation process.

### 5.5.2 Pins Configuration

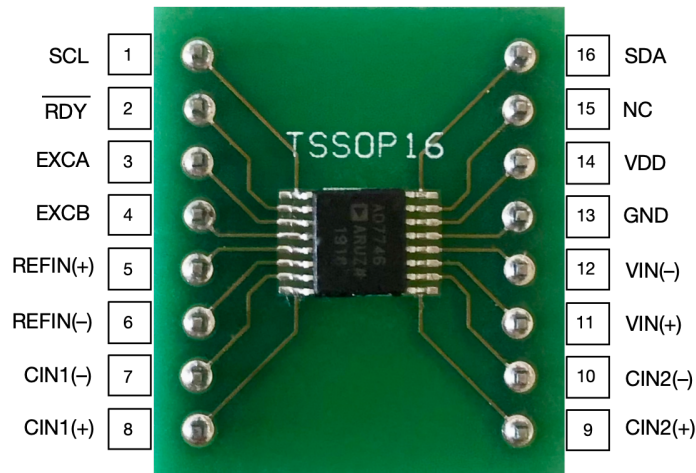


Figure 66: AD7746 Pin configuration (16-Lead TSSOP).

The chip integrates two different capacitance input channels and one voltage input channel, corresponding to pins 7 to 12, as shown in Figure 66. Each channel can be configured as single-ended by connecting only the positive (+) input or differential by connecting both the positive (+) and the negative (-) input.

A brief overview of the 16 pins of the AD7746 with their function description is reported in Table 9.

Pin No.	Pin Name	Description
1	SCL	Serial Interface Clock Input, connects to the master clock line.
2	$\overline{\text{RDY}}$	Logic Output.
3,4	EXCA, EXCB	CDC Excitation Outputs.
5,6	REFIN(+), REFIN(-)	Differential Voltage Reference Input for the voltage channel (ADC).
7	CIN1(-)	CDC Negative Capacitive Input in differential mode.
8	CIN1(+)	CDC Capacitive Input in single-ended mode or Positive Capacitive Input in differential mode.
9	CIN2(+)	CDC Second Capacitive Input in single-ended mode or Positive Capacitive Input in differential mode.
10	CIN2(-)	CDC Negative Capacitive Input in differential mode.
11, 12	VIN(+), VIN(-)	Differential Voltage Input for the voltage channel (ADC).
13	GND	Ground Pin.
14	VDD	Power Supply Voltage.
15	NC	Not Connected.
16	SDA	Serial Interface Bidirectional Data, connects to the master data line.

Table 9: Pin function description.

## 5.6 SERIAL INTERFACE

The AD7746 supports a 2-wire I<sup>2</sup>C-compatible serial interface. The Inter-Integrated Circuit, also known as I<sup>2</sup>C, is a serial computer bus used for connecting lower-speed peripheral ICs to processors and microcontrollers in short-distance. A clear advantage of this bus technology is the capability of a microcontroller to connect and control multiple devices with just two general-purpose I/O pins.

There are two bidirectional lines on the I<sup>2</sup>C bus:

- Serial Data Line (SDA) carries the data.
- Serial Clock Line (SCL) synchronizes the sender and receiver during the data transfer.

These carry all addressing, commands, and data information 1 bit at a time over the bus to all connected peripheral devices.

Wire library is added into the IDE by the following command, in order to establish communication with I<sup>2</sup>C devices:

---

```
1 #include <Wire.h>
```

---

The SDA/SCL pins of the ESP32 board are directly connected to the slave device. Pull-up resistors are needed when connecting SDA/SCL pins, so the two lines are connected to the 3.3 V power voltage by two 10 k $\Omega$  pull-up resistors.

Since Wire library is based on 7-bit addressing, addresses are in the range of 0 to 127 (decimal values). Also, the Wire library implementation is based on a 32 byte buffer, therefore any communication is within this limit.

Each node on the bus can have the role of master or slave:

- Master: the node generates the clock and starts communication – starting a data transfer message – with slaves.
- Slave: the node receives the clock and responds, when addressed by the master, to the data transfer message.

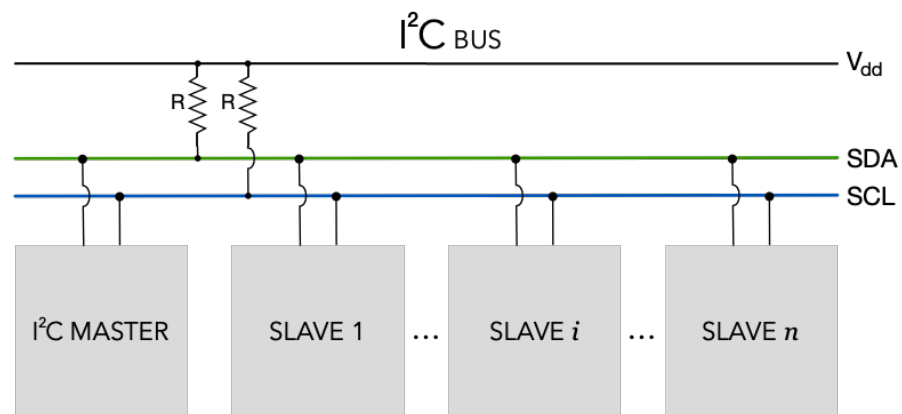


Figure 67: Generic example of I<sup>2</sup>C bus.

In the reported implementation, the ESP32 microcontroller works as master device, whereas the AD7746 acts as standard slave device on the I<sup>2</sup>C which requires a specific communication protocol to be controlled on the bus by the microcontroller.

When the master starts the communication, a sequence of events occurs in a specific order:

1. Start condition from the master: high-to-low (H→L) transition on SDA while SCL remains high.
2. 8-bit start byte from the master: 7-bit address plus a Read/Write bit indicator.
3. The peripherals connected to the bus respond to the start condition shifting in the next 8 bits.
4. The device that recognizes the transmitted address responds by pulling the SDA line low (H→L) during the 9<sup>o</sup> clock pulse (Acknowledge bit). The other devices withdraw from the bus and maintain the idle condition monitoring the two lines and waiting for the start condition and the correct address byte.

#### 5.6.1 Read/Write Operation

Since the bits are sent MSB (Most Significant Bit) first, the LSB (Least Significant Bit) of the start byte represents the direction of the data transfer corresponding to the Read/Write operation:

- $LSB = 0 \implies W \text{ operation}$   
The logic 0 means the master wishes to write information to the addressed device, specified by the 7-bit address; hence the master is in transmit mode and the AD7746 becomes the slave receiver.
- $LSB = 1 \implies R \text{ operation}$   
The logic 1 means the master wishes to read information from the addressed device, specified by the 7-bit address; hence the master is in receive mode and the AD7746 becomes the slave transmitter.

Since the used device is based on 7-bit addressing procedure, it is identified by a 7-bit address, as shown in Figure 68. Considering the address of the AD7746 is 0x48, the start byte address becomes:

- 0x90 for a W operation.
- 0x91 for a R operation.



Figure 68: Start byte address for Read/Write operation.

All communications with the AD7746 on the bus start with an access to the Address Pointer (AP) Register that indicates from or to which register the operation will take place. The Address Pointer Register is set up by a *W* operation from the master as soon as the slave device is accessed over the bus. After that, the master is able either to write data to or read data from the addressed slave's register:

- Write sequence:

The byte following the start byte is always the AP Register byte which points to one of the slave's internal registers. This byte, known as subaddress, is automatically loaded into the AP Register and the slave responds with an acknowledge (ACK). After the ACK from the slave, the master can respond by sending:

- a stop condition;
- a repeated start condition;
- a data byte.

When a data byte is transmitted after the register AP Register byte, the device loads the data byte into the register addressed by the AP Register and sends the ACK, so that the AP auto-incrementer automatically increments the AP Register to the next internal register address. It means that subsequent transmitted data bytes are loaded into sequentially incremented addresses.

- Read sequence:

The register that is currently addressed by the AP is transmitted onto the SDA line by the slave. This is clocked out by the master and the slave waits for an ACK from the master:

- If the ACK is received, the AP auto-incrementer automatically increments the AP Register and outputs the next addressed register's content onto the SDA line.
- If no ACK (NACK) is received, the slave returns to the idle state and the AP is not incremented.

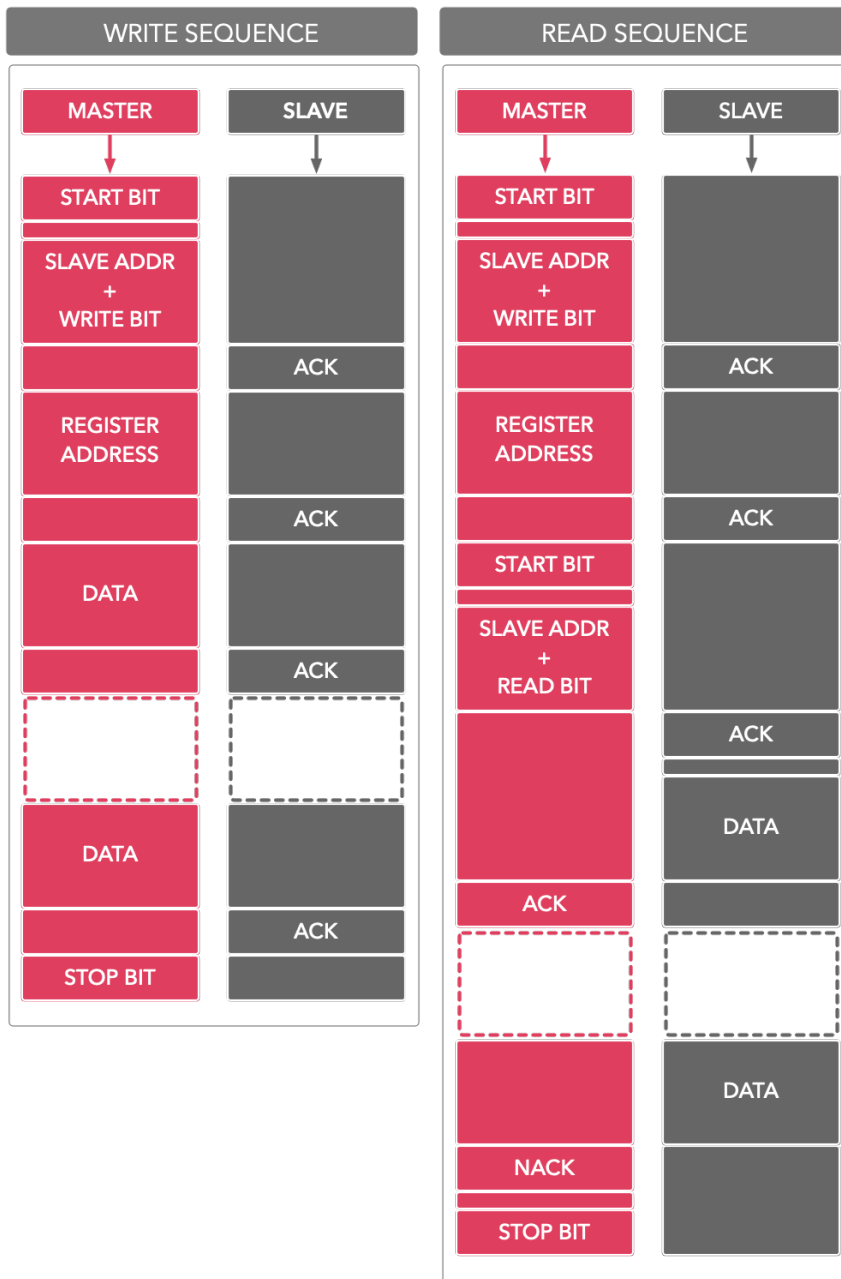


Figure 69: Write and Read Sequences.

In continuous conversion mode, the AP auto-incrementer is used for reading conversion results. Each conversion result corresponds to the 3 data bytes, which can be sequentially read by using the R sequence with the AP auto-incrementer feature of the serial interface.

At the end of the R sequence, when the master device issues a stop condition, the Address Pointer is reset to the address 0x00 but the master loses control of the bus. A stop condition, as the opposite of start condition, corresponds to a low-to-high (L→H) transition on SDA while SCL remains high.

In practical implementations, microcontroller issues repeated start conditions in place of the stop conditions so as to keep control of the transmission over the bus.

### 5.7 REGISTERS DESCRIPTION

The microcontroller can write to or read from all of the AD7746 registers except the AP Register, which is a write-only register and determines which register will be accessed during the next R/W operation. The device includes a total of 19 registers, specified by the Address Pointer from 0x00 to 0x12 (0 to 18 in decimal values).

The first 7 registers, corresponding to the Status Register (AP 0x00) and the six Data Registers (AP from 0x01 to 0x06), allow only R operations. The content of each register is stored as 1 byte value (8-bit value).

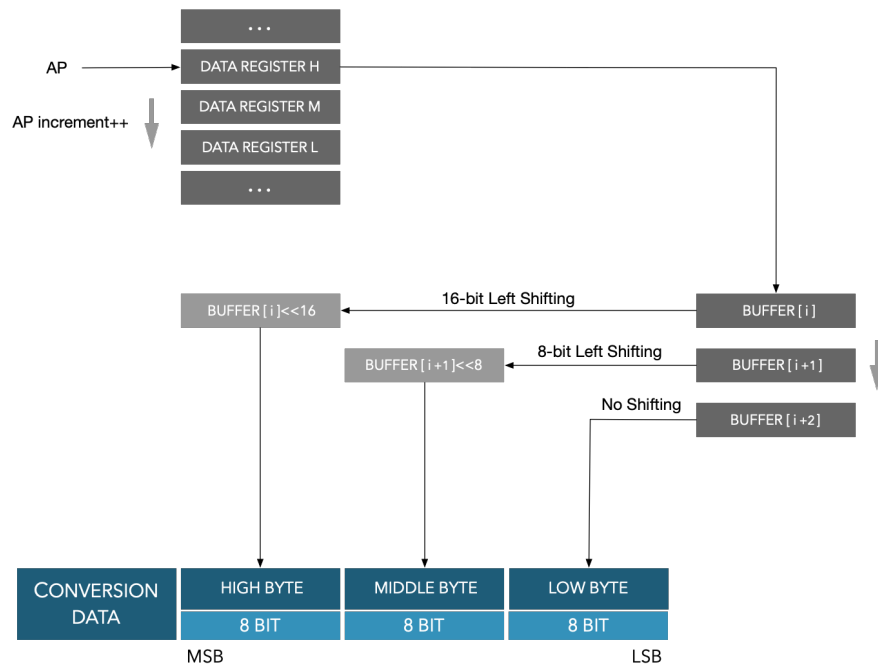


Figure 70: Conversion data reading process.

To get the 24-bit encoded converted data correctly, it is necessary to read sequentially from 3 Data Registers and combine the stored values in the order:

1. High byte
2. Middle byte
3. Low byte

as represented in Figure 70 on the facing page. Offset and Gain Registers (AP from 0x0D to 0x12) are 16-bit encoded, so only two bytes must be read sequentially to form the whole value. A summary of all the registers is shown in Table 10.

Register	AP	Dir	Value	Description
Status	0x00	R	8-bit	Status Register
Cap Data H	0x01	R	H byte	Capacitive channel data
Cap Data M	0x02	R	M byte	Capacitive channel data
Cap Data L	0x03	R	L byte	Capacitive channel data
VT Data H	0x04	R	H byte	Voltage channel data
VT Data M	0x05	R	M byte	Voltage channel data
VT Data L	0x06	R	L byte	Voltage channel data
Cap Setup	0x07	R/W	8-bit	Capacitive channel setup
VT Setup	0x08	R/W	8-bit	Voltage channel setup
EXC Setup	0x09	R/W	8-bit	Capacitive channel excitation setup
Configuration	0x0A	R/W	8-bit	Configuration setup
Cap DAC A	0x0B	R/W	8-bit	Capacitive DAC setup
Cap DAC B	0x0C	R/W	8-bit	Capacitive DAC setup
Cap Offset H	0x0D	R/W	H byte	Capacitive offset calibration
Cap Offset L	0x0E	R/W	L byte	Capacitive offset calibration
Cap Gain H	0x0F	R/W	H byte	Capacitive gain calibration
Cap Gain L	0x10	R/W	L byte	Capacitive gain calibration
Volt Gain H	0x11	R/W	H byte	Voltage gain calibration
Volt Gain L	0x12	R/W	L byte	Voltage gain calibration

Table 10: Registers summary.

### 5.7.1 Data Registers

Two data registers store the 24-bit encoded capacitive and voltage channel output data and are updated only once the capacitance and voltage conversions on the capacitive and the voltage channels are completed.

- Capacitive Data Register

Address Pointer: 0x01, 0x02, 0x03

Value encoding: 24-bit

0x000000 code: negative full scale ( $-4.096$  pF)

0x800000 code: zero scale (0 pF)

0xFFFFFFFF code: positive full scale ( $+4.096$  pF)

For the capacitive data register, the full-scale capacitance range of the device is  $\pm 4.096$  pF, that can be approximated to  $\pm 4$  pF.

- Voltage Data Register

Address Pointer: 0x04, 0x05, 0x06

Value encoding: 24-bit

0x000000 code: negative full scale ( $-V_{\text{REF}}$ )

0x800000 code: zero scale (0 V)

0xFFFFFFFF code: positive full scale ( $+V_{\text{REF}}$ )

For the voltage data register, the full-scale voltage can be set by using two approaches based on a different voltage reference:

1. on-chip high precision 1.17 V voltage reference
2. external voltage reference connected to the device's differential reference input pins

By using the second method, the differential voltage reference input pins are set up as follows:

REFIN(+): 3.3 V ESP32 power voltage

REFIN(-): 0 V ground voltage

Subsequent reading of the 3 bytes of each Data Register using the AP auto-increment feature, as shown in Figure 70 on page 92, prevents data loss during continuous conversion.

Part III

---

HUMAN MOTION MONITORING  
APPLICATIONS



## CHAPTER SIX

## 6.1 SIGNAL ACQUISITION AND FILTER STAGE

The routine related to the performed readings is started and the sensing signals can be properly acquired. Moreover, specific code for saving data is written on Processing IDE in order to make real-time storage of the read data. The Processing Environment allows to run programs written in the text editor, applying particular commands on data transmission through the Serial Port, where the serial communication between the microcontroller and the device under test goes on. For this aim, the prepared routine is able to write information in a file, making an electronic archive of the acquired data which can be read later allowing subsequent signal analysis and processing.

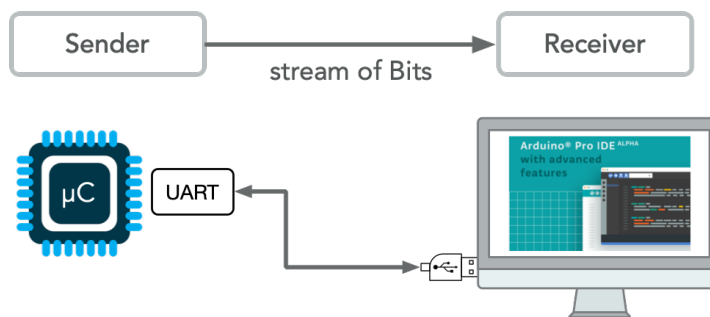


Figure 71: Data transmission from microcontroller to PC.

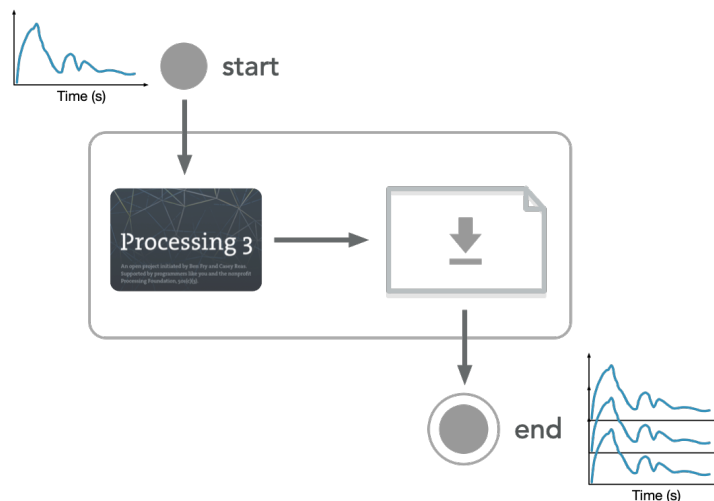


Figure 72: Data storage through self-written Processing program.

Once the electronic circuit is configured, the sample is connected and the signal acquisition can start. The software window opened on the PC plots the signal change over time. The written program saves data to a file while acquisition is on in order to allow next signal processing. An example of complete set-up of the connected sample to the electronic board to perform real-time signal acquisition, is shown in Figure 73.

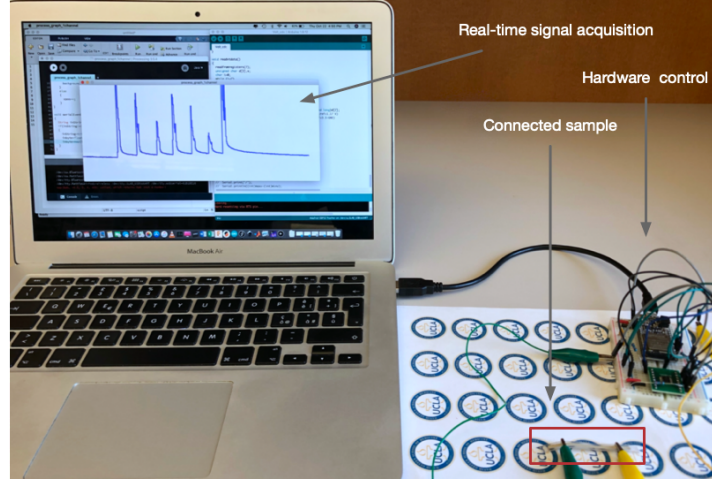


Figure 73: Connection set-up for real-time signal acquisition.

Since dynamic systems can be affected by large signal variations, adding a filtering stage of signal processing can be useful to easily analyze the acquired signals. Noisy signals are sent as input to a digital filter providing smoothed signals as output. For this purpose, Savitzky-Golay filter is implemented by Matlab Signal Processing Toolbox. This filter belongs to digital smoothing polynomial filters, which are typically used to smooth out noisy signals whose frequency span without noise is large. It is used to reduce high frequency noise of the signals due to its smoothing properties. The algorithm is based on minimizing the least-squares error in fitting a polynomial to frames of noisy data.

The filtering process consists of replacing each point of the signal by some combination of the signal values contained in a moving window centered at the point, on the assumption that nearby points measure nearly the same underlying value. In the case of moving average filters, each data point is replaced with the local average of the surrounding data points. In particular, taking  $k$  points to the left and  $k$  points to the right of the data point  $x_s$  corresponding to the window length  $L = 2k + 1$ , the filter gives the output value

$$\hat{x}_s = \frac{1}{L} \sum_{r=-k}^k x_{s+r} \quad (66)$$

which replaces the considered data point.

The  $n$ th-order local polynomial is used to fit the set of input samples included in the frame length by least-squares approximation, taking the calculated central point of the fitted polynomial curve as the new smoothed data point.

The Savitzky-Golay finite impulse response (FIR) smoothing filter can be implemented by setting the filter parameters related to the desired polynomial order and frame length as described in Table 11

Input Arguments	
<code>x</code>	Input signal
<code>order</code>	Polynomial order, specified as a positive integer; it must be smaller than the frame length.
<code>framelen</code>	Frame length, specified as a positive odd integer.
Output Arguments	
<code>y</code>	Filtered signal

Table 11: Filter arguments.

The two parameters must be set according to the input signal. In particular, the smoothing effect due to the averaging obviously increases with increasing frame length but could lead to a strong signal distortion, evident as reduction in the amplitude of the processed signal as also happens when the polynomial order increases.

Then, the designed filter can be applied to the input signal by the following command

```
y = sgolayfilt(x, order, framelen);
```

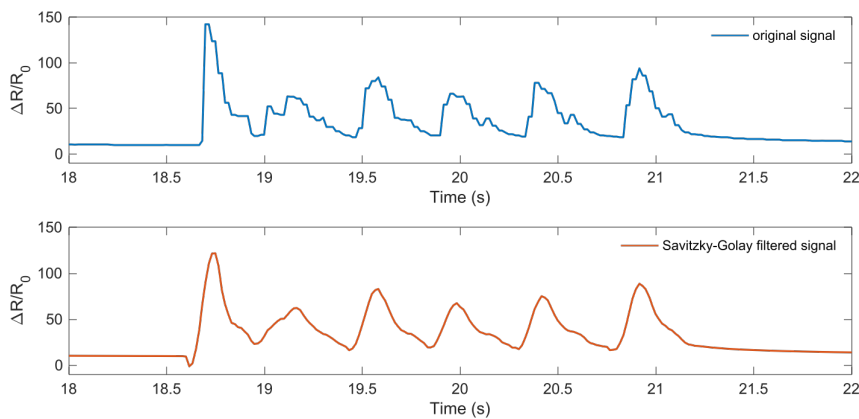
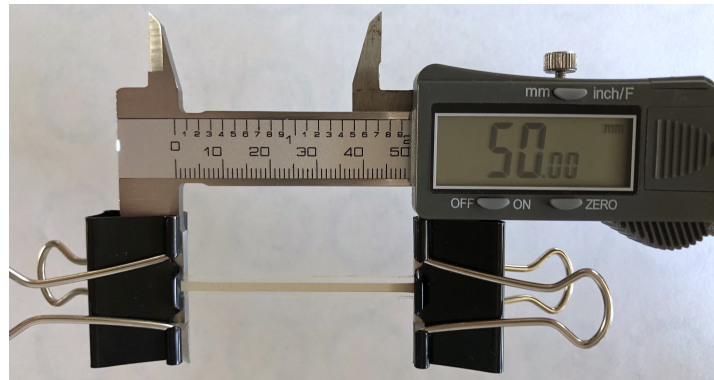


Figure 74: Example of original signal filtered by Savitzky-Golay filter with  $\text{order} = 3$  and  $\text{framelen} = 11$ .

## 6.2 ELECTROMECHANICAL PERFORMANCE

The resistance change  $\Delta R$  represents the change under states of deformation, while the  $R_0$  value is the base resistance (or initial resistance) related to absence of deformation, according to a completely unloaded state. The increasing in relative change resistance  $\Delta R/R_0$  is attributed to the conductive network change in the samples. This means strain sensitivity of the composite-based strain sensors is connected to the change in distance between the silver particles within the PDMS matrix: during the stretching process, the distance between particles increases and causes damage of the conductive network, thereby increasing the resistance.



(a) Initial state.

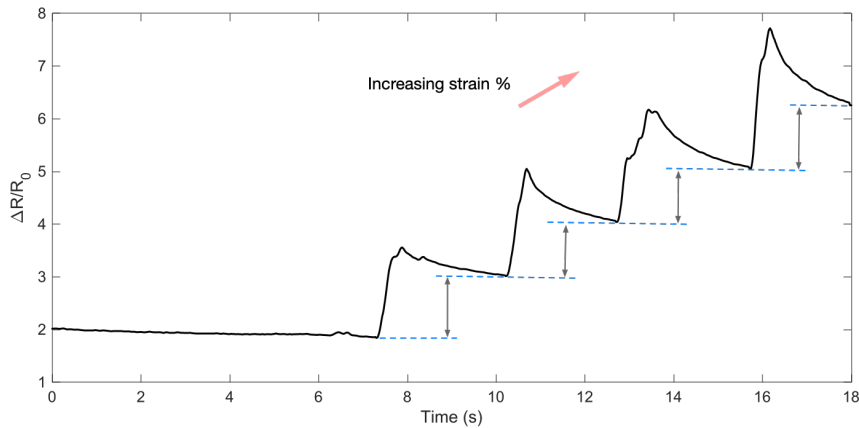


(b) Final state.

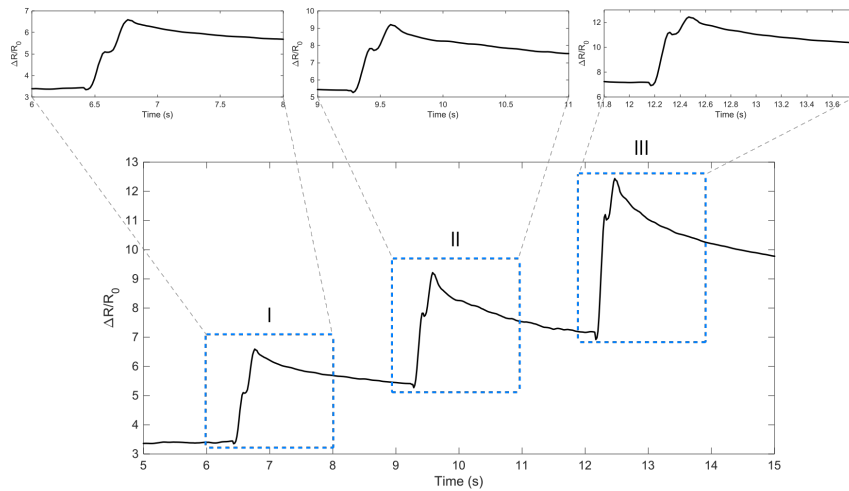
Figure 75: Strain of 20% applied on the fixed sample.

The samples are fixed at both ends on a digital caliper to analyze the performance in terms of strain sensing at different percentages of applied strain. It allows to give a controlled elongation to the fixed sample, while acquiring the electromechanical response. Figure 75 shows the simple set up to give elongation to the sample.

A stretching test is performed to analyze the sensing behavior of the fixed sample when different percentages of strain are induced by undergoing different elongation values. The initial condition corresponds to the fixed sample on the digital caliper with a low induced strain, as observed from the starting relative resistance change of 2. The plot related to the increasing strain test is reported in Figure 76a. A second test is also performed by giving larger elongation at each step. The plot reported in Figure 76b shows three consecutive steps related to subsequent elongations given starting from the previous value. The three insets of the magnified plot allow to better observe and compare the transitions.



(a) Response to increasing strain levels.

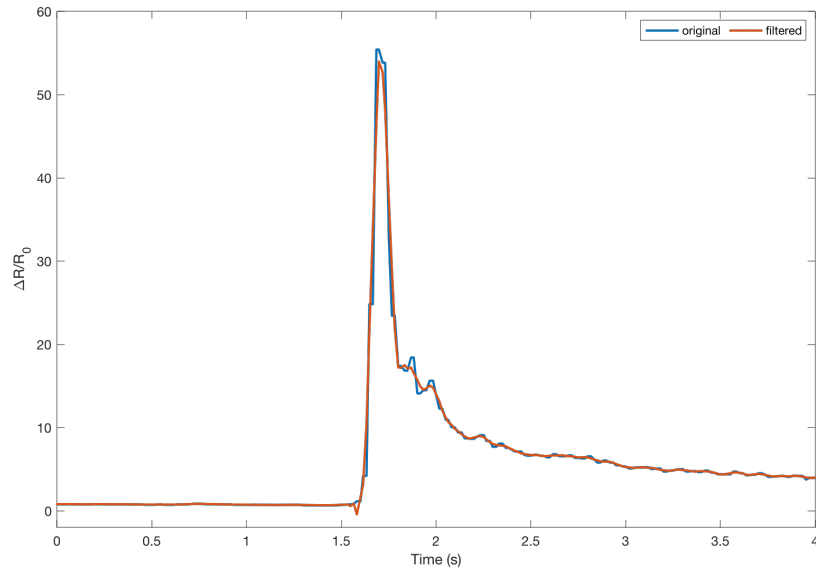


(b) Response to larger increasing strain levels.

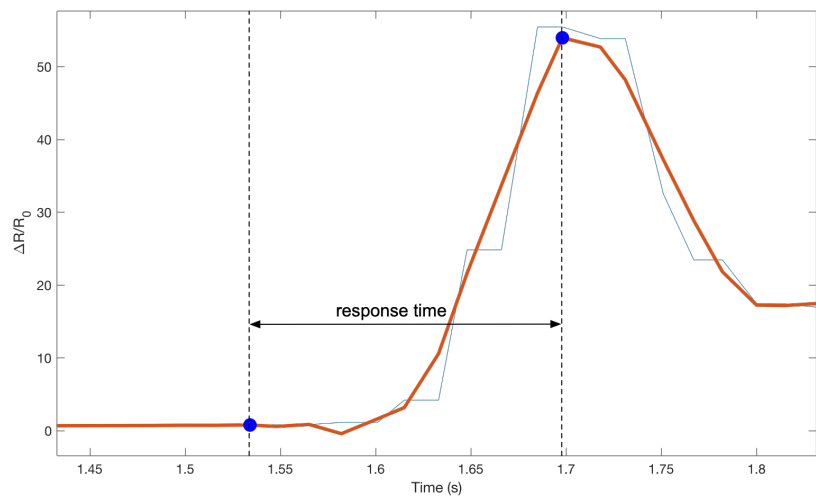
Figure 76: Examples of increasing strain tests.

In order to estimate the response time of the sensing mechanism, the tested sample undergoes a strain pulse performed by stretching the two ends of the sample. Figure 77a shows graphically the acquired impulse signal by both original and filtered signals overlapped.

The plot in Figure 77b reports the enlarged time interval in which the sudden transition from relaxed to stretched condition occurs.



(a) Impulse signal.



(b) Time difference between the two fixed points.

Figure 77: Example of response time evaluation.

The response time can be then estimated by the time difference between the two time instants indicating the start and end time of the growing curve, as shown by the circle markers. The two considered points, marked on the filtered signal, correspond to

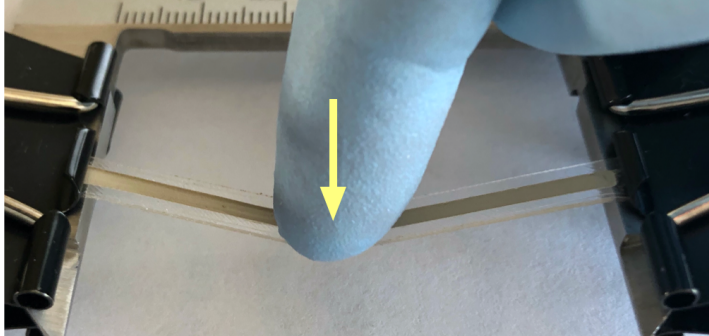
start position  $t_0 = 1.534 \text{ s}$

end position  $t_1 = 1.698 \text{ s}$

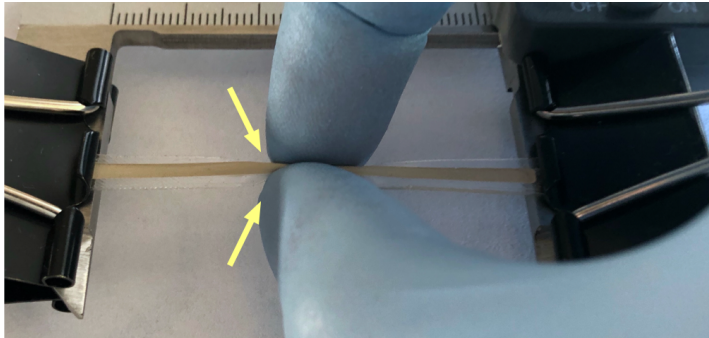
time difference  $\Delta t = t_1 - t_0 = 0.164 \text{ s} = 164 \text{ ms}$

That suggests a system response time of the order of a few hundreds milliseconds.

To analyze the feature of strain sensing, the first tests are based on applications of different states. The tested sample is clipped on both ends while these tests are performed. Figure 78 shows the states of pressing and pinching applied on the fixed sample. The pressing test is performed by applying pressure with finger in the middle of the sample, whereas the sample is squeeze with fingers during the pinching test.



(a) Pressing state.



(b) Pinching state.

Figure 78: Fixed sample in pressing and pinching states.

The controlled pressing test, shown by the schematic in Figure 79, lasts about 30 s. The cycles are repeated by pressing the sample in the same point of application. The peaks of response due to the applied pressure are distinguishable as well as the peak amplitude indicating the corresponding intensity of stress application. Since the strain induced by pressing leads to the increase in resistance, the higher peaks are related to higher strain, as evident from comparing the amplitude of the last 5 peaks to the others. The characteristic of double peaks, shown in the enlarged inset, indicates that second peaks follows the first because of the releasing state which restores the initial condition inducing to a strain due to the elastic property of the material. Therefore, two events of increase in resistance occur subsequently: the first increase in resistance due to the pressing process, the second due to the releasing process.

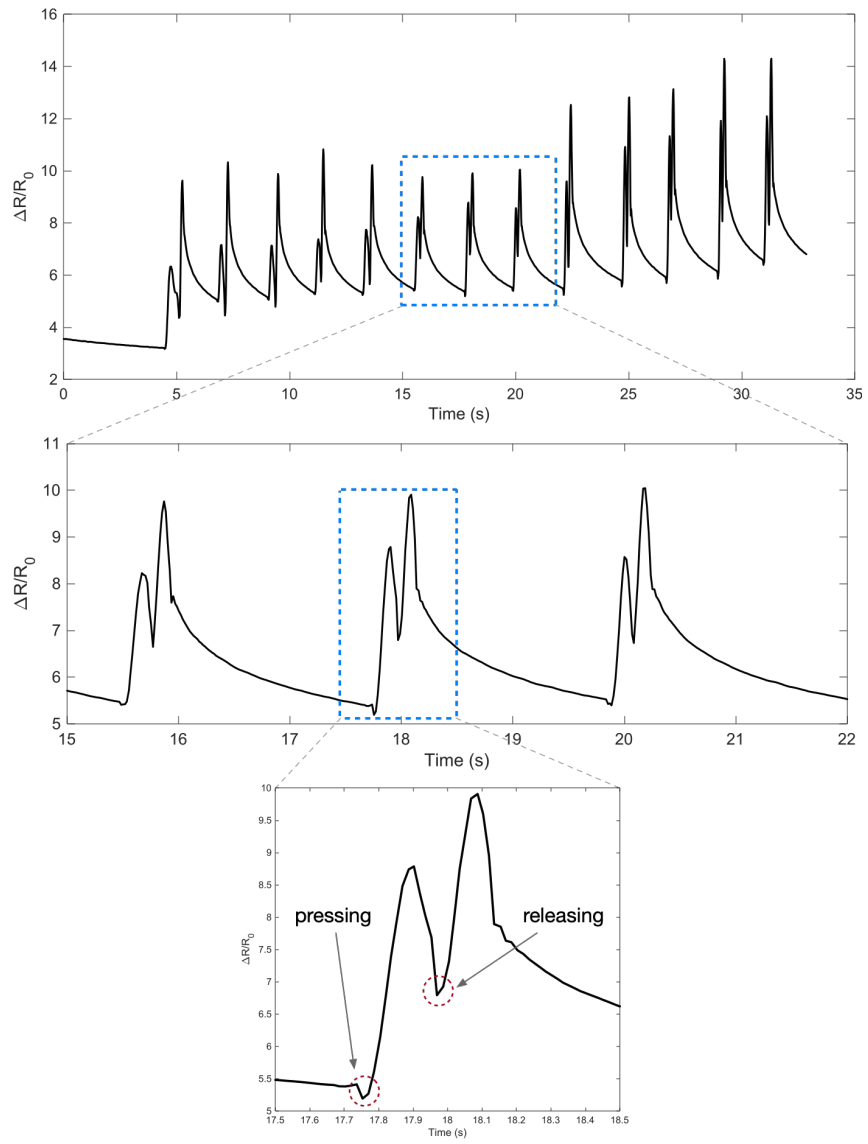


Figure 79: Slow pressing test.

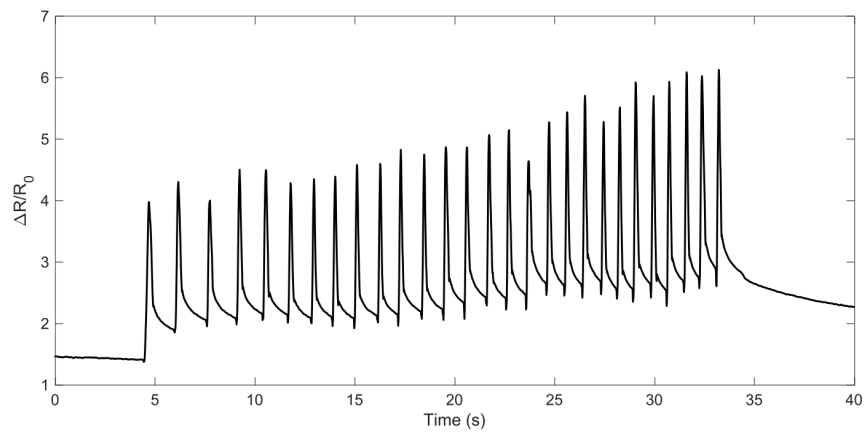


Figure 80: Fast pressing test.

Figure 80 reveals the response of the tested sample at fast pressing test with a duration of  $\approx 30$  s. During this test, the time related to the releasing process decreases as a consequence of the fast pressing repetitions, as evident from the presence of single peaks of response. The pinching test is performed by repeating the same action of stress 5 time consecutively. The resistance suddenly increases during the every pinching action, as shown in the the cycles reported in Figure 81. A holding phase is performed between the two blocks of repetitions, during that the sample is maintained pinched.

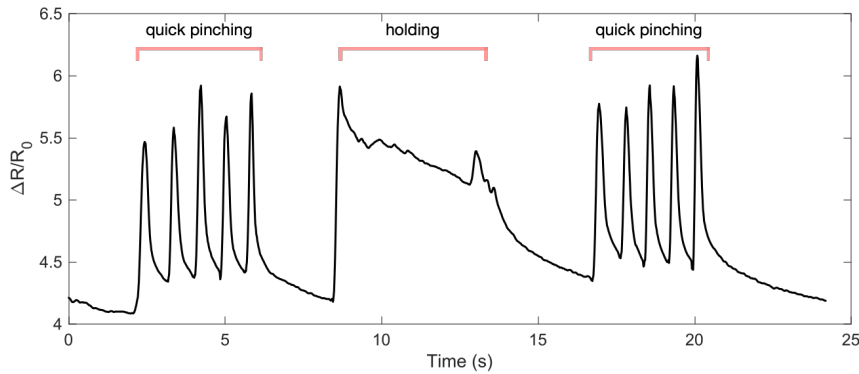


Figure 81: Pinching test.

### 6.3 HUMAN MOTION MONITORING

In order to prove the applicability of the developed strain sensors as wearable electronic devices for human activity monitoring, the samples are applied different parts of human body performing specific kind of tests. The strain sensors result highly stretchable and can be fixed onto clothing or directly mounted onto human skin to measure the body strain. Moreover, this type of strain sensors could be suitable for soft robots monitoring applications. The performed tests of strain sensing focus on detecting large range human motion, such as the bending movements of the body joints. In particular, the sensors are directly applied to the operator's skin by the aid of adhesive patches and demonstrate ability to detect the strain induced by the body joints movements.

In order to perform real-time human body motion detection, the strain sensors are tested in various configurations. A first example, reported in the following, concerns applications on the ankle joint. The test is performed while standing and moving the body's center of gravity forward. The induced ankle joint movement in the sagittal plane supports the maintenance of balance, leading the strain sensor to a compression state, as evident in the succession of peaks that reflect the repetition of the movement. In particular, three groups of cycles are performed by increasing the frequency of the movement, as shown in Figure 82.

The three groups of 10 consecutive movements are repeated by changing the speed of the joint movement. It can therefore be interpreted as a change in frequency of movement:

- cycles 1st group:  $\Delta t = 15 \text{ s}$   $f \approx 0.7 \text{ Hz}$
- cycles 2nd group:  $\Delta t = 9.5 \text{ s}$   $f \approx 1 \text{ Hz}$
- cycles 3rd group:  $\Delta t = 7 \text{ s}$   $f \approx 1.4 \text{ Hz}$

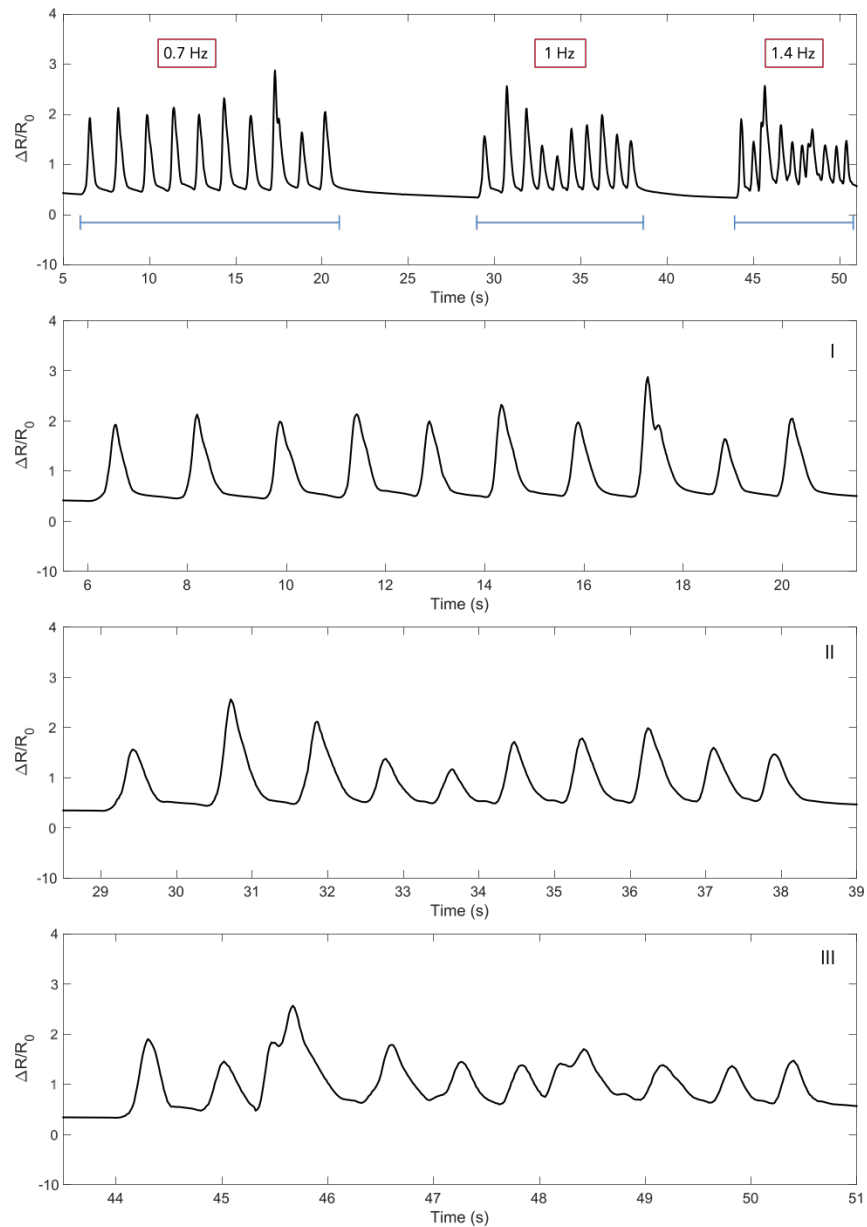


Figure 82: Cycles of motion of the ankle joint at different frequency values.

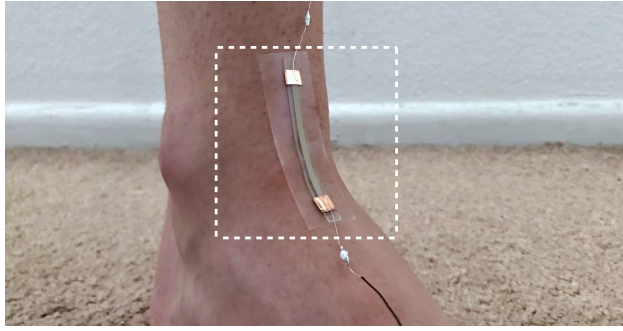


Figure 83: Strain sensor placed on the ankle joint.

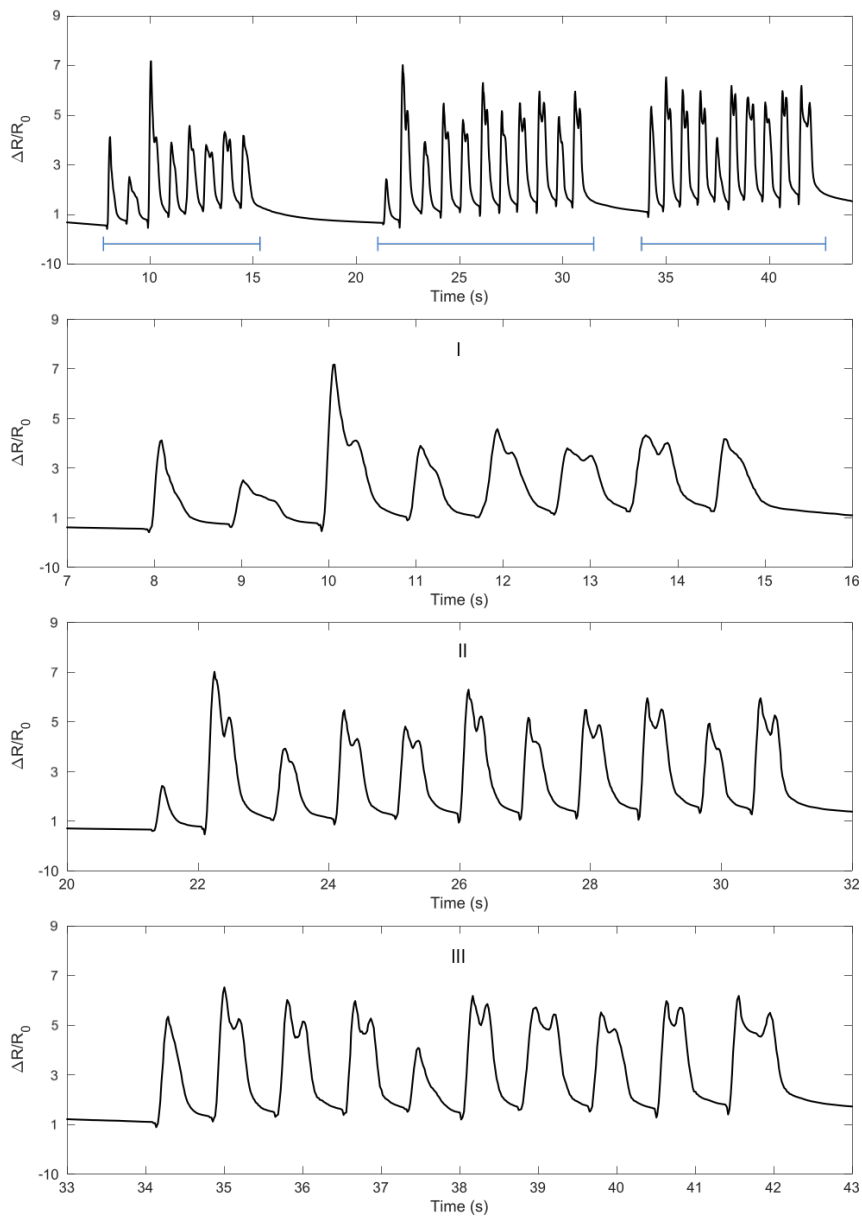


Figure 84: Cycles of motion of the ankle joint by moving the foot upwards.

Figure 83 shows the sensor correctly attached to the ankle joint for testing. A further test is performed by moving the foot upward. The movement induces intense compression on the sensor placed on the ankle joint, as evident from the height of the peaks in Figure 84. Also in this case, three groups of cycles of the same movement are repeated, letting a few seconds of non-movement pass between each of them.

The strain sensor is also used to detect the flexion movement of the wrist joint. To perform the following tests, the sensor is attached to the joint in full extension, as shown in Figure 85a. An example of flexion movement is shown in Figure 85a.

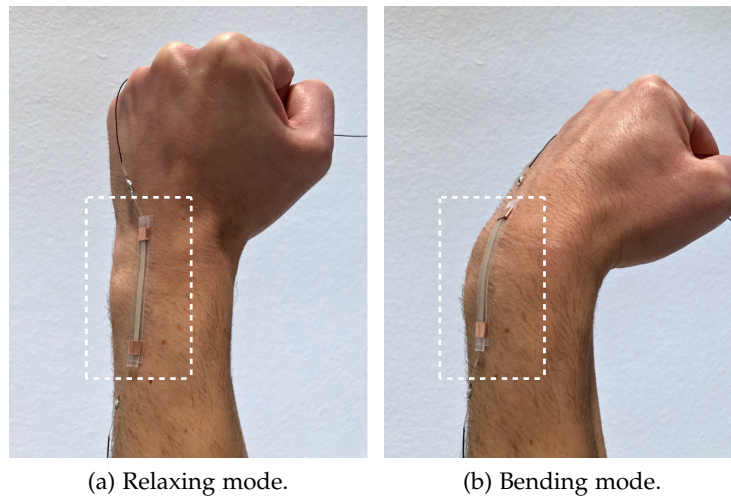


Figure 85: Strain sensor placed on the wrist joint.

The first test, shown in Figure 86, is based on repeating rapid bending movements starting from the unbending position. In particular, three events characterized by a different frequency of movement can be distinguished. The amplitude of the peaks are related to the speed of the performed movements. The presence of secondary peaks is clearly visible by increasing the frequency of movement. This is due to the release effect which creates a strain state in the sensor. Therefore, also the release phase immediately following the bending peak, induces the relative resistance change of the sensor to increase, as can be seen from the last inset, related to the highest frequency.

The three groups of 5 consecutive movements are repeated by changing the frequency of the joint movement as follows:

- cycles 1st group:  $\Delta t = 14 \text{ s}$   $f \approx 0.35 \text{ Hz}$
- cycles 2nd group:  $\Delta t = 7 \text{ s}$   $f \approx 0.7 \text{ Hz}$
- cycles 3rd group:  $\Delta t = 5 \text{ s}$   $f \approx 1 \text{ Hz}$

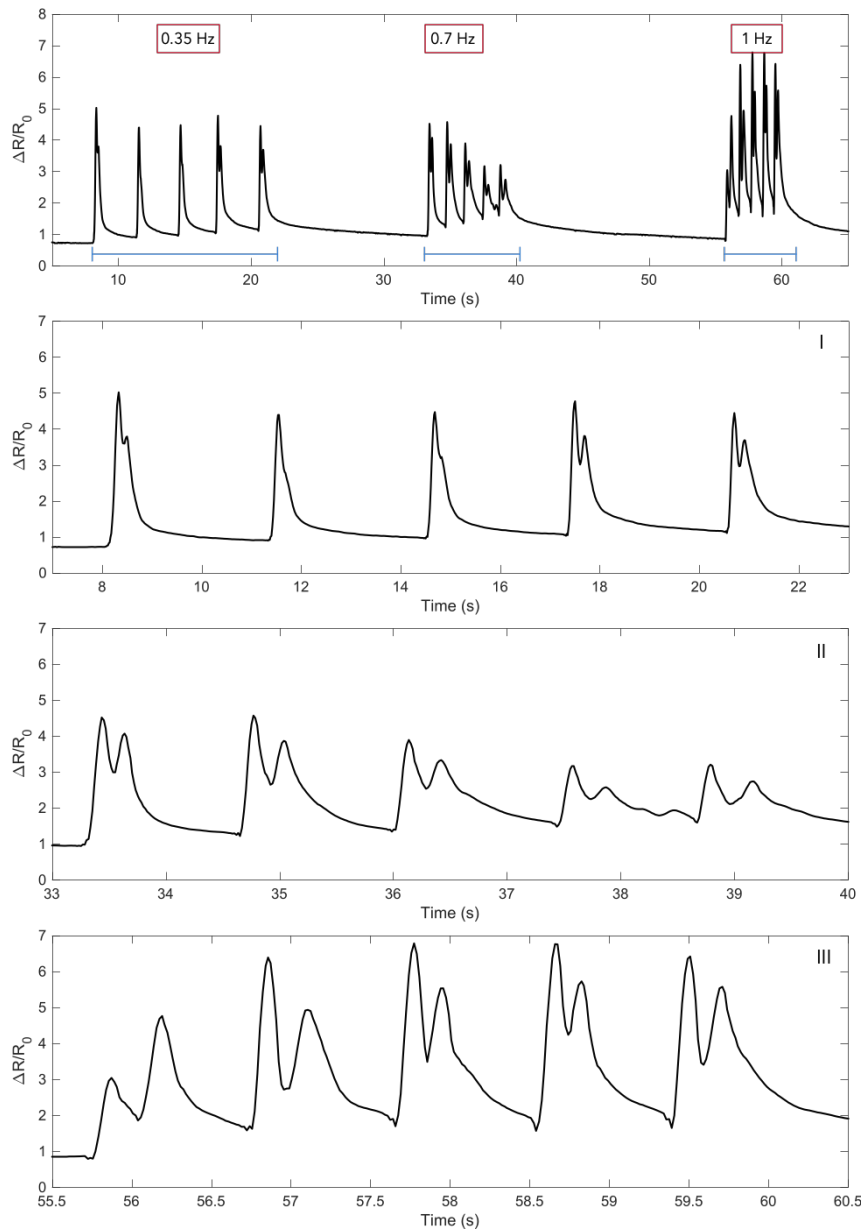


Figure 86: Quick bending cycles of the wrist joint at different frequencies.

The second test is performed by bending the joint starting from the relaxing position to the complete flexion, corresponding to a bending angle of  $90^\circ$ . The peaks in Figure 87 indicate the relative resistance change increases suddenly due to the bending movement occurring in less than 1 s. The bending transition related to three cycles can be observed from the enlarged insets, which show the relative resistance change according to the angle change from full extension to  $90^\circ$  of flexion. During this test the joint is held in the flexion state and then slowly released, controlling movement from the flexion position to full extension.

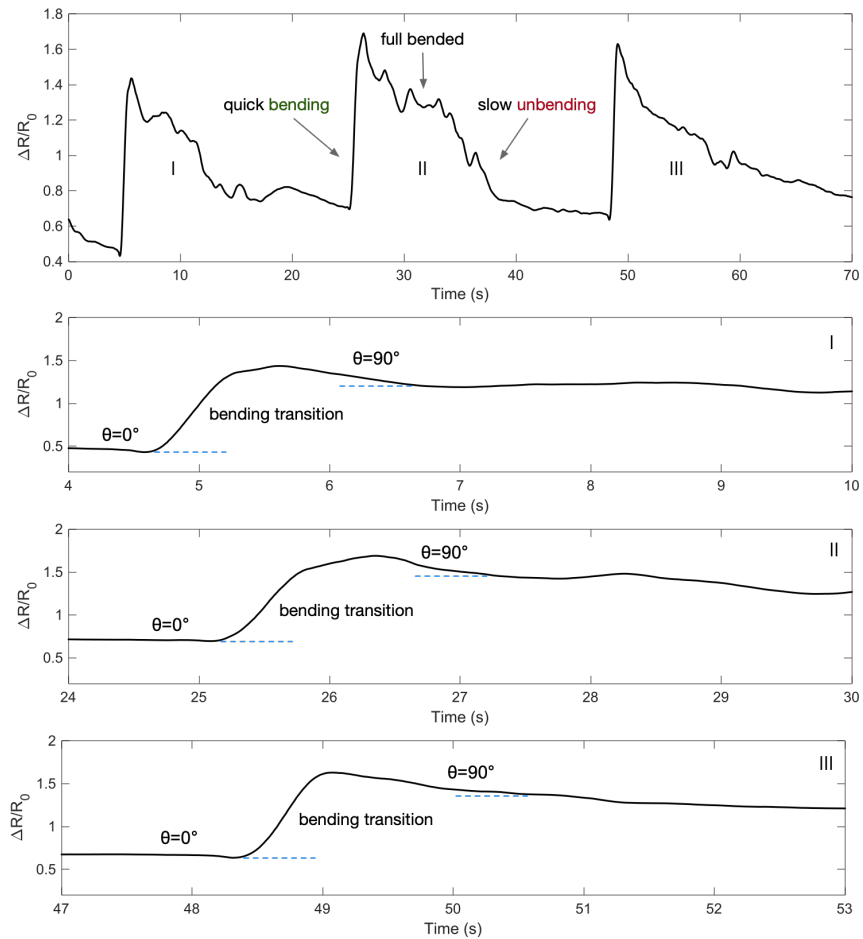
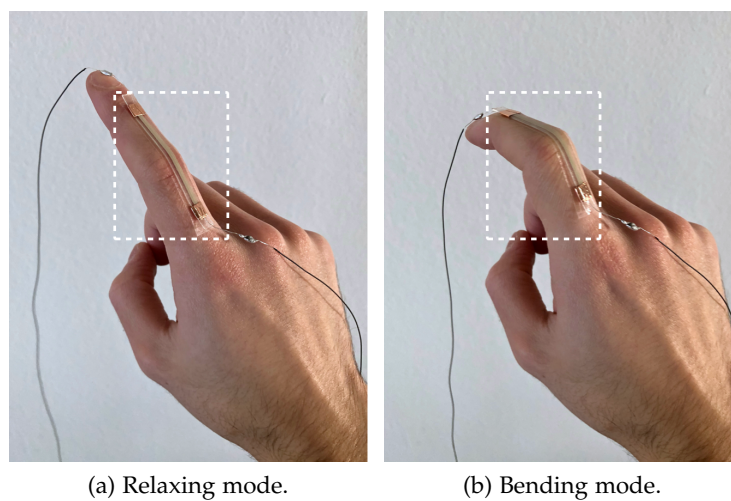


Figure 87: Bending cycles of the wrist joint with controlled unloading phase.

Due to the long shape, the sensors are also suitable for applications on the finger joints. For testing purpose, the sensor is placed on the proximal interphalangeal joint of the forefinger, as shown in Figure 88.



(a) Relaxing mode.

(b) Bending mode.

Figure 88: Strain sensor placed on the proximal interphalangeal joint.

The first test is based on the repetition of three full bending-unbending cycles of the finger joint. As shown in Figure 89, since the movement is performed by bending slowly the finger joint, the relative resistance change increases gradually according to the bending angle starting from the full extension position of  $0^\circ$  to the flexion position of  $90^\circ$ . Once the peak of flexion is achieved, the release phase follows with a second increase in response due to the strain induced by the compression state that occurs when the starting position is restored.

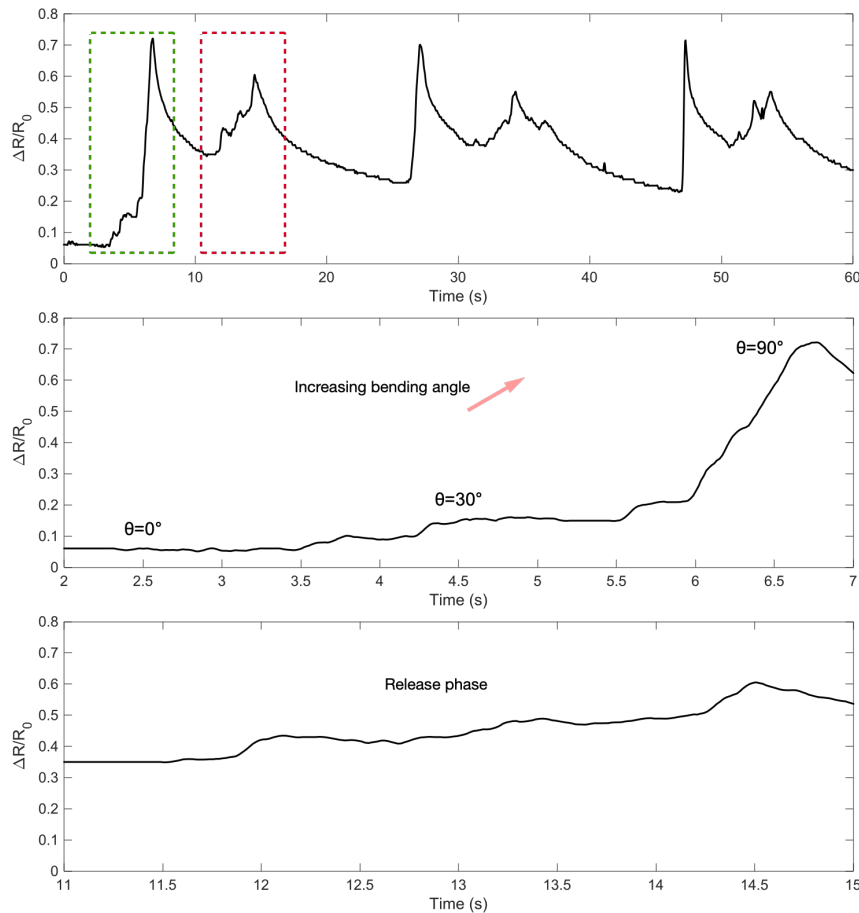


Figure 89: Full bending-unbending cycles of the interphalangeal joint.

The plot reported in Figure 90 is related to quick bending movements repeated 5 times in the same way, letting about the same amount of time pass between one movement and the next. It is noted the high speed of the movements leads to a higher electromechanical response. The enlarged insets reported below the main graph allow to compare the peaks related to the performed movements.

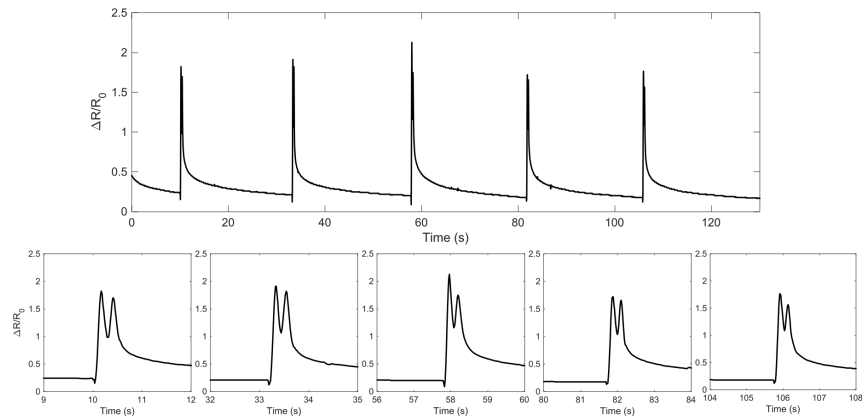


Figure 90: Quick bending-unbending cycles of the interphalangeal joint.

The performed test shown in Figure 91 demonstrates the sensor's ability to modulate the electromechanical response to the applied strain. It means the tested strain sensors show good sensitivity to change the response when movements are performed by changing the speed of the bending cycles. This significant feature is completely reflected on the amplitude of the relative resistance change peaks.

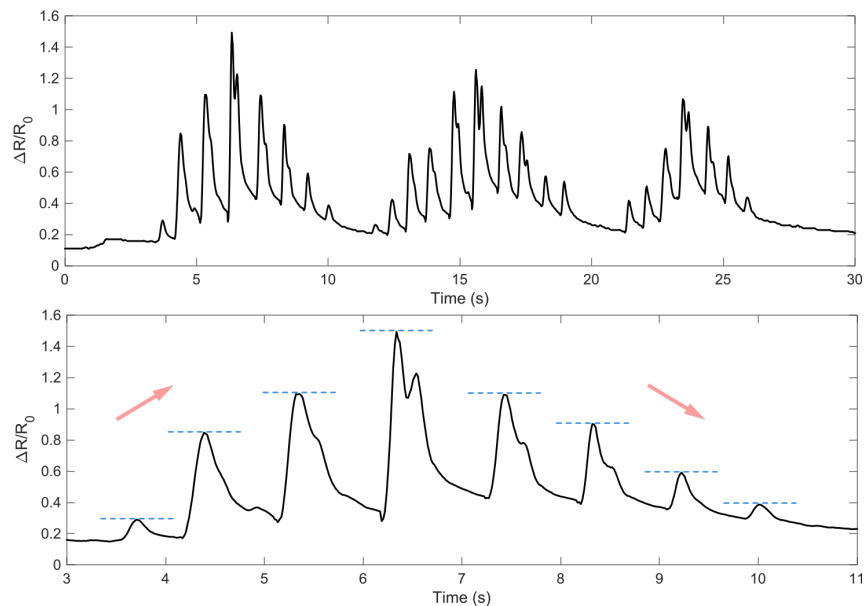


Figure 91: Finger bending.

The strain sensors can provide response also while undergoing fast vibration states, as shown in Figure 92. This further test proves the good sensitivity of the sensors, which means the response change follows optimally the rapid change in the strain state. The reproducibility of the response to very similar fast input changes can be also confirmed by this example.

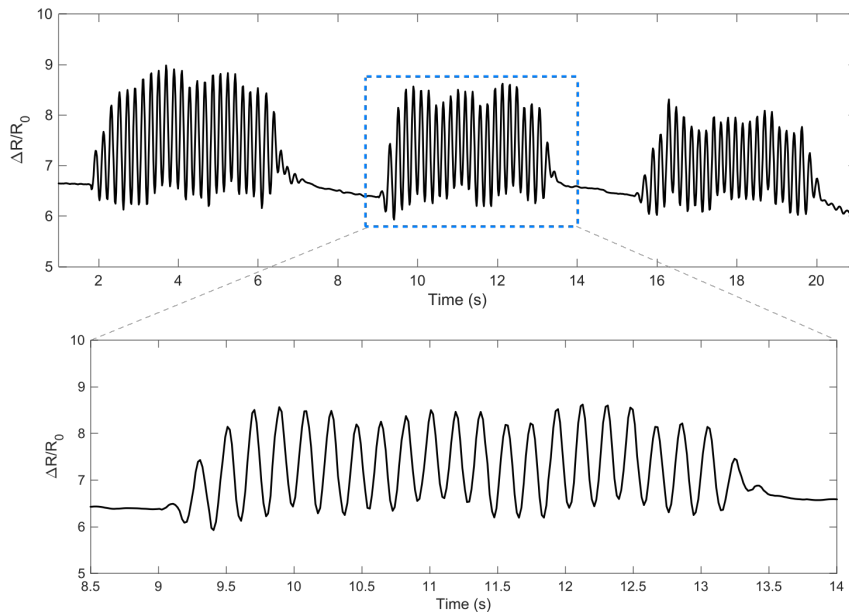


Figure 92: Vibration test of the interphalangeal joint.

Significant applications are also carried out by testing the strain sensors on the knee joint. The two opposite states of the joint, with the sensor properly attached above, are shown in Figure 93.

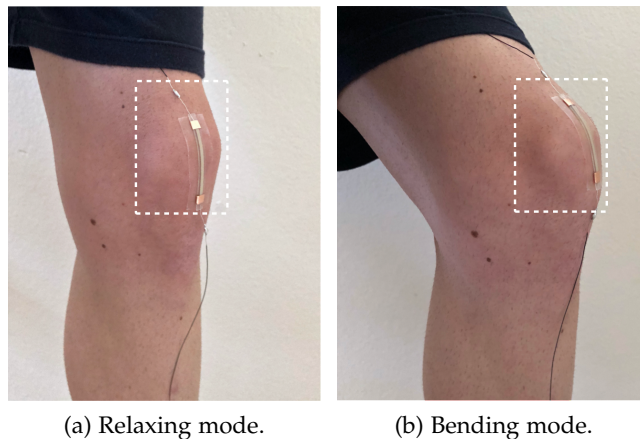


Figure 93: Strain sensor placed on the knee joint.

The first movement is performed by starting from the initial position that corresponds to full extension of  $180^\circ$  without considering the hyperextension angles, according to the standing position. The full motion is then performed by achieving the sitting position which leads to a flexion state of  $90^\circ$ . The sequence of 5 cycles of double movement can be observed in Figure 94. Furthermore, the same test is repeated by performing the second phase slowly, as confirmed by the lower secondary peak heights in Figure 95.

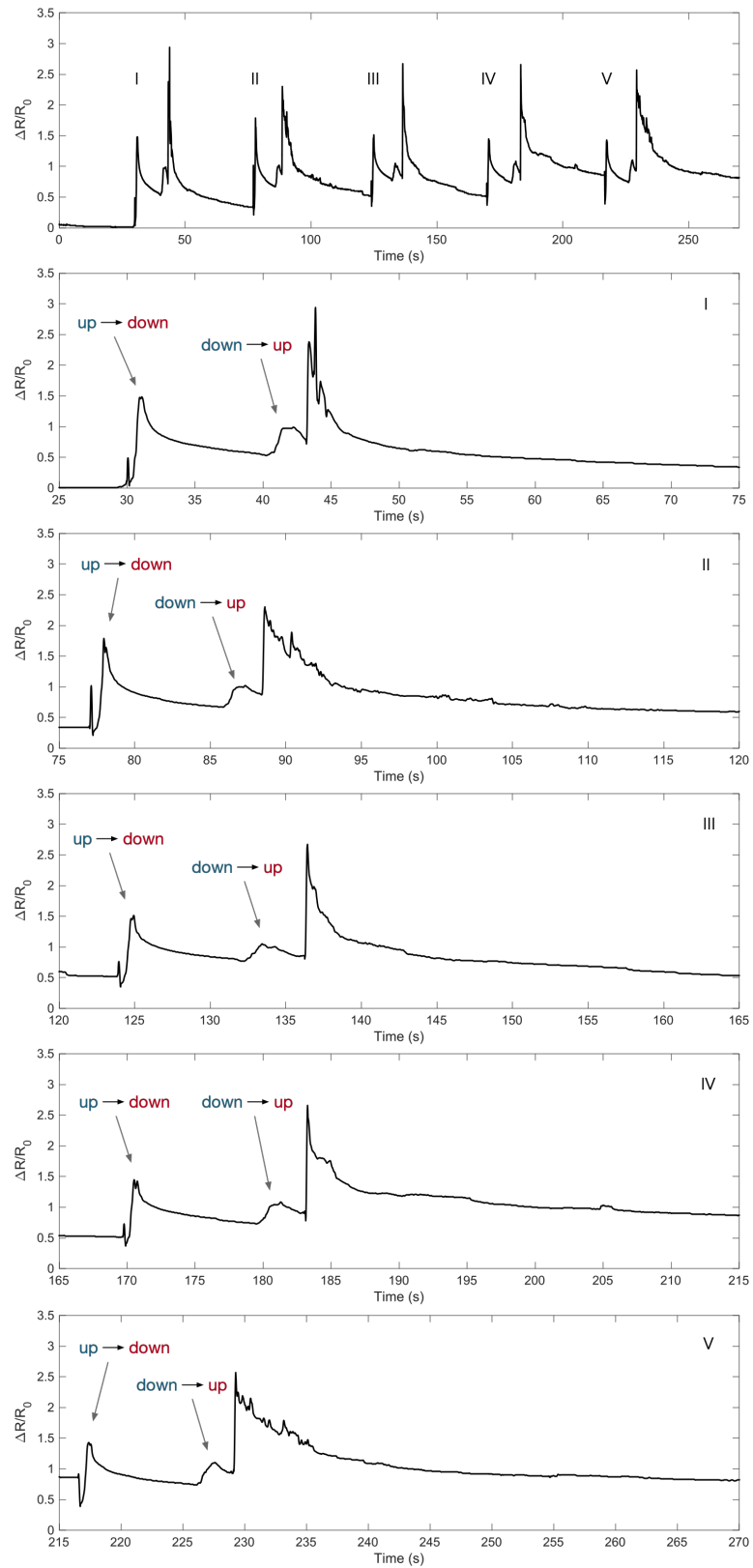


Figure 94: Full up-down cycles of the knee joint.

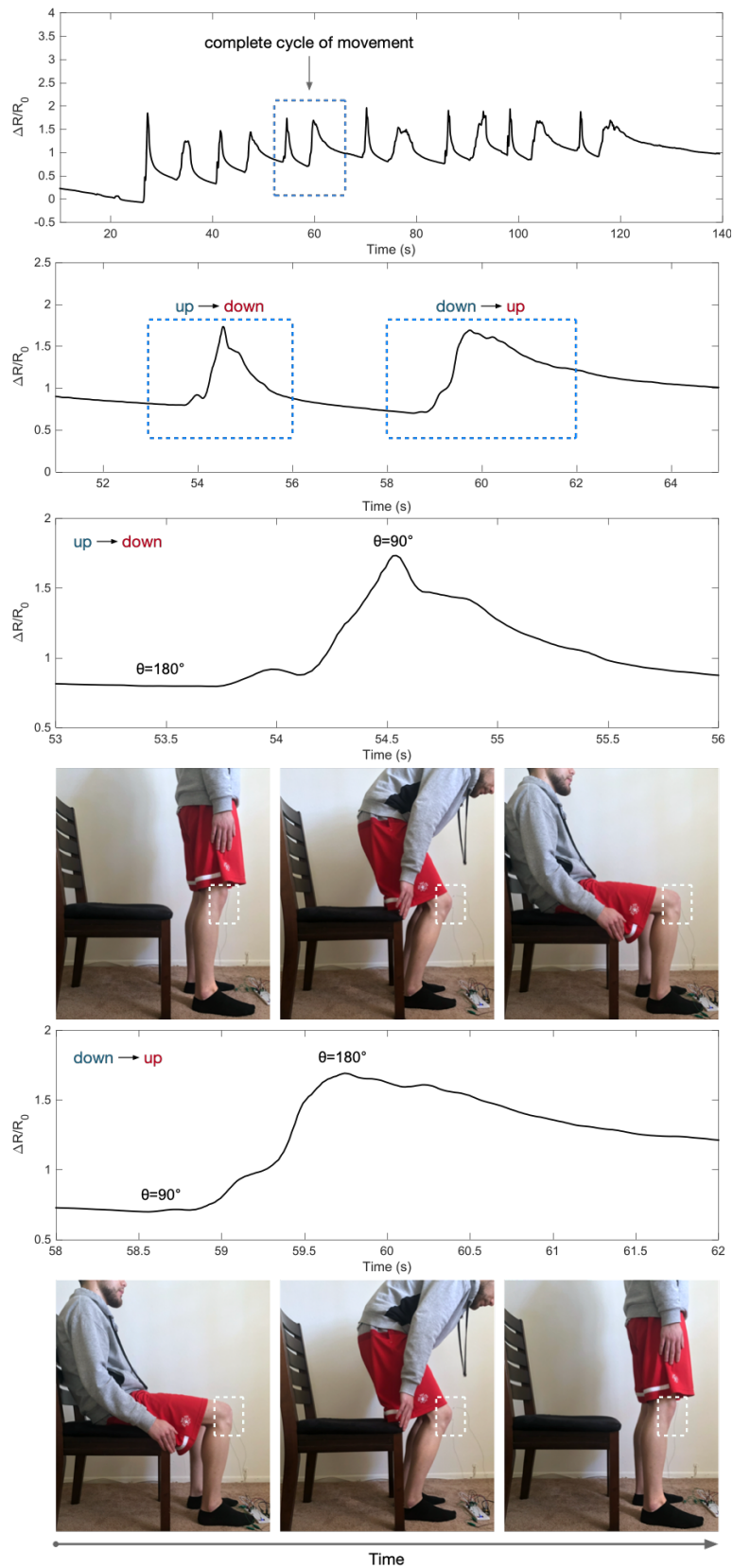


Figure 95: Full up-down cycles of the knee joint with controlled release phase.

As predicted by the piezoresistive effect, the resistance change of the strain sensors increases during stretching and decreases during the releasing process. A rapid strain state causes a lack of contact between particles and hence so that the conduction pathways become weak. For this reason, a damage and a subsequent reconstruction of the conductive network takes place network during each stretching/releasing cycle. Another evident feature of the response signal is the presence of secondary peaks. The generation of these shoulder peaks is attributed to the behavior of the network damage that opposes the reconstruction of the network during the recovery process.

The value of the system response time depends on the viscoelastic behavior of the polymeric material. Indeed, the presence of energy dissipation mechanisms distances the system from the ideal elastic response, which means the sensors are characterized by a behavior that is not completely linear in terms of response to mechanical stimuli. According to this consideration, the sensor behavior can be assumed as a first-order system and consequently the system response can be described using a first order differential equation.

Since the range of strain for the performed applications in human motion monitoring is limited to a maximum of  $\approx 30\text{-}50\%$ , it is observed the strain sensors show a good response in terms of sensitivity below that limit. The strain sensors exhibit high flexibility and stretchability ( $\varepsilon > 50\%$ ), keeping to correctly work also during stretching states last for many consecutive stretching/releasing cycles. The stretchability property of the samples is demonstrated by performing a break test, in order to obtain indication of the maximum elongation value for which the break of the sample occurs. The test is carried out by fixing the sample on the digital caliper and inducing elongation manually, starting from the relaxing state according to the value displayed on the digital screen of 50.25 mm. The elongation is provided gradually up to a value of  $\approx 83$  mm for which the sample begins to induce mechanical resistance to the elongation movement. Continuing with the elongation, the breaking point is then observed for a displayed length of 89.45 mm. As an immediate result, the maximum strain value related to the described test is equal to  $\approx 78\%$ , corresponding to the limit of percentage strain the sample under test can withstand.

In terms of electrical performance, the electrical conductivity of the composites estimated by electrical characterization show values up to an order of magnitude of  $10^3 \text{ S cm}^{-1}$  corresponding to a resistivity in the order of  $10^{-5} \Omega \text{ m}$ . A further characterization in terms of response to different strain values can provide estimate of the linear relationship between the resistance change and the strain. For this purpose, the linear fitting is performed from the resistance change values acquired for increasing strain values as shown in Figure 96.

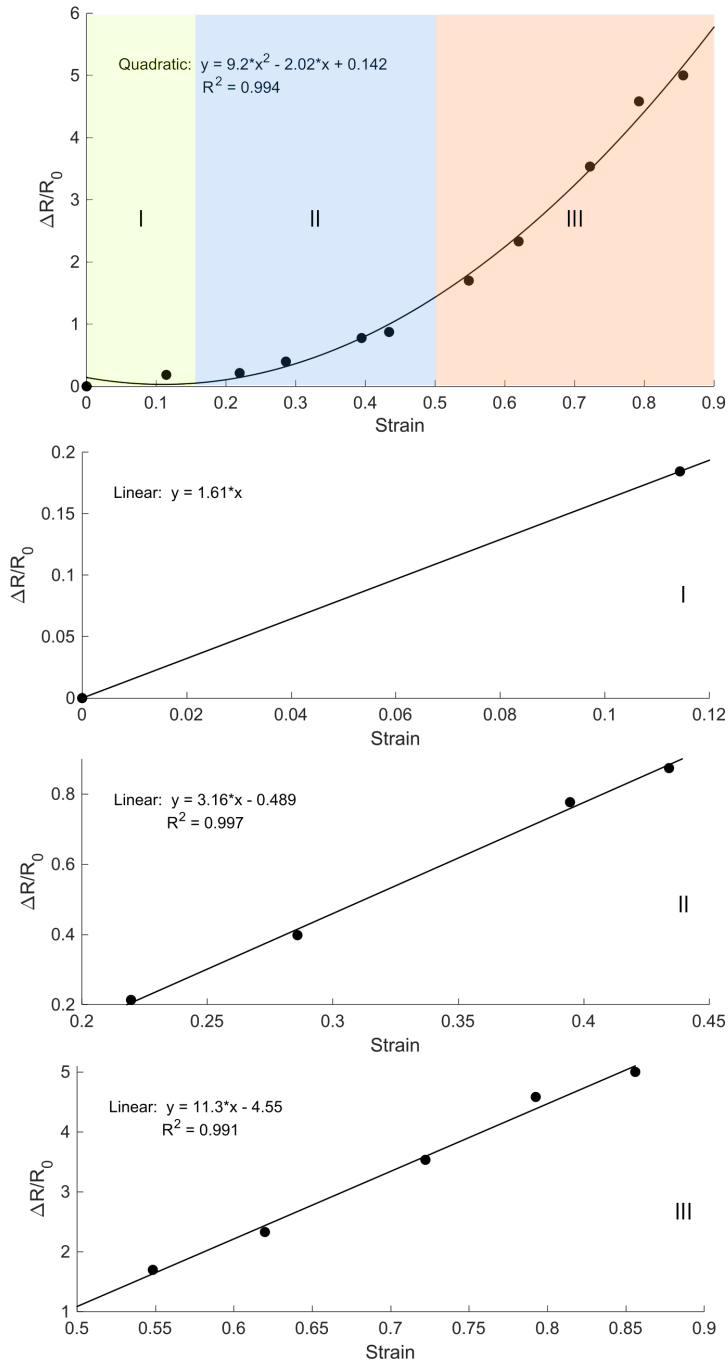


Figure 96: Representative strain-resistance change curve.

The experimental data used to estimate the relationship between the resistance change and the strain are related to an initial sample length of 17.5 mm and a strain range of 0-86%. The percentage of maximum deviations between the curve and the fitting line represents the linearity. The slope of the strain-resistance curve is defined as the strain gauge factor  $GF = (\Delta R/R_0)/\epsilon$ , reflecting the strain sensitivity. The greater the GF of the sensor, the easier it detects small deformations.

As shown in the main plot, three regions of linearity can be identified, characterized by a different GF value: as observed by the slope of the curves, the sensitivity, i. e. GF, increases with increasing strain.

#### 6.4 DEVELOPMENTS IN STRETCHABLE ELECTRONICS

Human body monitoring processes should exhibit sufficient stretchability for high strain and good sensitivity for small strain as well. The polymer-based strain sensors base on two main components, which are the polymer and conductive parts. The adopted design is based on composite-based method to create the sensing structure and then to allow the strain sensing ability. The non-conductive polymer component offers large support to the applied strain states, while the conductive fillers create a continuous conduction network, providing a reliable electrical response for sensing strain.

Since the developed samples are electrically characterized by extremely low resistance values due to high conductivity of the composite material, they can be considered as reliable conductors. Therefore, the developed samples have potential applications in stretchable conductors, owing to their excellent performance in terms of stretchability and electrical conductivity. This means the conductive composite can be used to draw precise pattern on soft polymeric substrates creating stretchable electrical circuits connecting sensors. Using this design, no external wires connection is needed. The required hardware electronics, such as electronic chips for signal reading and conversion, can be easily integrated into the stretchable structure due to their reduced size.

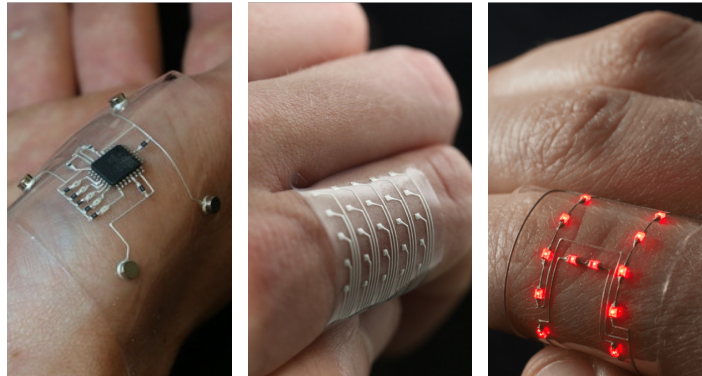


Figure 97: Examples of innovative soft electronics.

According to these considerations, further studies can be performed in the development of methods for fabricating stretchable electrodes from conductive composites that can be integrated into stretchable electronic devices, providing high stretchability and electrical conductivity simultaneously.

Part IV

---

APPENDIX





## SOFTWARE ROUTINES

---

### A.1 PROCESSING SCRIPT

---

```
import java.util.*;
import java.text.*;
import processing.serial.*;

4  PrintWriter output;
   DateFormat fnameFormat= new SimpleDateFormat("file");
   DateFormat millisFormat = new SimpleDateFormat("ss.SSS");
   Serial myPort;
9  String fileName;
   char HEADER = 'H';
   float[] val=new float[1];
   int xpos=1;
   float inbyte=0;
14 int lastxpos=1;
   int lastheight=0;

   void setup()
   {
19 size(1440,600); //window size
   String portName = Serial.list()[3];
   println(Serial.list());
   println("Connecting" + Serial.list()[3]);
   myPort = new Serial(this, portName, 115200);
24 Date now = new Date();
   fileName = fnameFormat.format(now);
   output = createWriter(fileName + ".txt");
   myPort.clear();
   myPort.bufferUntil('n');
29 background(255);
   }
   //...
```

---

---

```

//...
void draw()
{
4  output.println();
   String timeString = millisFormat.format(new Date());
   output.print(timeString);
   output.print('/');
   for(int i=0;i<1;i++)
9   output.print(val[i]);
   stroke(1,34,255); //line color
   strokeWeight(4); //line width
   line(xpos,lastheight,xpos,height-inbyte);
   lastxpos=xpos;
14  lastheight=int(height-inbyte);
   if(xpos>=width)
   {
     xpos=0;
     lastxpos=0;
19  background(255);
   }
   else
     xpos++;
   }
24
void keyPressed()
{
   output.flush();
   output.close();
29  exit();
   }

void serialEvent(Serial myport)
{
34  String inString=myport.readStringUntil('\n');
   if(inString!=null)
   {
     inString=trim(inString);
     float incomingval[]=float(split(inString,"\t"));
39  if(incomingval.length<=1 && incomingval.length>0)
     {
       for(int i=0;i<incomingval.length;i++)
         val[i]=incomingval[i];
     }
44  inbyte=float(inString);
     inbyte=map(inbyte,0,10,0,height); //range values to display
   }
}

```

---

## ACKNOWLEDGEMENTS

---

I sincerely thank my supervisors, especially Prof. L. Gastaldi for her support in carrying out my research study. Special thanks to Prof. F. Billi for always being available and easygoing with me. Thanks to my parents, my sister, and my grandma M., who always relies on my choices. Although the spent time has proved a tricky step of the way, I am pretty sure I will try to take the positive side.



## BIBLIOGRAPHY

---

- [1] Sehee Ahn, Ayoung Choe, Jonghwa Park, Heesuk Kim, Jeong Gon Son, Sang-Soo Lee, Min Park, and Hyunhyub Ko. "Directed self-assembly of rhombic carbon nanotube nanomesh films for transparent and stretchable electrodes." In: *Journal of Materials Chemistry C* 3.10 (2015), pp. 2319–2325. DOI: [10.1039/C4TC02733G](https://doi.org/10.1039/C4TC02733G).
- [2] Guangming Cai, Mengyun Yang, Zhenglin Xu, Jiangan Liu, Bin Tang, and Xungai Wang. "Flexible and wearable strain sensing fabrics." In: *Chemical Engineering Journal* 325 (2017), pp. 396–403. DOI: <https://doi.org/10.1016/j.cej.2017.05.091>.
- [3] Mengting Chen, Ling Zhang, Shasha Duan, Shilong Jing, Hao Jiang, and Chunzhong Li. "Highly Stretchable Conductors Integrated with a Conductive Carbon Nanotube/Graphene Network and 3D Porous Poly(dimethylsiloxane)." In: *Advanced Functional Materials* 24.47 (2014), pp. 7548–7556. DOI: [10.1002/adfm.201401886](https://doi.org/10.1002/adfm.201401886).
- [4] Xinning Ho, Ju Nie Tey, Wenjun Liu, Chek Kweng Cheng, and Jun Wei. "Biaxially stretchable silver nanowire transparent conductors." In: *Journal of Applied Physics* 113.4 (2013), p. 044311. DOI: [10.1063/1.4789795](https://doi.org/10.1063/1.4789795).
- [5] Daeshik Kang, Peter V. Pikhitsa, Yong Whan Choi, Chanseok Lee, Sung Soo Shin, Linfeng Piao, Byeonghak Park, Kahp-Yang Suh, Tae-il Kim, and Mansoo Choi. "Ultrasensitive mechanical crack-based sensor inspired by the spider sensory system." In: *Nature* 516.7530 (2014), pp. 222–226. DOI: [10.1038/nature14002](https://doi.org/10.1038/nature14002).
- [6] Yong Lin, Xuchu Dong, Shuqi Liu, Song Chen, Yong Wei, and Lan Liu. "Graphene–Elastomer Composites with Segregated Nanostructured Network for Liquid and Strain Sensing Application." In: *ACS Applied Materials & Interfaces* 8.36 (Sept. 2016), pp. 24143–24151. DOI: [10.1021/acsami.6b08587](https://doi.org/10.1021/acsami.6b08587).
- [7] Yong Lin, Shuqi Liu, Song Chen, Yong Wei, Xuchu Dong, and Lan Liu. "A highly stretchable and sensitive strain sensor based on graphene–elastomer composites with a novel double-interconnected network." In: *Journal of Materials Chemistry C* 4.26 (2016), pp. 6345–6352. DOI: [10.1039/C6TC01925K](https://doi.org/10.1039/C6TC01925K).
- [8] Yu Long, Xuanliang Zhao, Xin Jiang, Li Zhang, Han Zhang, Yuan Liu, and Hongwei Zhu. "A porous graphene/polydimethylsiloxane composite by chemical foaming for simultaneous tensile and compressive strain sensing." In: *FlatChem* 10

- (2018), pp. 1–7. DOI: <https://doi.org/10.1016/j.flatc.2018.07.001>.
- [9] Jianhua Ma, Peng Wang, Hongyu Chen, Shenjie Bao, Wei Chen, and Hongbin Lu. “Highly Sensitive and Large-Range Strain Sensor with a Self-Compensated Two-Order Structure for Human Motion Detection.” In: *ACS Applied Materials & Interfaces* 11.8 (Feb. 2019), pp. 8527–8536. DOI: [10.1021/acsami.8b20902](https://doi.org/10.1021/acsami.8b20902).
- [10] Jiuke Mu, Chengyi Hou, Gang Wang, Xuemin Wang, Qinghong Zhang, Yaogang Li, Hongzhi Wang, and Meifang Zhu. “An Elastic Transparent Conductor Based on Hierarchically Wrinkled Reduced Graphene Oxide for Artificial Muscles and Sensors.” In: *Advanced Materials* 28.43 (2016), pp. 9491–9497. DOI: [10.1002/adma.201603395](https://doi.org/10.1002/adma.201603395).
- [11] Zhen Sang, Kai Ke, and Ica Manas-Zloczower. “Interface Design Strategy for the Fabrication of Highly Stretchable Strain Sensors.” In: *ACS Applied Materials & Interfaces* 10.42 (Oct. 2018), pp. 36483–36492. DOI: [10.1021/acsami.8b14573](https://doi.org/10.1021/acsami.8b14573).
- [12] Zhen Sang, Kai Ke, and Ica Manas-Zloczower. “Elastomer Composites with a Tailored Interface Network toward Tunable Piezoresistivity: Effect of Elastomer Particle Size.” In: *ACS Applied Polymer Materials* 1.4 (Apr. 2019), pp. 714–721. DOI: [10.1021/acsapm.8b00241](https://doi.org/10.1021/acsapm.8b00241).
- [13] Ming Wang, Kai Zhang, Xin-Xin Dai, Yin Li, Jiang Guo, Hu Liu, Gen-Hui Li, Yan-Jun Tan, Jian-Bing Zeng, and Zhanhu Guo. “Enhanced electrical conductivity and piezoresistive sensing in multi-wall carbon nanotubes/polydimethylsiloxane nanocomposites via the construction of a self-segregated structure.” In: *Nanoscale* 9.31 (2017), pp. 11017–11026. DOI: [10.1039/C7NR02322G](https://doi.org/10.1039/C7NR02322G).
- [14] Yue Wang et al. “A highly stretchable, transparent, and conductive polymer.” In: *Science Advances* 3.3 (Mar. 2017), e1602076. DOI: [10.1126/sciadv.1602076](https://doi.org/10.1126/sciadv.1602076).
- [15] Shuying Wu, Raj B. Ladani, Jin Zhang, Kamran Ghorbani, Xuehua Zhang, Adrian P. Mouritz, Anthony J. Kinloch, and Chun H. Wang. “Strain Sensors with Adjustable Sensitivity by Tailoring the Microstructure of Graphene Aerogel/PDMS Nanocomposites.” In: *ACS Applied Materials & Interfaces* 8.37 (Sept. 2016), pp. 24853–24861. DOI: [10.1021/acsami.6b06012](https://doi.org/10.1021/acsami.6b06012).
- [16] Shuying Wu, Shuhua Peng, Zhao Jun Han, Hongwei Zhu, and Chun H. Wang. “Ultrasensitive and Stretchable Strain Sensors Based on Mazelike Vertical Graphene Network.” In: *ACS Applied Materials & Interfaces* 10.42 (Oct. 2018), pp. 36312–36322. DOI: [10.1021/acsami.8b15848](https://doi.org/10.1021/acsami.8b15848).

- [17] Feng Xu, Xin Wang, Yuntian Zhu, and Yong Zhu. “Wavy Ribbons of Carbon Nanotubes for Stretchable Conductors.” In: *Advanced Functional Materials* 22.6 (2012), pp. 1279–1283. DOI: [10.1002/adfm.201102032](https://doi.org/10.1002/adfm.201102032).
- [18] Yang Yu, Yufeng Luo, Alexander Guo, Lingjia Yan, Yang Wu, Kaili Jiang, Qunqing Li, Shoushan Fan, and Jiaping Wang. “Flexible and transparent strain sensors based on super-aligned carbon nanotube films.” In: *Nanoscale* 9.20 (2017), pp. 6716–6723. DOI: [10.1039/C6NR09961K](https://doi.org/10.1039/C6NR09961K).